NAVAL POSTGRADUATE SCHOOL

MONTEREY, CALIFORNIA

THESIS

SURFACE LAYER PROCESSES AND NOCTURNAL LOW-LEVEL JET DEVELOPMENT—AN OBSERVATIONAL STUDY DURING PECAN

by

Michael K. Beall

December 2016

Thesis Advisor: Qing Wang
Second Reader: Wendell Nuss

THIS PAGE INTENTIONALLY LEFT BLANK

REPORT DOCUMENTATION PAGE			*Form Approved OMB No. 0704–0188*

1. AGENCY USE ONLY *(Leave blank)*	**2. REPORT DATE** December 2016	**3. REPORT TYPE AND DATES COVERED** Master's thesis

4. TITLE AND SUBTITLE
SURFACE LAYER PROCESSES AND NOCTURNAL LOW-LEVEL JET DEVELOPMENT—AN OBSERVATIONAL STUDY DURING PECAN

5. FUNDING NUMBERS

6. AUTHOR(S) Michael K. Beall

7. PERFORMING ORGANIZATION NAME(S) AND ADDRESS(ES)
Naval Postgraduate School
Monterey, CA 93943-5000

8. PERFORMING ORGANIZATION REPORT NUMBER

9. SPONSORING /MONITORING AGENCY NAME(S) AND ADDRESS(ES)
N/A

10. SPONSORING / MONITORING AGENCY REPORT NUMBER

11. SUPPLEMENTARY NOTES The views expressed in this thesis are those of the author and do not reflect the official policy or position of the Department of Defense or the U.S. Government. IRB number ____N/A____.

12a. DISTRIBUTION / AVAILABILITY STATEMENT
Approved for public release. Distribution is unlimited.

12b. DISTRIBUTION CODE

13. ABSTRACT (maximum 200 words)

Low-level jets (LLJ) occur in many regions around the world and exhibit a diverse range of impacts across a variety of climate and weather-related applications, including U.S. Department of Defense assets and operations. A team from the Naval Postgraduate School participated in the 2015 Plains Elevated Convection at Night (PECAN) research project and collected high-resolution stable boundary layer data as it evolved through the night. The objective of this study was to use this dataset to identify the impact of LLJ presence on surface layer properties, such as thermal stability, dynamic stability, surface fluxes, and turbulence. Additionally, this study investigated pre-LLJ daytime surface layer conditions that might promote LLJ development and intensification. The subsequent analysis found that both nocturnal thermal stability and dynamic stability, while in the presence of a LLJ, were only marginally stable, a result consistent with previous literature that related LLJ development primarily to boundary layer properties above the surface layer. This study also found that nocturnal surface fluxes of momentum, sensible heat, and latent heat were significantly enhanced during LLJ events, owing mostly to larger-than-normal generation of shear-driven turbulence. Interestingly, this research also found that the presence of the nocturnal LLJ was highly correlated with values of thermal and dynamic stability that were close to neutral. This result appears to be inconsistent with previous literature in that LLJ presence is suggested to occur under clear, cloud-free conditions; this finding warrants further analysis. Finally, after examining the relationship between daytime turbulence and subsequent LLJ presence, jet development appeared to be well-correlated to higher levels of turbulence during the preceding daytime.

14. SUBJECT TERMS Low-level jet, nocturnal boundary layer, stable boundary layer, convective boundary layer, surface layer, ageostrophic wind, thermal stability, dynamic stability, surface flux, turbulence, turbulence kinetic energy, Richardson number, wind shear, buoyancy	**15. NUMBER OF PAGES** 121
	16. PRICE CODE

17. SECURITY CLASSIFICATION OF REPORT	**18. SECURITY CLASSIFICATION OF THIS PAGE**	**19. SECURITY CLASSIFICATION OF ABSTRACT**	**20. LIMITATION OF ABSTRACT**
Unclassified	Unclassified	Unclassified	UU

NSN 7540–01-280-5500 Standard Form 298 (Rev. 2–89)
Prescribed by ANSI Std. 239–18

THIS PAGE INTENTIONALLY LEFT BLANK

Approved for public release. Distribution is unlimited.

SURFACE LAYER PROCESSES AND NOCTURNAL LOW-LEVEL JET DEVELOPMENT—AN OBSERVATIONAL STUDY DURING PECAN

Michael K. Beall
Lieutenant, United States Navy
B.S., Purdue University, 2008

Submitted in partial fulfillment of the
requirements for the degree of

MASTER OF SCIENCE IN METEOROLOGY AND PHYSICAL OCEANOGRAPHY

from the

NAVAL POSTGRADUATE SCHOOL
December 2016

Approved by: Qing Wang
Thesis Advisor

Wendell Nuss
Second Reader

Wendell Nuss
Chair, Department of Meteorology

THIS PAGE INTENTIONALLY LEFT BLANK

ABSTRACT

Low-level jets (LLJ) occur in many regions around the world and exhibit a diverse range of impacts across a variety of climate and weather-related applications, including U.S. Department of Defense assets and operations. A team from the Naval Postgraduate School participated in the 2015 Plains Elevated Convection at Night (PECAN) research project and collected high-resolution stable boundary layer data as it evolved through the night. The objective of this study was to use this dataset to identify the impact of LLJ presence on surface layer properties, such as thermal stability, dynamic stability, surface fluxes, and turbulence. Additionally, this study investigated pre-LLJ daytime surface layer conditions that might promote LLJ development and intensification. The subsequent analysis found that both nocturnal thermal stability and dynamic stability, while in the presence of a LLJ, were only marginally stable, a result consistent with previous literature that related LLJ development primarily to boundary layer properties above the surface layer. This study also found that nocturnal surface fluxes of momentum, sensible heat, and latent heat were significantly enhanced during LLJ events, owing mostly to larger-than-normal generation of shear-driven turbulence. Interestingly, this research also found that the presence of the nocturnal LLJ was highly correlated with values of thermal and dynamic stability that were close to neutral. This result appears to be inconsistent with previous literature in that LLJ presence is suggested to occur under clear, cloud-free conditions; this finding warrants further analysis. Finally, after examining the relationship between daytime turbulence and subsequent LLJ presence, jet development appeared to be well-correlated to higher levels of turbulence during the preceding daytime.

THIS PAGE INTENTIONALLY LEFT BLANK

TABLE OF CONTENTS

THIS PAGE INTENTIONALLY LEFT BLANK

LIST OF FIGURES

THIS PAGE INTENTIONALLY LEFT BLANK.

LIST OF TABLES

THIS PAGE INTENTIONALLY LEFT BLANK

LIST OF ACRONYMS AND ABBREVIATIONS

ABL	atmospheric boundary layer
AGL	above ground level
AOR	area of responsibility
CAPE	convectively available potential energy
CASES-99	Cooperative Atmospheric Surface Exchange Study—1999
CBL	convective boundary layer
CDT	Central Daylight Time
DOD	Department of Defense
DOE	Department of Energy
FP	Fixed PISA
HRDL	high-resolution Doppler lidar
LLJ	low-level jet
NASA	National Aeronautics and Space Administration
NBL	nocturnal boundary layer
NOAA	National Oceanic and Atmospheric Administration
NPS	Naval Postgraduate School
NSF	National Science Foundation
NWP	numerical weather prediction
PECAN	Plains Elevated Convection at Night
PISA	PECAN Integrated Sounding Array
TKE	turbulence kinetic energy
TRL	tilted residual layer
UMBC	University of Maryland-Baltimore County
UTC	Coordinated Universal Time

THIS PAGE INTENTIONALLY LEFT BLANK

ACKNOWLEDGMENTS

Special acknowledgement for this project goes to the National Science Foundation for their support and contribution to this field experiment through the funding provided by grant number AGS-1359723.

I would also like to acknowledge the collective NPS team at FP-2 in Greensburg, KS. My professor, Dr. Qing Wang, has provided immeasurable guidance both in the field and during the research and analysis phase of my project. Your tireless efforts and ingenuity have greatly expanded the scope and originality of my work. The MATLAB coding expertise of Ryan Yamaguchi and comprehensive instrumentation knowledge of Dick Lind rendered data collection and processing an accomplishable task. Monotonous data collection during late nights in the field was made more manageable with the help and comic relief of LT Geoff Eberle.

Additional acknowledgement goes to John Kalogiros of the National Observatory of Athens in Athens, Greece, for the numerous times he generated or modified MATLAB coding to assist our team in data processing. Finally, I would like to acknowledge Belay Demoz and Ruben Delgado, who served as principal investigators for the University of Maryland–Baltimore County and generously provided us with high-resolution lidar data collected at their site and guidance with which to process it.

THIS PAGE INTENTIONALLY LEFT BLANK

I. INTRODUCTION

Low-level jet (LLJ) streams are nocturnal boundary-layer phenomena that generally occur in regions downslope of mountain ranges or in areas dominated by strong spatial temperature contrasts, such as the land-sea interface. The LLJ has been observed in numerous geographic locations around the world, including the west coast of South America (Garreaud 2005), Europe (Baas et al. 2009), and the east coast of China and Taiwan (Chen 1987). They have been most extensively documented, however, across the U.S. Great Plains where numerous research projects have been undertaken to better understand their evolution and implications.

The Great Plains LLJ commonly "develops around sunset, under dry cloud-free conditions conducive to strong radiational cooling, reaches peak intensity during the early morning hours, and decays shortly after dawn following the onset of daytime convective mixing," as described in Shapiro (2009). Common characteristics of the nocturnal LLJ include wind-maxima that can exceed geostrophic values by 100% or more, positioning at levels below 1000m within the atmospheric boundary layer (ABL), and an anticyclonic rotation (veering) of the wind direction with both time and height. LLJs can exert wide-ranging influences on a variety of regional weather and climate applications. They serve as dynamical and thermodynamic support mechanisms for the development of deep, elevated convective thunderstorms and long-duration, heavy rain events. LLJs function as efficient conveyors of fungi, pollen, mold spores, insects, and lower-tropospheric pollutants, often transporting particulates several hundred miles in a single night. They are also important providers of clean, sustainable wind energy for wind farms. Downward transport of LLJ-enhanced momentum coupled with the post-sunrise onset of turbulent mixing during the day generates strong surface winds that have been known to rapidly intensify wildfires. Finally, strong wind shear generated by LLJ events may present significant aviation hazards, especially during take-off and landing (Shapiro 2009).

U.S. Department of Defense (DOD) assets operate all over the world, spanning areas of responsibility (AORs) in both the terrestrial and maritime domain. Considering the high LLJ frequency in many places around the world and their wide-ranging impacts

and implications, especially aviation hazards, it is beneficial to attempt to gain better understanding of these phenomena to mitigate weather-related casualties to both manpower assets and equipment.

The Plains Elevated Convection at Night (PECAN) project was a multi-agency, multi-institution project sponsored by the National Science Foundation (NSF), National Oceanic and Atmospheric Administration (NOAA), National Aeronautics and Space Administration (NASA), and U.S. Department of Energy (DOE). PECAN was comprised of eight research laboratories and fourteen universities, and was designed to advance the understanding of continental, nocturnal, warm-season precipitation. PECAN was primarily focused on nocturnal convection over the southern Great Plains when it occurred under the influence of a stable boundary layer, a nocturnal LLJ and higher values of convectively available potential energy (CAPE) above the ABL. Despite numerous qualitative studies, forecast accuracy and a thorough understanding of elevated convection remains a high priority. Within the scope of the PECAN mission, this thesis work intends to characterize the near-surface environment, how it contributes to the formation of the nocturnal LLJ, and how it is modified by the LLJ presence over the Great Plains. In particular, this study seeks to analyze boundary layer parameters and surface layer turbulence data collected during the six-week PECAN field campaign and compare the findings with quantitative studies in recent literature. The ultimate goal is to obtain improved boundary layer parameterizations within numerical weather prediction (NWP) models such that physical processes under the influence of the nocturnal LLJ are better resolved. This will result in increased lead-time in forecast products and improved forecast accuracy in LLJ-associated impacts.

In this thesis, Chapter II will give a comprehensive review of the current literature on different LLJ formation mechanisms and the relationship between boundary layer processes and LLJ evolution. Chapter III will give a brief site description and a comprehensive description of instrumentation used and their respective specifications. In Chapter IV, case selection criteria, experiment results, and accompanying discussion will be presented. Finally, my findings from the PECAN project will be summarized in Chapter V, with accompanying remarks on future work and collaborations.

II. BACKGROUND

This literature review will give a comprehensive examination of previous research on LLJ formation mechanisms, including inertial oscillation, baroclinicity over a sloping terrain, and a unified combination of these two theories. Additional topics of discussion will focus on qualitative studies correlating various boundary layer processes to relative LLJ strength, as well as turbulence kinetic energy and atmospheric stability response under the influence of the LLJ.

A. LLJ FORMATION

Several theories pertaining to the formation of the Great Plains nocturnal LLJ have been proposed over the years. The inertial oscillation concept proposed by Blackadar (1957) has served as the foundation for LLJ formation theory for almost 60 years. Holton (1967) applied baroclinicity over a gentle slope coupled with the equations of motion to further simulate LLJ formation. More recent numerical simulations of LLJ formation have focused on variable combinations of both the Blackadar and Holton mechanisms as the driving force behind LLJ development (Shapiro and Federovich 2009; Shapiro and Federovich 2010; Shapiro et al. 2016). Other LLJ formation theories incorporate applications of potential vorticity conservation associated with the foothills of the Rocky Mountains (Zhong et al. 1996; Wexler 1961) and larger scale synoptic meteorological forcing (Song et al. 2005; Wei et al. 2013; Hu et al. 2013b). These latter two theories cannot explain the diurnal nature or vertically jet-like shape of the Great Plains LLJ, and as such, will not be discussed further.

B. INERTIAL OSCILLATION

The 1957 Blackadar theory postulates that an inertial oscillation resulting from the rapid stabilization of the boundary layer near sunset is responsible for the formation of a low-level ageostrophic wind maxima over the Great Plains. This rapid stabilization and subsequent shutdown of turbulent (frictional) stresses typically occurs under dry, cloud-free conditions. The existence of a generally east-west oriented synoptic-scale pressure gradient is vital for the validity of inertial oscillation theory. Around the time of

sunset, air parcels are freed from any turbulent frictional constraint and accelerate in the direction of the ambient pressure gradient force, with a coincident rightward deflection by Coriolis force. Blackadar's simulation found that the height of the wind speed maximum usually coincided with the top of the nocturnal inversion and he attributed the upward-growing inversion height to turbulent transfer generated at or near the Earth's surface resulting from large wind shear within the inversion. Blackadar suggests that, because vertical mixing within the boundary layer acts to dampen wind maxima and minima, vertical turbulent mass exchange is not favorable for jet maintenance. Within a deepening nocturnal inversion, a small amount of turbulence is maintained within the inversion layer due to wind shear. This turbulence acts to transfer heat from the top of the boundary layer down to the surface where it is lost to radiational cooling, resulting in a net loss of heat, and thereby further deepening the inversion (Blackadar 1957).

Blackadar assumes, for simplicity, that the horizontal pressure gradient is constant in time and space, and that the motion is completely horizontal. The equations of motion just above the inversion may be written as:

$$\frac{\partial}{\partial t}\left(u - u_g\right) = f\left(v - v_g\right) \tag{1}$$

$$\frac{\partial}{\partial t}\left(v - v_g\right) = -f\left(u - u_g\right) \tag{2}$$

where u, v, u_g, and v_g are components of the wind and geostrophic wind and f the Coriolis parameter. The solution of these equations is facilitated by introducing a complex number

$$W = (u - u_g) + i(v - v_g) \tag{3}$$

which, when plotted in the complex plane, yields a vector representing a deviation from the geostrophic wind, or the ageostrophic wind. Therefore, Equations 1 and 2 become

$$\frac{\partial W}{\partial t} = -ifW \tag{4}$$

and after integrating, yields

$$W = W_o e^{-ift} \tag{5}$$

where W_o is the ageostrophic deviation at the initial time, which may be assumed to occur around sunset. The motion resulting from this solution can be seen in Figure 1. It can be seen that the ageostrophic wind remains constant in magnitude but rotates to the right, with a period of one-half pendulum day per complete revolution, owing to the veering nature of the LLJ. From Figure 1, it can be seen that, if W_o is a typical geostrophic deviation at time=0, or sunset, a supergeostrophic wind maximum is reached approximately six hours later (Blackadar 1957).

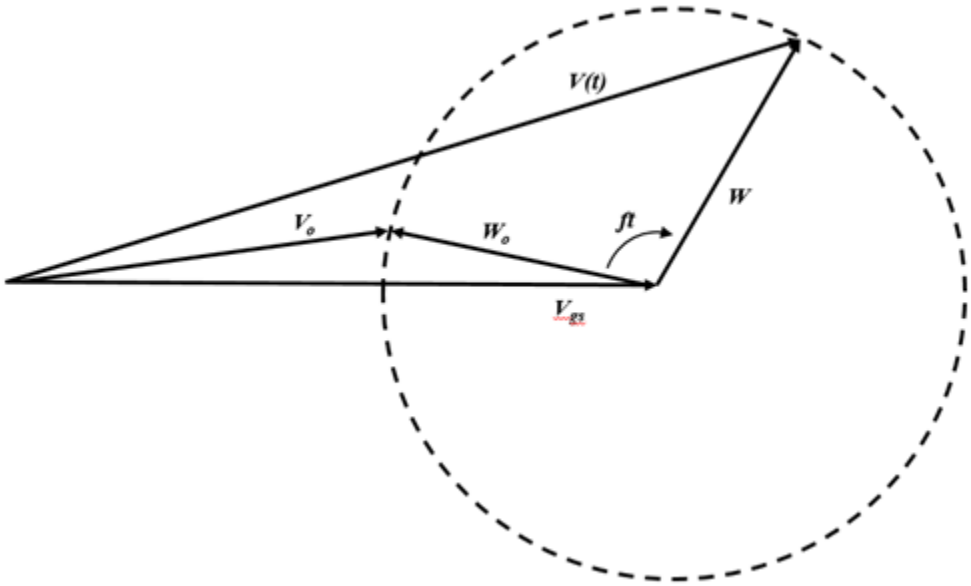

Relation of the ageostrophic wind W and the wind vector V(t) to the initial values W_o, V_o and the geostrophic wind vector V_g during a frictionally initiated inertial oscillation

Figure 1. Variation of Ageostrophic Wind with Time at Single Level above Inversion. Adapted from Blackadar (1957).

Blackadar proposed that, above the inversion where this solution is valid, the solution at each subsequently higher level may be considered independently of levels above or below, except that, at the initial time, W_o is determined as a function of height. The wind profile above the inversion, as indicated in Figure 2, represents the combination of solutions at every pertinent level. In cases where the initial geostrophic deviation is not approximately opposite that of the geostrophic wind, the supergeostrophic wind

maximum would be reached at a different time interval than the arbitrary case depicted in Figure 2, and furthermore, may not necessarily occur simultaneously at all levels. It is important to note that the geostrophic wind has not necessarily been deemed to be independent of height, and as such, the above Blackadar model could be modified to apply to cases where the geostrophic wind changes with height (Blackadar 1957).

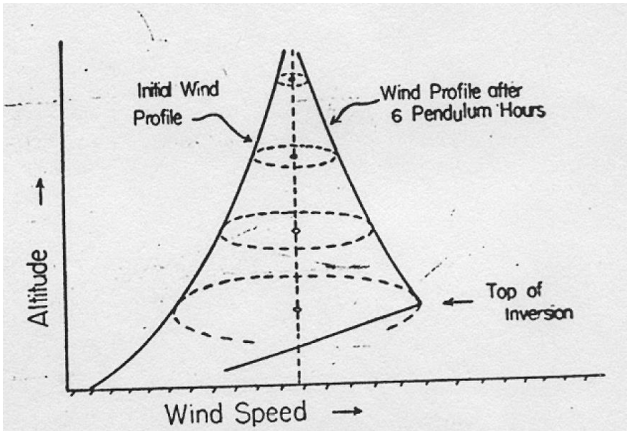

Figure 2. Schematic Illustration Explaining Boundary Layer Jet Evolution. Source: Blackadar (1957).

Blackadar observed that the sharpness of LLJ maximum is generally enhanced when the geostrophic wind decreases with height, and that if the decrease is sufficiently rapid, that a jet-like profile may even develop during the day. However, a LLJ may not develop at all if the geostrophic wind increases too rapidly with height. Below the jet, the wind speed distribution may be explained by supposing that varying amounts of momentum have been extracted by a downward turbulent flow and subsequently dissipated at the surface (Blackadar 1957).

C. BAROCLINICITY OVER SLOPING TERRAIN

Although Blackadar's generation of a LLJ hodograph that depicts veering winds with height and a jet maxima attained during the nocturnal period have been verified in various qualitative studies, subsequent observational field projects have suggested that inertial oscillation theory may be incomplete. As an example, Blackadar's inertial oscillation theory cannot, by itself, explain how peak LLJ speeds can exceed

supergeostrophic values by more than 100%. It also does not account for the geographic preference of the LLJ for the U.S. Great Plains and their gently sloping terrain, whereby maximum frequency of LLJ occurrence is around 100°W. Additionally, Blackadar suspected a close association between the height of LLJ maximum and the vertical extent of nocturnal temperature inversion. Several qualitative cases have revealed such a relation, but a rather larger number of studies have demonstrated that this association may not be valid. It has been found in numerous case studies that, while nocturnal inversions generally grow in height over the course of a night, the height of LLJ wind maximum may decrease, increase or remain constant (Shapiro 2009).

Alternative theories have been advanced to attempt to explain the geographical inclination of the summertime nocturnal LLJ to a narrow longitudinal swath over the Great Plains. In 1967, Holton set to expand upon an idea proposed by Bleeker and Andre (1951), proposing that "low-level nocturnal convergence of the wind over the Mississippi basin is the result of a large scale drainage wind caused by downslope flow of radiationally cooled air along the slopes of both the Rocky mountains to the west and Appalachian mountains to the east." Holton further suggests that "the resultant drainage implies that the thermal and viscous boundary layers are coupled through a diurnally oscillating density field" (Holton 1967).

Holton assumes a geostrophic wind parallel to the y-axis (southerly component of the wind) and that the diurnal temperature oscillation is independent of y, making all variables functions of x and z alone. He deems this approach justifiable, as the north-south scale of the LLJ is much larger than the east-west scale. Holton conducted non-dimensional analysis on the equations of motion, continuity equation, and thermodynamic energy equation in the newly established coordinate system. Of these six equations, special attention should be given to the χ-momentum (east-west terrain-tangent direction) equation and equation representing diurnal temperature variation:

$$\frac{\partial u}{\partial t} - v\cos\phi = -\frac{\partial p}{\partial \chi} - \frac{\rho \sin\phi}{\delta} + \frac{\partial^2 u}{\partial \zeta^2} \tag{6}$$

$$\frac{\partial \theta}{\partial t} + u\frac{\sin\phi}{\varepsilon\delta} = \frac{\partial^2 \theta}{\partial \zeta^2} + H(\theta_R - \theta) \tag{7}$$

where H is a variable stability parameter, θ_R is the non-dimensional amplitude of the diurnal temperature variation, ϕ is the terrain slope angle, and ζ is the ground-normal direction. In Equation 7, if the heating cycle is approximated as a harmonic oscillation of temperature as it decreases exponentially with height, Holton defines the non-dimensional diurnal temperature variation as:

$$\theta_R = \theta_R(0)e^{-\zeta}\cos(\Omega t^*) \tag{8}$$

where $\theta_R(0)$ is the amplitude of θ_R at the ground, Ω is the angular velocity of the Earth, and $t^*=t/f$ where $f=2\ \Omega\sin(\text{latitude})$, such that, when f is evaluated at 30°N, $\theta_R = \theta_R(0)e^{-\zeta}\cos t$. It follows that $t=0$ corresponds to the time of maximum temperature at the ground. The χ-momentum equation retains the normal terms for the time-dependent Ekman layer with the addition of the term $-\rho\sin\phi/\delta$. In the Great Plains, $\sin\phi \sim 0(\delta)$ and must be included in the equations. It represents gravity in the χ direction which exists when the terrain slope angle $\phi\neq 0$, and subsequently produces both downslope and upslope accelerations when $\rho>0$ and $\rho<0$, respectively. It follows that, over a gentle slope, the diurnally varying temperature provides a source of gravitational potential energy which consequently forces a diurnal oscillation in the boundary layer current. In Equation 7, which is obtained from Holton:

> The term $u\dfrac{\sin\phi}{\varepsilon\delta}$ represents the rate of potential temperature change due to advection of the mean potential temperature field along χ. The atmosphere is stably stratified when $\varepsilon>0$ and downslope (upslope) motion creates a positive (negative) potential temperature anomaly, which results in a buoyancy force in opposition to the motion. (1967)

The outcome is a suppressed east-west boundary layer wind component when there is stable stratification over a sloping terrain (Holton 1967).

Holton varied a terrain-slope stability parameter $\propto$ for two separate cases: neutral stability and an isothermal atmosphere. Terrain slope over the Great Plains is approximately 1/400 such that $\phi\approx 0.0025$. This yields $\propto=0$ for the neutral stability case and $\propto\approx 0.5$ for the isothermal case. Figure 3 portrays wind hodographs for both the neutral case where $\propto=0$ (solid line) and the isothermal case where $\propto\approx 0.5$ (dashed line).

The neutral case corresponds to level ground and/or neutral stability while the isothermal case represents a stable atmosphere over a sloping terrain where motion across the contour is suppressed by the buoyancy force. The resultant plot is a flatter Ekman spiral with a smaller mass transport across isobars than the neutral case (Holton 1967).

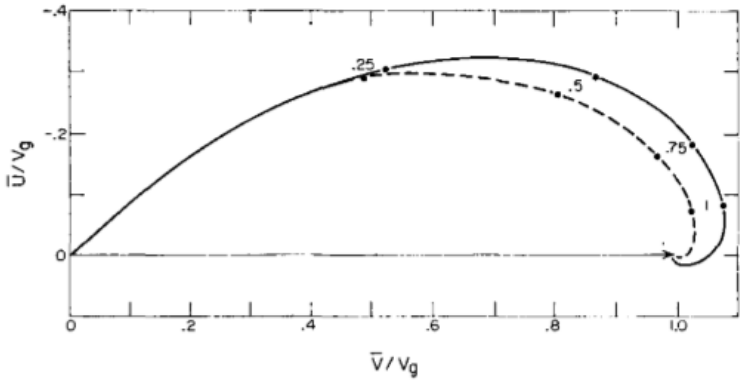

Labeled points refer to height in kilometers

Figure 3. Hodograph Reflecting Flat Terrain/Neutral Case (solid) vs. Sloping Terrain/Isothermal Case (dashed). Source: Holton (1967).

Figures 4 and 5 depict hodographs at 250m, 500m, and 1000m for the neutral case and isothermal case, respectively. Holton observed that positive stability (isothermal case) "reduces the amplitude of the oscillation, decreases the height of maximum amplitude, and increases the ellipticity of the hodographs." Holton concludes from the resulting solutions that, without considering any frictional release as proposed by Blackadar (1957), thermal effects also contribute substantially to the amplitude of the diurnal wind oscillation over sloping terrain such as the Great Plains (Holton 1967). Unfortunately, the Shapiro (2009) numerical simulation suggests that Holton's findings failed to accurately reproduce the phase of diurnal oscillations observed in qualitative studies. Additionally, diurnal boundary layer flow over sloping terrain was not nearly as "jet-like" as qualitative observations depict (Shapiro 2009).

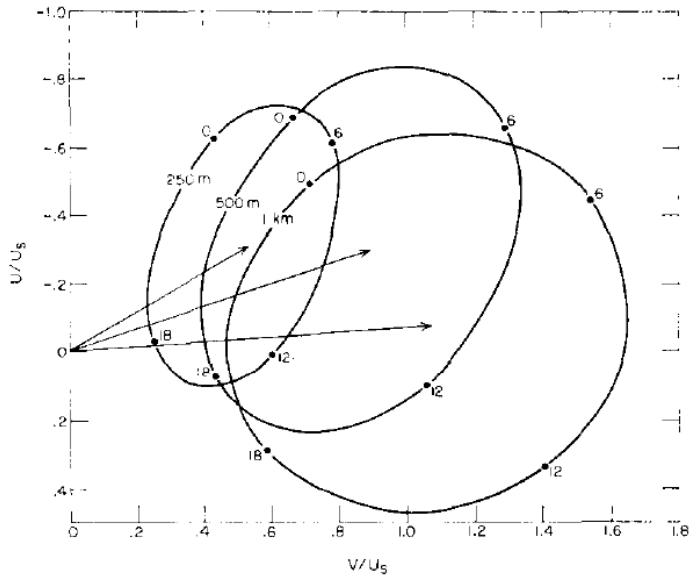

The arrows indicate mean velocity at each level and times indicate hours after time of maximum surface temperature. Ellipses are for 250m, 500m, and 1000m

Figure 4. Neutral Stability Case for $\propto$=0. Source: Holton (1967).

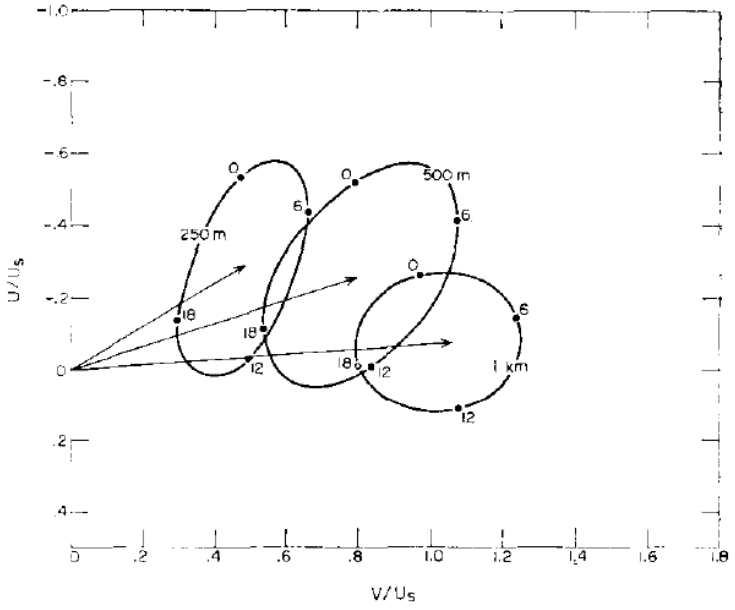

Figure 5. Isothermal Atmosphere/Positive Stability Case for $\propto \approx 0.5$. Source: Holton (1967).

D. BLACKADAR AND HOLTON METHODS COMBINED

In more recent studies, an overwhelming number of published LLJ analyses support Blackadar's inertial oscillation theory, where the Great Plains LLJ arises from a force imbalance that is prompted by the release of friction in the boundary layer around sunset. These findings are accompanied, however, by additional findings that both topographical and meteorological factors do contribute to the nature of the force imbalance. Blackadar's inertial oscillation dominates when a synoptic-scale pressure gradient force is present. The addition of the characteristic sloping terrain of the Great Plains introduces a downslope buoyancy force component resulting from daytime heating, from which the LLJ is thought to behave like an inertial-gravity oscillation. Shapiro and Federovich (2009) extended Blackadar's theory with the inclusion of slope angle and pairing the equations of motion and thermodynamic energy.

Similar to Holton's model construction, Shapiro considers nocturnal LLJ development within the boundary layer over an infinite slope of angle α and no boundary effects. In a Cartesian coordinate system, the *x*-coordinate points east down the slope while the *y*-coordinate points across the slope to the north, as depicted in Figure 6. The premise for the Shapiro model is a wind-oscillation induced within the ABL triggered by the sudden cessation of friction near the time of sunset (t=0), as is presented in Blackadar's theory (Shapiro 2009).

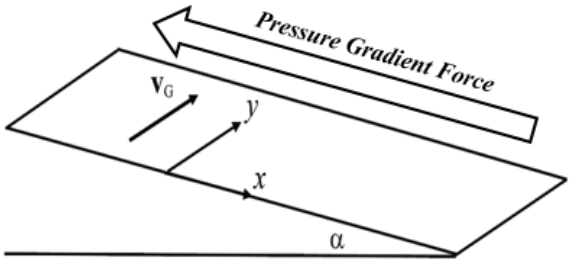

X is the downslope coordinate pointing east, y is the cross-slope coordinate pointing due north, the geostrophic wind vector V_G is southerly and points to the north and the pressure gradient force points west and up the slope.

Figure 6. Slope Following Coordinate System. Adapted from Shapiro (2009).

Shapiro's model differs from Blackadar in that, instead of a purely inertial oscillation, he introduces the concept of an inertial-gravity oscillatory mode. In keeping consistent with Holton 1967, Shapiro (2009) incorporates the existence of a synoptic pressure gradient force which points toward the west (negative *x* direction), with a resultant geostrophic wind from the south ($V_G>0$). Shapiro also remarks on the dependence of LLJ strength and vertical location to the boundary layer's thermal structure. Around sunset, the layer that has been convectively mixed becomes characterized by weak turbulence that is in a state of decay. In the very near-surface layer, a thin stably stratified boundary layer begins to develop. Just above this layer where the thermal structure remains largely unchanged from the well-mixed, late afternoon regime, there exists a residual layer. The residual layer extends vertically to a capping inversion at the free atmosphere, typically between 1 and 2 km above ground level (AGL). Shapiro (2009) suggests that this same residual layer also exists over sloping terrain and recalls "that parcel buoyancy is proportional to the potential temperature difference between the parcel and the environment at the same elevation." He concluded that there exists a local, neutrally stratified tilted residual layer (TRL) that is also characterized by non-zero buoyancy. Shapiro's TRL would have a downward-directed buoyancy gradient, resulting in a positively buoyant layer at the lower levels while maintaining negative buoyancy just below the capping inversion. This concept is depicted in Figure 7.

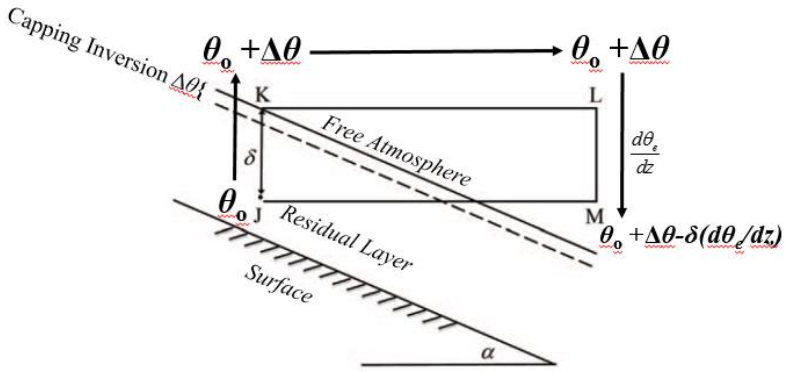

The sloping dashed and solid lines represent the base and top of the capping inversion, respectively. Point J represents the position of an air parcel within the residual layer, while δ is the distance from the parcel to the top of the capping inversion layer. Point L is in the free atmosphere and at the same elevation as point K, and point M is in the free atmosphere directly beneath point L at the same elevation as point J. The horizontal line KL is an environmental isentrope. An air parcel with given initial potential temperature in the residual layer along sloping terrain cycles through a capping inversion and along an environmental isentrope as shown.

Figure 7. Vertical Cross-Section through a Residual Layer over a Shallow-Slope. Adapted from Shapiro et al. (2009).

The parcel depicted in Figure 7 above, after completing the point J to point M cycle, has resulting potential temperature $\theta_o + \Delta\theta - \delta(\frac{d\theta_e}{dz})$ at M. From this, one can interpret the initial buoyancy at J (or any point within the residual layer) as $b_o - g\frac{\Delta\theta}{\theta_r} + N^2\delta$ and multiplying both sides by $\frac{\sin\alpha}{fv_G}$ yields a non-dimensional initial buoyancy parameter:

$$B_o = \frac{N^2 \sin\alpha}{fv_G}\delta - \frac{\sin\alpha g\Delta\theta}{fv_G\theta_r} \tag{9}$$

Shapiro offers that, "since δ decreases with an increasing slope-normal coordinate, the slope-normal derivative of B_o is negative, meaning that buoyancy decreases upward, and has magnitude proportional to N^2, meaning that it is strongly dependent on the static stability in the free atmosphere." For parcels at or just below the base of the capping inversion, δ is small and B_o is dominated by the second term, and initial buoyancy values are negative. For parcels at lower levels, the first term dominates, and initial buoyancy is positive. This is significant, as many observed LLJs occur beneath a height of 500m

AGL, corresponding to a range of heights in the lower portion of the residual layer. Additionally, after introducing sloping terrain to the equations of motion and parcel buoyancy, parcels at progressively lower levels of a TRL would be associated with larger values of initial buoyancy, which, in turn, induce progressively larger oscillation amplitudes (Shapiro 2009).

Shapiro applies this varying, non-dimensional buoyancy to his non-dimensional solution for *V(T)* which is given by:

$$V(T) - V_o = -\frac{U_o}{\Omega}\sin\Omega T + \frac{1}{\Omega^2}(-B_o + V_o - 1)(\cos\Omega T - 1) \tag{10}$$

where $V \equiv v/v_G$, $V_o \equiv v_o/v_G$, $U_o \equiv u_o/u_G$, $T \equiv ft$, and $\Omega \equiv \omega/f$, where $\omega = \sqrt{f^2 + N^2 \sin^2\alpha}$. Applying Equation 9 to Equation 10 at time $T = \pi/\Omega$ when V is at max amplitude and assuming $U_o = 0$ gives a solution for maximum V:

$$V_{\max} = V_o\left(1 - \frac{2f^2}{f^2 + N^2\sin^2\alpha}\right) + \frac{2f^2}{f^2 + N^2\sin^2\alpha}\left(\frac{N^2\sin\alpha}{fv_G}\delta - \frac{\sin\alpha}{fv_G}\frac{g\Delta\theta}{\theta_r} + 1\right) \tag{11}$$

From Equation 11, Shapiro infers that large values of V_{max} are valid for parcels with large initial values of ageostrophic wind speed ($1\text{-}V_o$) when V_o is small and are located at low levels when δ is large. The parcels are also located within a residual layer where there is a relatively small capping inversion $\Delta\theta$. Figures 8 and 9 depict Shapiro's findings well and plot V_{max} as a function of α (slope angle), $\Delta\theta$ (inversion strength), N (stability), and V_o (initial southerly wind component) (Shapiro 2009).

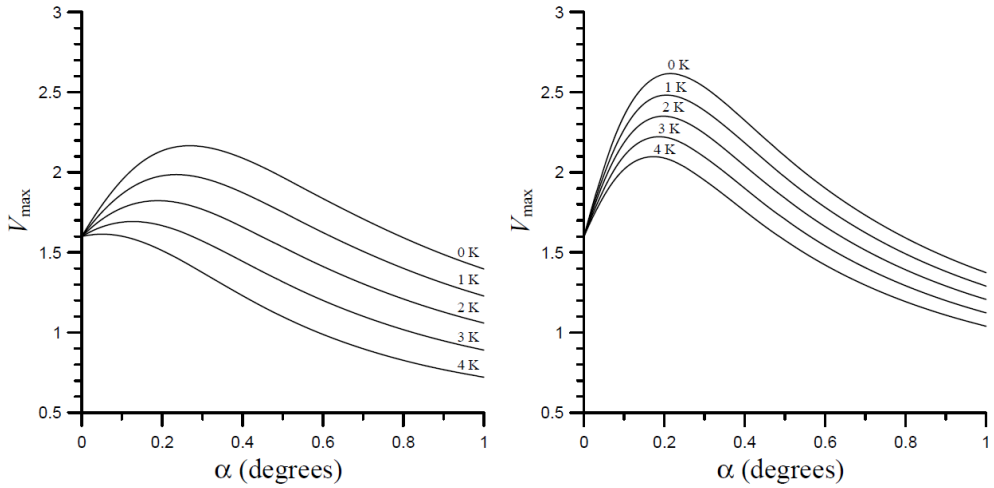

Plots of V_{max} as a function of slope angle α (x-axis), Δθ in degrees K (multiple curves), stability N (left plot N=0.01 s^{-1} and right plot N=0.015 s^{-1}) for initial southerly wind component V_o=0.4.

Figure 8. Maximum Ratio (V_{max}) of Ageostrophic Wind (LLJ) to Geostrophic Wind for V_o=0.4. Source: Shapiro et al. (2009)

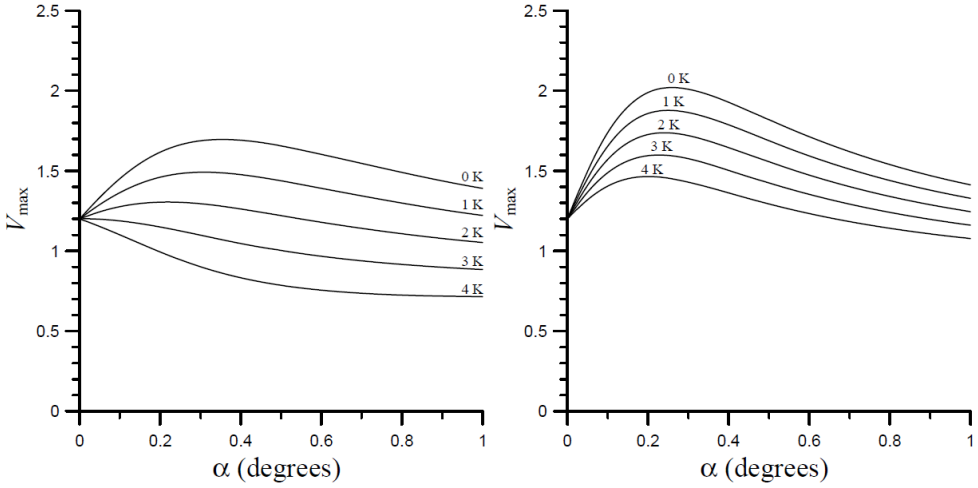

Plots of V_{max} as a function of slope angle α (x-axis), Δθ in degrees K (multiple curves), stability N (left plot N=0.01 s^{-1} and right plot N=0.015 s^{-1}) for initial southerly wind component V_o=0.8.

Figure 9. Maximum Ratio (V_{max}) of Ageostrophic Wind (LLJ) to Geostrophic Wind for V_o=0.8. Source: Shapiro et al. (2009).

These analyses point to the fact that, as slope angle increases, V_{max} increases initially as well, but then decreases after a certain critical value for α. This relationship

holds especially true for the cases of stronger stable stratification (N=0.015 s^{-1}, or the right side of each plot). Shapiro explains this relationship in that, for small slope angle, "the tendency of a positive initial buoyancy to strengthen the amplitude of the oscillation overcomes any inhibiting influence that along-slope advection of environmental potential temperature may have." On the other hand, larger values of α would allow environmental potential temperature advection to dominate. Shapiro predicts that the optimum slope angle for LLJ formation for an initial southerly wind of V_o=0.4 lies between 0.10° and 0.20°, while for an initial southerly wind of V_o=0.8, the optimum slope angle for LLJ formation lies between 0.15° and 0.25°. These findings by Shapiro predict a LLJ-formation corridor somewhere between 100°W and 102°W over the Great Plains (Shapiro 2009).

Additionally, Shapiro plots Vmax as a function of depth below the capping inversion δ, which can be seen in Figure 10. This case is valid for α=0.15° and N=0.01s^{-1}. This plot confirms that stronger jets result from weaker inversions at greater depths under the capping inversion. This is extremely significant in that it contradicts Blackadar's conclusion that stronger LLJs would be found under stronger inversions, and just above the inversion level (Shapiro 2009).

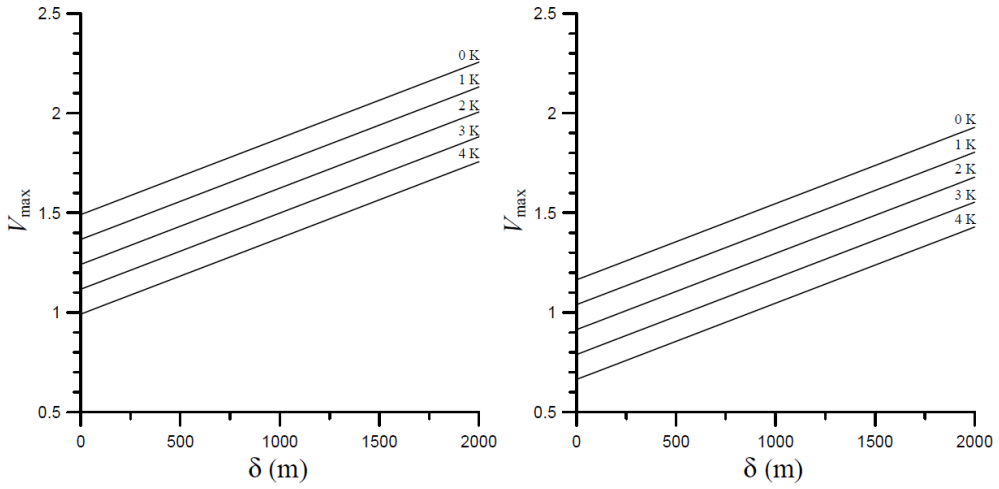

Results shown hold for α=0.15° and N=0.01 s^{-1} and capping inversion strengths of Δθ=0, 1, 2, 3, 4K. Left panel holds for V_o=0.4 and right panel holds for V_o=0.8.

Figure 10. Peak Southerly Jet Speed V_{max} As Function of Distance δ Beneath Capping Inversion (Shapiro 2009)

E. THE ATMOSPHERIC BOUNDARY LAYER AND THE LLJ

Open questions remain yet about LLJ evolution and its interaction with nocturnal boundary layer (NBL) structure. According to Klein et al. (2015), this results primarily from a lack of meaningful, high-resolution observations that account for the layer between the surface and a few hundred meters above the LLJ nose. One of the most comprehensive qualitative studies to investigate connection between characteristics of the nocturnal LLJ and NBL structure was the Joint Urban field experiment in July 2003 in Oklahoma City. Klein's study made use of wind-profile measurements and turbulence quantities measured on an 80m television tower, as well as wind and stability data from the Oklahoma Mesonet network in surrounding rural areas (Klein et al. 2015).

Mean wind speeds at 37m and 80m, denoted as U_{37} and U_{80}, respectively, were used in the Klein et al. (2015) study to evaluate NBL wind shear near the surface. U_{37} was also used as a scaling velocity for turbulent quantities measured at the same height. Frictional velocity, given by

$$u_* = \left[\left(\overline{u'w'} \right)^2 + \left(\overline{v'w'} \right)^2 \right]^{1/4} \tag{12}$$

and turbulent velocity scale U_t, given by

$$U_t = \sqrt{0.5\left(\sigma_u{}^2 + \sigma_v{}^2 + \sigma_w{}^2 \right)} \tag{13}$$

where $\sigma_{u,v,w}{}^2$ is the variance of the *u*, *v*, and *w* velocity components, were used to quantify turbulent mixing within the surface layer, with $U_t{}^2$ serving as a measure of turbulent kinetic energy (TKE). Turbulent kinematic momentum fluxes $\overline{u'w'}$ and $\overline{v'w'}$, and velocity variances were measured from sonic anemometer data at the 37m level and processed using 60-min averaging periods. Wind speeds (u_{10} and u_2) and air temperatures (T_9 and $T_{1.5}$) used to compute the bulk Richardson number, given by

$$Ri = \frac{g\left[\frac{\left(T_9 - T_{1.5} \right)}{\Delta Z_T} + \Gamma_d \right] \Delta Z_u{}^2}{T_{1.5}\left[u_{10} - u_2 \right]^2} \tag{14}$$

were obtained from the Oklahoma Mesonet sites. In the equation for *Ri*, *g* is acceleration due to gravity, ΔZ_T=7.5m is the height difference between temperature levels, ΔZ_u=8.0m is the height difference between wind-speed collection levels, and Γ_d=0.01 K m^{-1} is the dry adiabatic lapse rate (Klein et al. 2015).

Klein et al. (2015) noted an 85% occurrence rate of LLJs in July 2003 over the Oklahoma City experiment site. In most instances, the LLJ nose fell between 400m and 800m AGL. They selected 12 hour time periods for each day and night ranging from 1730–0430 CDT (2230-0930 UTC) and limited LLJ cases to instances where the predominant wind direction measured on the television tower fell within a southerly sector measuring 135°-225°. Daytime values were computed as the average of the 1730–1830 CDT observations, while nighttime values were computed as the average of three-hourly profiles from 0130–0330 CDT. It was found that LLJ properties for each case did not vary much within this nighttime period. Table 2 in Klein (2015) (not shown here) lists important boundary layer parameters and scaling ratios for the 18 cases in which a LLJ was deemed to be present during the Joint Urban experiment (Klein et al. 2015).

Within Klein's analyses, $(U_{LLJ})_{max}$ refers to the maximum value of the LLJ wind speed within a given nighttime period on each respective day. U.S. is the averaged daytime wind maximum above 800m, averaged between 1730 and 1830 CDT. This quantity represents a daytime scaling velocity which serves as a proxy for the pre-sunset geostrophic wind with which to compare nighttime U_{LLJ} values to. The ratio of these two quantities represents the increase of the wind speed at the LLJ nose relative to the initial mixed-layer wind speed. Shown also are proxies for wind shear between the LLJ maxima ($U_{LLJ,max}$) and velocities at 37m on the tower (U_{37}), and between 80m on the tower (U_{80}) and 37m on the tower (U_{37}). Ri_{day} depicts the minimum Richardson number prior to sunset, while Ri_{night} depicts the maximum *Ri* value occurring between 2230 and 0430 CDT. Daytime and nighttime values for U_t, defined above, are listed, along with values for U_t/U_{37}, which have been defined as daytime (mean value between 1730 and 1830 CDT) and nighttime (minimum value between 2230 and 0430 CDT) values of relative turbulence intensities. Figure 11 depicts various wind-speed ratios plotted against various stability and turbulence intensity parameters (Klein 2015).

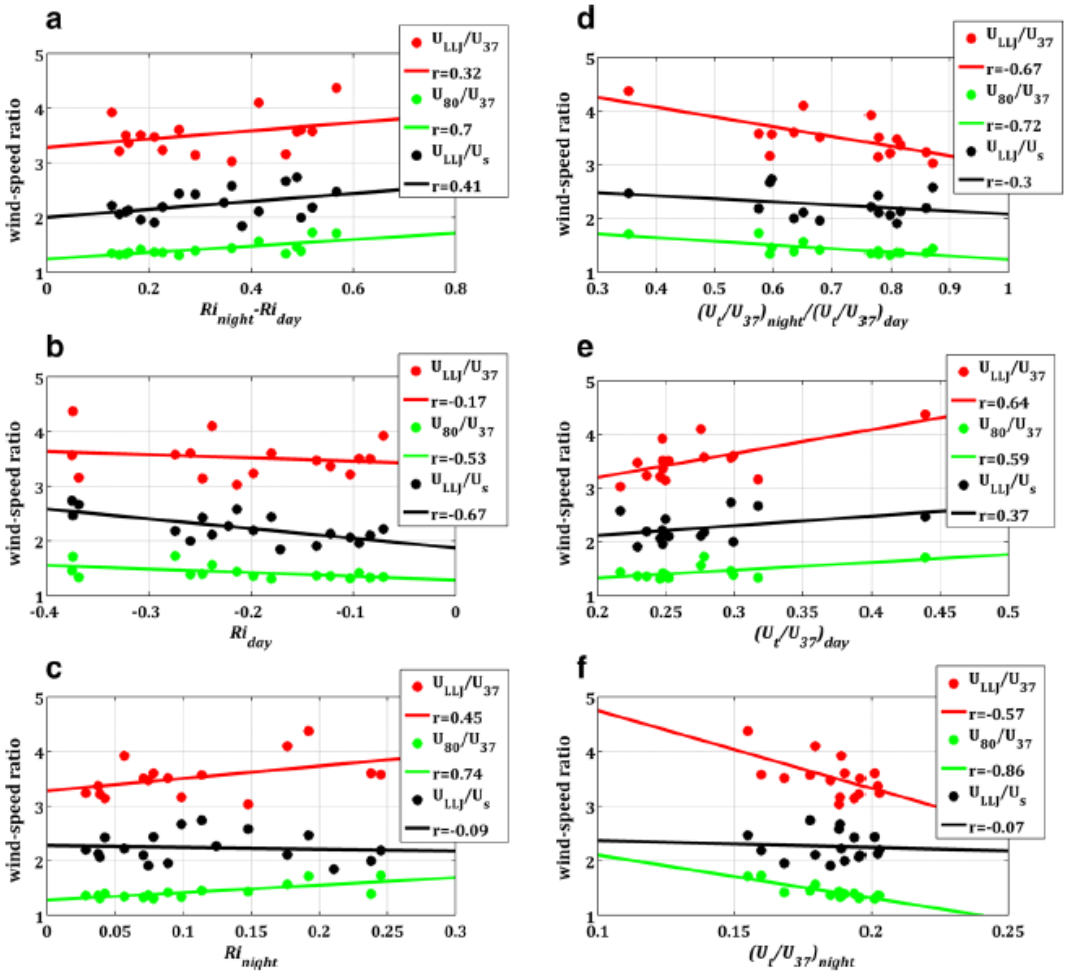

Figure 11. Plots of Relative LLJ Strength and Shear Parameters vs. Various Stability and Shear Parameters. Source: Klein et al. (2015)

For analysis simplicity purposes, ΔRi will be defined as Ri_{night}-Ri_{day}. From Figure 11, it can be seen that relative LLJ strength $(U_{LLJ}/U_S)_{max}$ increases for increasing ΔRi (Figure 11a) and decreasing $\frac{(U_t/U_{37})_{night}}{(U_t/U_{37})_{day}}$ (Figure 11d). Correlation coefficients for these comparisons are low, however, owing to the fairly large scatter in the data. Shear parameters U_{LLJ}/U_{37} and U_{80}/U_{37} are also plotted in Figure 11 and were found to increase with increasing ΔRi and decrease with increasing $\frac{(U_t/U_{37})_{night}}{(U_t/U_{37})_{day}}$, with higher correlation coefficients of 0.7 and 0.72 for U_{80}/U_{37} vs. ΔRi and the turbulence intensity ratio, respectively. Klein also investigated relative LLJ strength $(U_{LLJ}/U_S)_{max}$ plotted against

daytime and nighttime *Ri* by themselves. A strong correlation of 0.67 for $(U_{LLJ}/U_S)_{max}$ vs. Ri_{day} hint at the fact that relative LLJ strength is highly dependent on stronger convective turbulence (lower *Ri*) during the day, while a similarly strong correlation of 0.86 for a decreasing shear parameter U_{80}/U_{37} vs. increasing nighttime turbulence intensity $(U_t/U_{37})_{night}$ suggests that boundary layer wind shear slackens as relative turbulence increases while under the influence of a nocturnal LLJ. Klein's findings indicate that relative LLJ strength is dependent upon the magnitude of change in atmospheric stability, as well as the magnitude of change of turbulence intensity during the early evening transition. Klein underscores the fact that "conditions in the daytime convective boundary layer (CBL) immediately prior to sunset are critical, and as such, Ri_{day} is a good indicator of LLJ strength." (Klein 2015)

Under LLJ influence, turbulence and the resultant fluxes in the stable NBL are generated by vertical shear of the horizontal wind. When the LLJ develops after sunset, a layer of enhanced shear forms between the jet nose and Earth's surface resulting in the generation of turbulence. It follows that LLJ strength can act as a control mechanism on the magnitude of turbulence and associated fluxes within the stable NBL. Banta et al. (2002) performed numerous analyses from the Cooperative Atmospheric-Surface Exchange Study-1999 (CASES-99) field campaign in southeast Colorado in October 1999. They analyzed high resolution Doppler lidar (HRDL) data and turbulence kinetic energy (TKE) data from a sonic anemometer on a 60m tower, combined with stability estimates, to gain a deeper understanding for TKE behavior as a result of LLJ presence. LLJ maximum speed U_X and Z_X, its height, were used to approximate shear below the jet nose as U_X/Z_X (Banta et al. 2002).

Sonic anemometers were positioned at the 45m, 50m, and 55m levels on the tower, and TKE values were calculated over 1, 3, 5, 7, 9, and 11 minute intervals centered on the middle of each 15 minute period for which U_X and Z_X had been calculated. Resultant time series were then divided into 1 minute segments with TKE calculated for each segment, following a procedure delineated in Vickers and Mahrt (2003) to account for turbulence non-stationarity. Banta states that "TKE for these segments was then further averaged for the 3, 5, 7, 9, and 11 temporal segments centered on each 15 minute interval of LLJ data." In these cases, resulting TKE values were

averaged in the vertical for each of the 45m, 50m, and 55m levels of the tower. Banta investigated the results from 1 minute averaged segments, further averaged over five segments, which is to say over a 5 minute period in the middle of each 15 minute block. For this experiment, Z_X was found generally in a layer between 80m and 150m, and estimates of TKE at ~50m were often in the middle of the below-jet shear layer. Banta also introduces the bulk jet Richardson number as a viable stability parameter, and given by

$$Ri_J = \frac{g\left(\Delta\theta / \Delta z\right)}{\theta\left(U_X / Z_X\right)^2} \tag{15}$$

where shear in the denominator is estimated from the speed and height of the jet. Banta presents two cases in which both a strong LLJ and weak LLJ are accounted for. The 25 October strong LLJ case is associated with TKE levels exceeding 0.4 m^2s^{-2} for most of the night, while a weak LLJ occurred on 26 October with relatively small TKE below 0.05 m^2s^{-2} for most of the night (see Figures 3 and 4 in Banta (2002)). Also included in Banta's analyses was a scatter diagram of Ri_J vs. TKE for entire sample period of 10 nights, which can be found in Figure 12 (Banta et al. 2002).

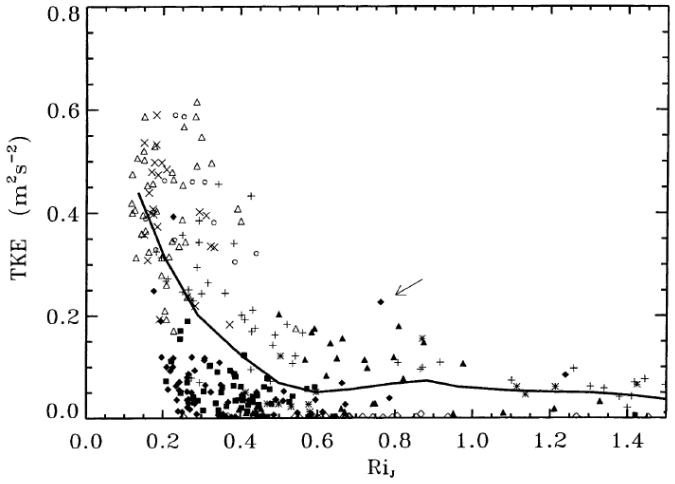

Shear estimates were obtained from HRDL measurements

Figure 12. Scatter Diagram of Ri_J vs. TKE for Entire 10-Night Sample Period. Source: Banta et al. (2002)

For the strong LLJ night on 25 October, high TKE values appeared generally for Ri_J values between 0.1 and 0.3, while for the weak LLK night on 26 October, much lower TKE values were observed for significantly higher jet Richardson numbers generally higher than 3. In observing Figure 13 for the entire sample period, it is significant to note that, for stable Ri_J values greater than 0.4, TKE values were generally low, with values around 0.1 m^2s^{-2} or less. As Ri_J values decreased below 0.4, a marked increase in turbulence values was observed. The solid line in Figure 13 represents mean TKE values for each 0.05 interval of Ri_J and shows the increase of TKE as Ri_J decreases to below 0.4 (Banta et al. 2002).

Banta's analysis has shown that shear generated below the LLJ plays a significant role in turbulence generation and turbulent fluxes within the stable NBL over non-mountainous terrain. Bulk properties of the LLJ, including speed and height, are useful for estimating shear below the jet, which in turn can be used to calculate Ri_J and can then be further used to predict turbulence in the layer below the jet. If these bulk properties of LLJ strength and height can be accurately determined or extracted from NWP models, they could also be used to forecast turbulence quantities within the boundary layer. Banta notes that, for proper representation of Ri_J, it is critical to obtain an accurate measure of stability $\partial\theta/\partial z$ near the surface. In NWP models, this involves accurate incorporation of longwave radiation, net radiation and net energy budgets at the surface, which has proved problematic in current models (Banta et al. 2002).

F. MOTIVATION

Recent scientific literature has shown that Blackadar's inertial oscillation mechanism has remained the primary forcing behind LLJ dynamics, as was shown previously in this chapter. Thermal and topographical variations also lend significant contributions to fine tuning the dynamic solutions and geographical preference that characterize the LLJ, as was delineated in both Holton (1967) and Shapiro (2009). Qualitative field measurements analyzed in both the Klein (2015) and Banta (2002) studies have demonstrated that there is significant correlation between wind shear, stability, and TKE generation, and relative LLJ strength. While these findings have greatly advanced the understanding of the boundary layer response under LLJ influence,

insight into the intricate processes that occur within the lowest several tens of meters adjacent to the Earth's surface remain elusive. Because the surface layer can be viewed as a reflection of the deeper ABL, which is in turn also associated with processes in the free atmosphere, the motivation of this study is to incorporate qualitative, high-resolution data from the field into current analytical models in an effort to gain a better sense of LLJ-dominated surface layer processes.

THIS PAGE INTENTIONALLY LEFT BLANK

III. EXPERIMENT SETUP

A. SITE DESCRIPTION

The PECAN domain was comprised of multiple fixed and mobile PECAN Integrated Sounding Array (PISA) sites across much of Kansas, as well as portions of Nebraska and Oklahoma. The PECAN domain is depicted in Figure 13.

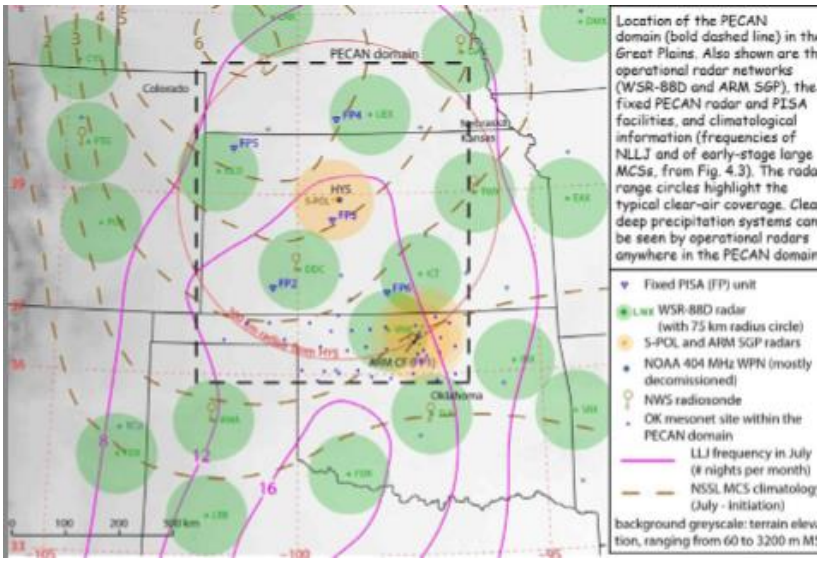

PECAN domain pictured above depicts various fixed PECAN Integrated Sounding Array (PISA), or FP sites. Also pictured are WSR-88D radar coverage circles (green), S-POL and Atmospheric Radiation Measurement (ARM) SGP radar coverage circles (gold), National Weather Service (NWS) radiosonde launch sites, Oklahoma Mesonet sites, and July LLJ and MCS climatology contours.

Figure 13. PECAN Domain. Source: NSSL (2015).

The team from the Naval Postgraduate School (NPS) established their data collection site at fixed PISA site #2, or FP-2. FP-2 was located on the eastern edge of the city of Greensburg, KS, which is in the southwestern corner of the PECAN domain approximately 45 miles east-southeast of the Dodge City, KS NWS station. The address of FP-2 was 211 S. Cottonwood Street, Greensburg, KS 67054 with a GPS location of 37°36’ 22.91”N and 99°16’ 26.40”W. The environment surrounding the collection site is characterized by the classic flat terrain and grassy stubble that comprises much of the Kansas high plains. All instrumentation was erected at sufficient distance from buildings,

trees, and other obstructions in order to extract accurate samples of the environment. The NPS team at FP-2 was collocated with teams from the University of Maryland-Baltimore County (UMBC) and NASA. A diagram of the location and layout of the experiment site is depicted in Figure 14.

Figure 14. Location and Experiment Site Layout for FP-2 in Greensburg, KS. Adapted from Google Earth.

B. INSTRUMENTATION

The NPS sensor array at FP-2 included a 16m main tower, a 6m flux tripod, and a 3m scalar tripod, all instrumented for turbulence and/or mean measurements. There was also a high frequency Doppler sodar, a ceilometer, a tethered balloon system with attached tethersondes and rawinsonde sensor package. The NPS team also made rawinsonde launches on selected days. Additionally, to augment the NPS measurements at low levels, we downloaded HRDL data and supplemental rawinsonde data collected at FP-2 by the collocated UMBC/NASA teams. The HRDL data was processed at NPS to obtain mean wind speed/direction and vertical velocity variance from lidar conical scans and vertical stare scans, respectively.

The 16m main flux tower was outfitted with four levels of turbulence and scalar perturbation measurements using 3-D sonic anemometer/LICOR combination or IRAGSON at 2.83m, 5.66m, 11.32m, and 16m. The turbulence and perturbations were sampled at 20Hz. In addition to the high-rate sensors, the 16m main tower was outfitted with two levels of mean wind, temperature, relative humidity, and pressure measurements using Vaisala WXT-520 weather stations at 10m and 14m. The 16m main tower was also equipped with twelve levels of naturally ventilated temperature and relative humidity

probes at 0.86m, 1.63m, 2.82m, 4.21m, 5.64m, 7.47m, 9.65m, 11.32m, 12.72m, 14.48m, 15.98m. The WXT-520 weather stations and temperature/relative humidity probes sampled and logged at a rate of 1Hz, with the averages of the parameters mentioned above also logged at 10 second, 1 minute, and 10 minute intervals. Figure 15 is a photograph of the fully outfitted 16m main tower.

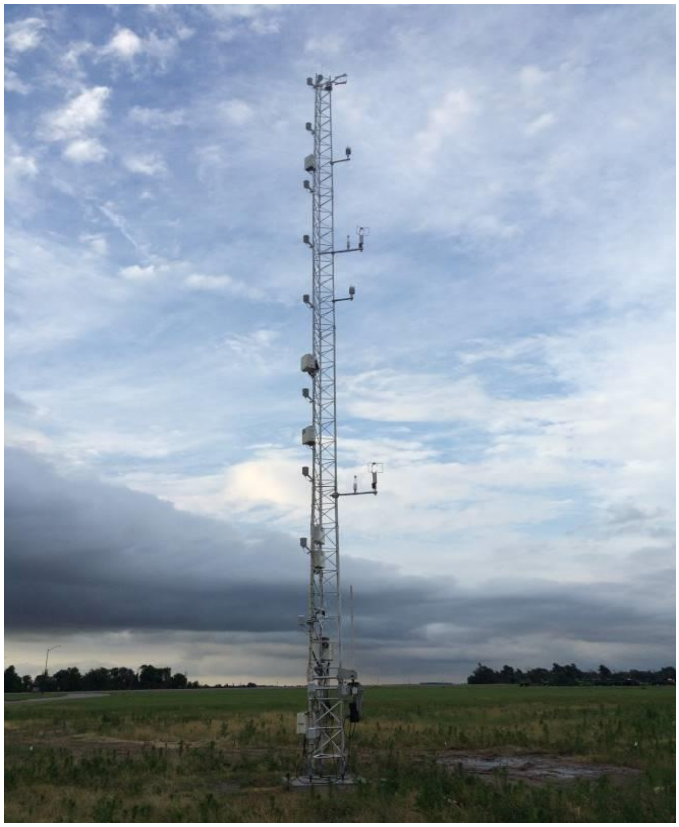

Figure 15. Outfitted 16m Main Tower

A 1.3m x 1.3m square concrete pad served as a stabilizing foundation for the 16m main tower. In order to mitigate any heating effects by the concrete foundation, a 6m flux tripod was constructed adjacent to the 16m main tower. The 6m flux tripod was equipped with two redundant levels of turbulence measurements using sonic anemometers at 2.83m and 5.66m, which were at the same levels as the lowest two levels of turbulence measurements on the 16m tower. These redundant flux measurements were used to better represent true turbulence quantities over the natural grassy surface. Temperature and relative humidity measurements at these two levels were also collected. The lowest level

2.83m sonic anemometer was also outfitted with a LiCor LI-7500 open-path infrared gas analyzer. All flux measurements were sampled and logged at 50Hz, while temperature and relative humidity data were sampled and logged at 1Hz, with the same parameter averages also saved at 1 and 10 minute intervals.

A 3m scalar tripod was also erected adjacent to the 16m main tower and 6m flux tripod. Mean aspirated temperature and relative humidity measurements were made at 0.114m, 0.1905m, 0.343m, 0.66m, 1.295m, 2.445m levels, while subterranean soil temperature was measured at -0.05m, -0.10m, and -0.25m and soil moisture at -0.10m and -0.25m. Shortwave solar irradiance and exitance measurements and longwave irradiance and exitance measurements were made using a Kipp and Zonen CNR1 instrument at 1.5m on the 3m scalar tripod. A tipping bucket rain gauge was also mounted at 1.5m. All data and associated means from the 3m scalar tripod were sampled and saved at 10 second, 1 minute and 10 minute intervals. A photograph of the 6m flux tripod and 3m scalar tripod can be found in Figure 16, with a closer view of the 3m scalar tripod in Figure 17.

Figure 16. 6m Flux Tripod and 3m Scalar Tripod

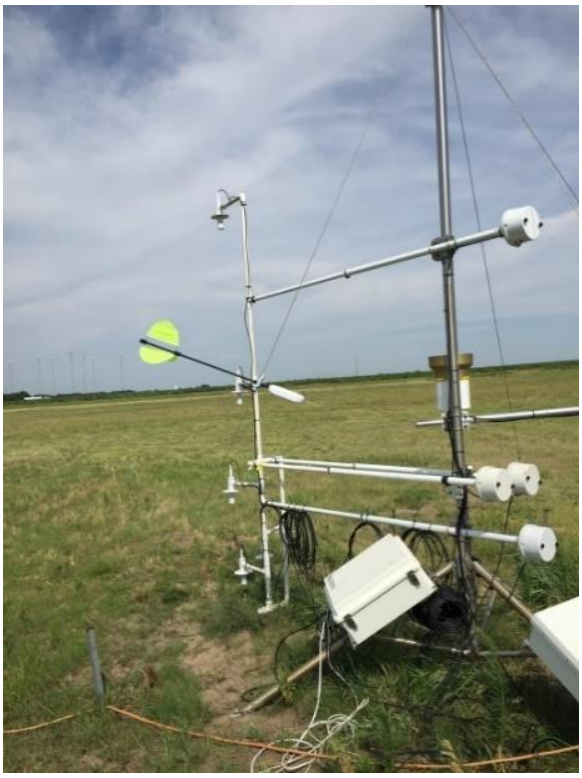

Figure 17. Closer View of 3m Scalar Tripod

The NPS team assembled an ASC (now merged with MetOne) model 4000 SODAR to obtain vertical profiles of wind speed, wind direction, turbulence, and 30 minute averages of these quantities. The SODAR had a pulse rate of 4500 Hz, a vertical resolution of 5m, and a data range of 20–260m with a maximum of 50 gates. Data returns were dependent on the level of mechanical turbulence in the boundary layer column and were reduced with higher ambient noise in the 4500Hz frequency range. Noise in this frequency range occurred with the presence of chirping birds and/or insects. A photograph of the Doppler SODAR can be found in Figure 18. Also included in the NPS fixed, continuous sensor array was a Vaisala CL31 laser ceilometer (not pictured) sampling to 7500m with 1550 range gates and a vertical resolution of 5m.

Figure 18. Doppler SODAR at FP-2

The NPS team employed the use of a hydraulic trailer winch and tethered balloon system to further sample the boundary layer column. Helikite balloons of volume 3.3m^3, 16m^3, and 34m^3 with 3mm tether line and attached Anasphere SmartTether 8.0M tethersonde were used to sample wind speed and direction, temperature, and relative humidity continuously starting just before sunset and concluding several hours before sunrise. In order to accurately capture the evening boundary layer transition, the winch control and tether line were released, allowing the helikite and tethersonde package to ascend to a desired height. Once this occurred, the winch was reengaged, resulting in a steady, controlled descent of the helikite/tethersonde package. This was repeated continuously starting just before sunset to capture the conclusion of the CBL, and ending several hours before sunrise to accurately capture the evolution of both the nocturnal temperature inversion and the formation of the LLJ. While taking measurements during PECAN, we found that the Anasphere tethersonde temperature and humidity sensors did not respond fast enough to satisfy the profiling measurements. The impact on the measurements was clearly evident in the vertical profiles of temperature and relative

humidity where the vertical variations of these parameters from the ascent and descent profiles were not consistent. In order to obtain reliable temperature and humidity measurements from the tethered balloon system, we added an iMet rawinsonde onto the tether line approximately 1m below the tethersonde 29 June 2015. In addition, the tethered balloon operation was limited to surface wind speed below 15 m/s, above which the Helikite that was used became rather unsteady. As a result, the deployment of the tethered balloon system was not on a daily basis, but instead used during nights when local wind speeds would allow a safe and stable deployment of the sensor package. Figures 19 and 20 are photographs of the tethered balloon system and Anasphere tethersonde, respectively.

Balloon System is shown with the Helikite and the balloon mooring arms on a trailer with hydraulic winch. A generator (seen on ground) was used to power the winch and work lights during night operations.

Figure 19. NPS Tethered Balloon System

Figure 20. Calibration of the Anasphere Tethersonde

In addition to the tethered balloon/tethersonde instrumentation package, the NPS team and UMBC/NASA team at FP-2 frequently made rawinsonde weather balloon launches using a Vaisala system with RS41 radiosondes over the course of the PECAN campaign. The NPS team supplemented the UMBC radiosonde launches during the second half of the campaign and used an up/down sounding approach. This was achieved by inserting a medical syringe into the balloon's opening and tying off the radiosonde line. Upon releasing the balloon, the balloon operator would remove the syringe plunger, allowing helium to escape at a slow rate. This allowed the balloon to ascend to an approximate, pre-determined height until the weight of the rawinsonde opposed the amount of lift provided by the balloon. When this occurred, the balloon would begin a slow descent to the surface. In this manner, the NPS team was able to obtain two successive vertical profiles of a column of desired thickness, which yielded multiple profiles through the nocturnal LLJ. The nozzle of the syringe was also cut to various

lengths as a nominal control of the helium leak, which further aided in achieving the desired height.

As previously mentioned, the NPS team obtained data collected by a Leosphere 200S high resolution Doppler lidar operated by the UMBC team at FP2. The UMBC lidar was positioned several hundred meters adjacent to the NPS experiment site at 37.605915°N and -99.275718°W. The Leosphere 200S obtained line of sight wind speeds derived from Doppler frequency shift in backscattered photons off atmospheric aerosols at a pulse rate of 10kHz and wavelength of 1.54 microns. The scan routine for the lidar was kept constant over the duration of PECAN, and is delineated in Table 1. The full runtime for the scan routine was around 20–25 minutes per cycle. Degrees in Table 1 are measured clockwise from the lidar compass heading, which is magnetic north. At different scan elevations, the lidar had maximum ranges of 3km, 6km, 12km, and 12km that correspond to range resolutions of 25m, 50m, 75m, and 100m, respectively. Line-of-sight lidar wind data was processed to obtain horizontal wind speed and direction from the PPI scan at five elevation angles and the vertical velocity mean and variance from the vertical stare. Data from the 45° elevation scan will be used in this thesis to take advantage of averaging over a smaller scanned volume.

Table 1. Scan Routine for Leosphere 200S during PECAN Campaign. Source: Delgado et al. (2016).

Iterations	Mode	Start Az. (°)	End Az. (°)	Start Elev. (°)	End Elev. (°)	Accumulation Time (s)	Speed (°/s)
1	PPI	0	360	5.0	-	1.00	2.5
1	PPI	0	360	7.5	-	1.00	2.5
1	PPI	0	360	10.0	-	1.00	2.5
1	PPI	0	360	20.0	-	1.00	2.5
1	PPI	0	360	45.0	-	1.00	2.5
1	RHI	80	-	0.0	60.0	1.00	2.5
1	RHI	80	-	60.0	0.0	1.00	-2.5
1	RHI	170	-	60.0	0.0	1.00	-2.5
1	RHI	170	-	0.0	60.0	1.00	2.5
600/300	LOS	0	-	90.0	-	1.00	-

THIS PAGE INTENTIONALLY LEFT BLANK

IV. RESULTS AND DISCUSSION

A. DATA OVERVIEW

The Leosphere 200S high-resolution Doppler lidar was able to provide the most meaningful insight into which nights were dominated by LLJ presence, which will be defined further in the sub-chapter entitled "Case Selection." Leosphere HRDL data was available from June 3 through July 14. Most days over the PECAN campaign include full lidar datasets with some exceptions. Days that included partial or incomplete lidar datasets include June 4, 8, 10, 12, 13, 14, 15, 18, 19, 23 and July 7, 9 and 13. Partial or incomplete datasets were found in both vertical and temporal domains. Some data was available for the entire time period on a given day, but was limited or cutoff above a certain height. Other datasets were robust for an appreciable vertical scale, but were incomplete temporally where data was missing over several hours on a given day. If any portion of the data available fit the definition of a LLJ described in the "Case Selection" sub-chapter, it was deemed a LLJ event.

Instruments on the 3-m scalar tripod were activated at 0000 UTC on 04 June and were decommissioned on 15 July at 2000 UTC. The Vaisala WXT-520 instruments and sonic anemometers affixed to the 16-m main tower came online on 14 June at 0000 UTC and were decommissioned at 0000 UTC on 14 July. Raw data from the scalar tripod, 16-m tower WXT-520s, and sonic anemometers on the 16m tower were averaged over 20 minute periods for the current analyses. The Doppler sodar became operational on 06 June at 0000 UTC and was taken offline at 0100 UTC on 16 July. Sodar data used in these analyses were the result of averaging raw data every 3 minutes.

Rawinsonde launches commenced on 31 May and ceased on 15 July. Anywhere between one and six soundings were completed each night during the campaign, with the first sounding of the night launched around 0000 UTC (1900 Local Time) and the final sounding launched around 0800 UTC (0300 Local Time).

Data that corresponds to a specific day within plots, tables, and text represents that day as it begins at 0000 UTC (1900 Local Time on the previous day) and ends at 2359 UTC (1859 Local Time on the day in question), unless otherwise noted. Sunset and

sunrise times mentioned within the analyses are also in UTC time. The earliest sunset time over the duration of the campaign was 0155 UTC (2055 Local Time on the day prior to the UTC day), while the latest sunset time was 0203 UTC (2103 Local Time on the day prior to the UTC day). Because the sunset time only varied by eight minutes over the course of the project, this thesis will use the median sunset time of 0159 UTC (2059 Local Time on the day prior to the UTC day). In a similar fashion, the earliest sunrise time was 1115 UTC (0615 local time) and the latest sunrise time was 1128 UTC (1128 Local Time). A median sunrise time of 1121 UTC (0621 Local Time) will be used for this "Results and Discussion" chapter.

This analysis used a blending of data from different sensors at FP-2 in order to depict profiles of different atmospheric parameters. The flux tower data accounts for the lowest 16m of the atmosphere, the SODAR accounts for data between 25m and approximately 200m, and the HRDL data accounts for wind speed and direction only from 50m AGL up through around 1500m AGL. Figure 23 shows different boundary layer profiles for 20 June, which was designated as a LLJ day, and is an example of a profile using a combination of data over multiple sensors. All data shown is valid for the time of maximum LLJ wind speed on 20 June.

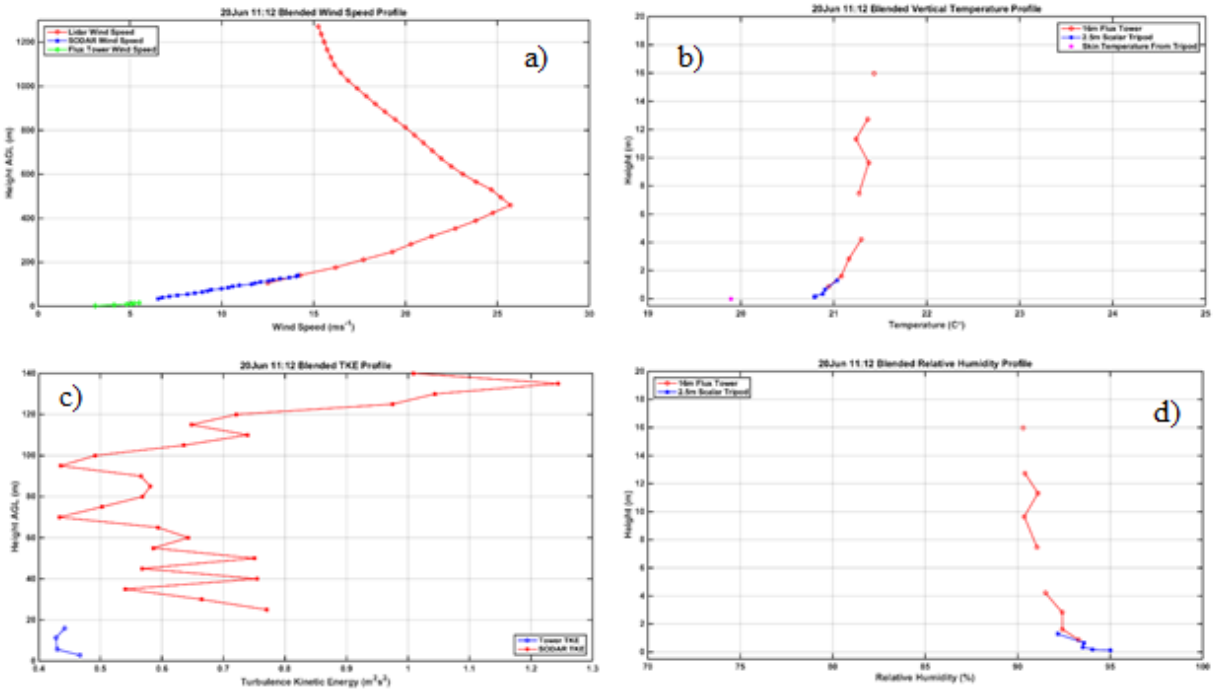

The graphs are a blending of sensor measurements from different AGL heights for a) wind speed profile using data from the flux tower, SODAR, and Leosphere HRDL, b) TKE using the 16m flux tower and SODAR, c) vertical temperature profile using data from the scalar tripod and 16m flux tripod, and d) vertical profile of relative humidity using data also from the scalar tripod and 16m flux tower.

Figure 21. Example of Vertical Profile Using Blended Data from Multiple Sensors

B. CASE SELECTION

LLJ definition varies from study to study with dependence on what particular application is being addressed as well as data set limitations. These data set limitations include horizontal and vertical spatial limitations, temporal limitations, and incomplete or erroneous datasets (Banta 2008). All LLJ definitions generally include requirements for a pronounced wind maximum falling somewhere between two height levels within the boundary layer, while other definitions place additional restrictions on LLJ criteria, such as vertical and temporal anticyclonic turning of the nocturnal ageostrophic wind vector on LLJ nights and winds flowing predominantly from a southerly sector (Klein 2015). For simplicity purposes and because this analysis is written as an initial look at the PECAN FP-2 dataset from a LLJ perspective, this thesis presents the occurrence of a LLJ

as defined by Andreas (2000), which states that, "If the wind speed profile shows a local maximum that is 2 m s^{-1} higher than speeds both above and below it, we call the feature a jet." Andreas points out that this definition follows the Stull (1988) criteria, which claims, "We will pragmatically define the LLJ as occurring whenever there is a relative wind speed maximum that is more than 2 m s^{-1} faster than wind speeds above it within the lowest 1500-m of the atmosphere." (Stull 1988) The Andreas (2000) modification differs only in the requirement of an elevated (i.e., not surface based) wind maximum. Following the Andreas (2000) definition, this analysis has identified LLJ wind speed maxima that are at least 2m s^{-1} higher than wind speeds below the level of the maximum and above the level of maximum up to a height where the wind speed retrieval data ends. The labeling of a LLJ night will hereafter be valid for the respective UTC day mentioned in any plot, table or portion of the text. This thesis will also include analysis of daytime atmospheric quantities with the intention of identifying possible LLJ formation factors for use in advancing prediction capabilities. All daytime analyses hereafter will apply to data collected on the UTC day prior to a LLJ night, as these atmospheric parameters ultimately constitute proxies for initial conditions entering a LLJ event.

One additional criterion that has been placed on case criteria is amply available data across all sensors. Significant incomplete datasets obtained at FP-2 during PECAN were found on 14 June, 23 June, and 29 June, rendering these days not usable. 0000 UTC on 14 June was the first day where data was available across all sensors, with the 16-m flux tower constituting the limiting factor in this determination. Because flux tower data was not available during the day on 13 June for use in daytime analysis, this data was omitted from the results. A significant amount of Leosphere HRDL data was missing on 23 June, and as such, this day was omitted as well. Finally, erroneous flux data from the flux tower's sonic anemometers on 29 June prevented the creation of a sufficient flux profile analysis for that LLJ event, and that day was omitted as well.

Figure 22 depicts a boundary layer snapshot using sampled FP-2 rawinsonde launches for the entire experiment period. It is important to note that the rawinsonde data is advantageous to use in gaining a coarse understanding of different parameters within the ABL, but because data processing of these soundings involved a significant amount

of interpolation between a few soundings on each night only, this data is to be interpreted with a certain degree of caution.

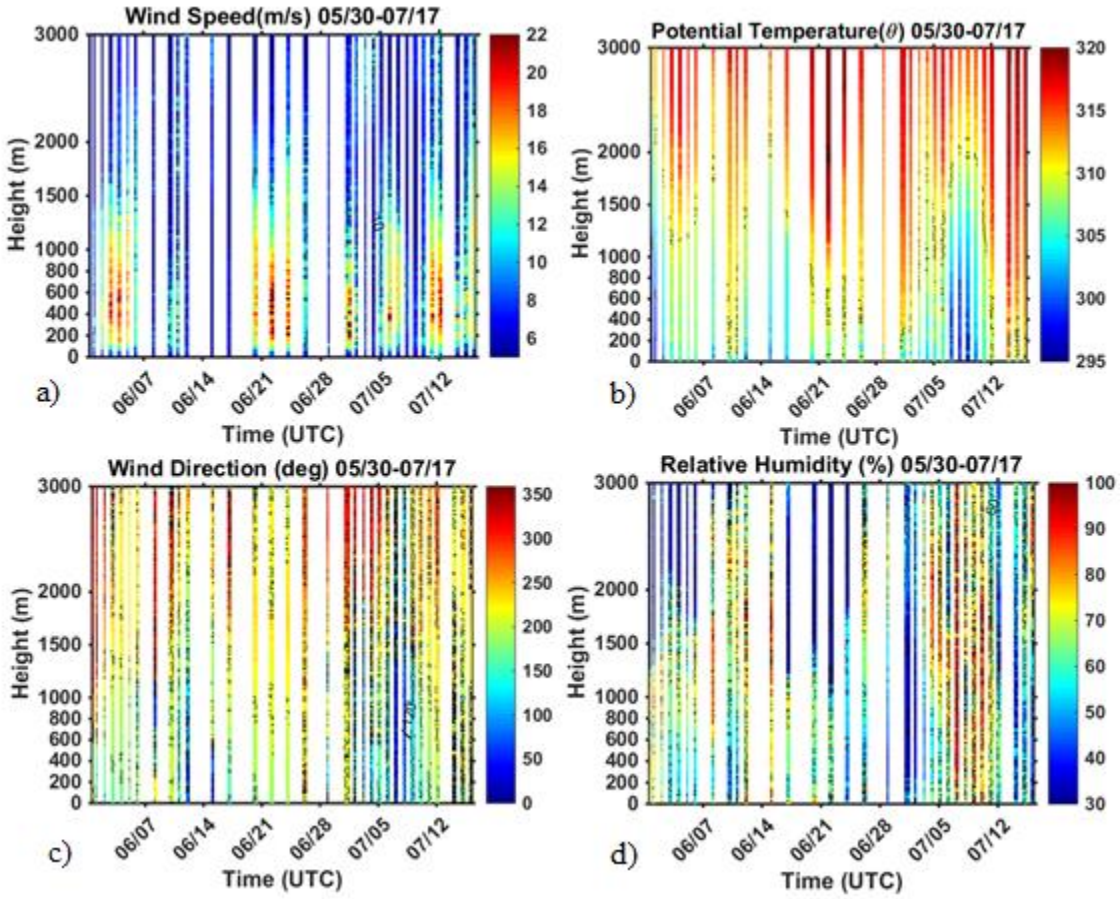

Figure depicts various nocturnal boundary layer parameters over the course of the PECAN campaign. Shown are a) wind speed in ms^{-1}, b) potential temperature in degrees K, c) relative humidity %, and d) specific humidity in g kg^{-1}.

Figure 22. FP-2 Boundary Layer Depiction from Nighttime Rawinsonde Measurements

The wind speed contour plot portrays a LLJ top of around 1000 m over the course of the project. Above the LLJ top, winds generally subside to values between 0 and 12 ms^{-1} and are likely good approximations of the geostrophic wind. A LLJ core, or the location of the LLJ maximum, can clearly be seen on several nights between 300m and 700m, with maximum speeds on some nights exceeding 16 m s^{-1}. It is also important to notice a very shallow layer of weaker surface layer winds beneath the lower extent of the

LLJ on almost every LLJ night. In Figure 22b, the potential temperature variation reveals a distinct low-level cool layer with an approximate upper bound that correlates well with the LLJ top at around 1000 m. Above this cool layer, warmer temperatures abound with some vertical temperature gradients of 5–10 degrees K. These temperature inversions are quite typical of nocturnal terrestrial temperature profiles and are the result of significant radiative cooling initiated at the cessation of incoming shortwave solar radiation. Figure 22c represents boundary layer wind direction throughout the PECAN experiment period. In Figure 22d, the plot of relative humidity illustrates a pronounced moist layer in the lower ABL with a top limit that also correlates well with the LLJ top on most LLJ nights. This lower-level moist layer is a result of a decreasing dew point depression as the boundary layer cools which enhances the ambient moisture profile.

Since the rawinsonde launches were released only intermittently through most nights and the subsequent plots are mere interpolations of the parameters discussed previously, individual LLJ evolution for a given night is better identified using the continuous HRDL data. Figure 23 is a collection of contour plots that portray the low level horizontal wind field during PECAN, and is very useful for LLJ event identification.

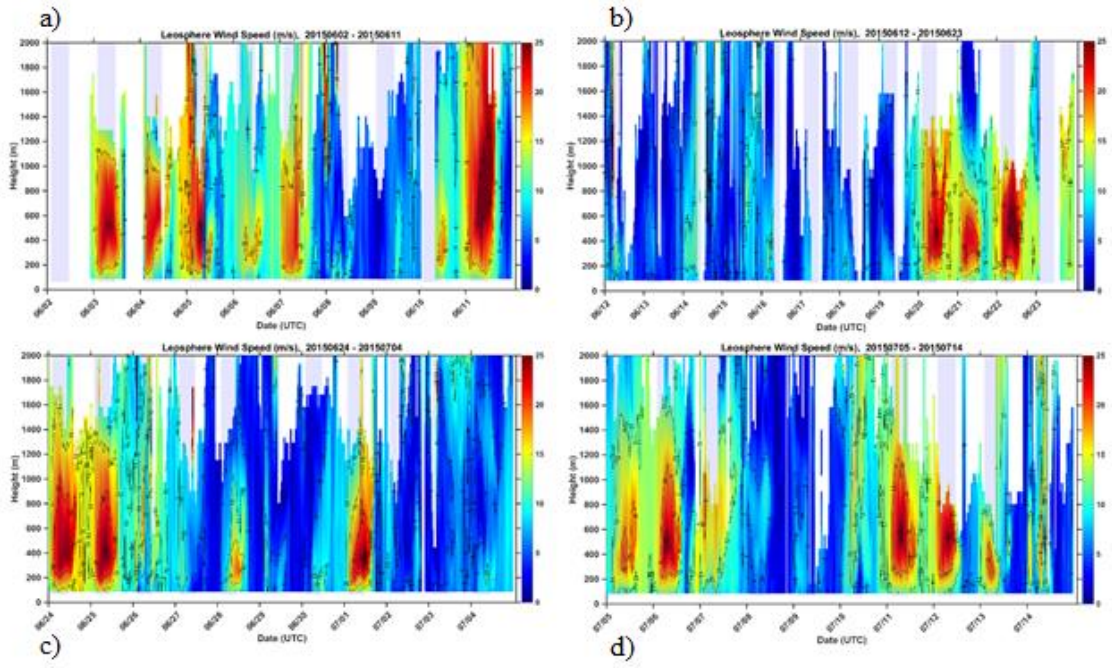

Continuous wind speed measurements at FP-2 were made using the Leosphere 200S HRDL during PECAN and were subsequently used to identify LLJ events according to criteria defined in Andreas (2000). Shown are wind speed measurements between a) 02 June and 11 June, b) 12 June and 23 June, c) 24 June and 04 July and d) 05 July and 15 July.

Figure 23. Plot of Leosphere 200S HRDL Wind Speed as a Function of Time and Height at FP-2 during PECAN.

LLJ characteristics are much better defined in the contour plots of HRDL data. The days with pronounced wind maxima are clearly seen with the orange and red colors, but other days are less obvious. LLJ events indicated by the HRDL with wind maxima greater than 15 ms^{-1} have been denoted as strong LLJ days and include 03–05 June, 07 June, 11 June, 20–22 June, 24–26 June, 28 June, 01 July, 05–07 July, and 10–13 July. Other LLJ events are less obvious, but fall under the criteria of 2 ms^{-1} greater than levels above and below. These LLJ events are characterized by wind maxima less than 15 ms^{-1} and include 16 June, 18 June, 27 June, 04 July, and 08 July. LLJ ceilings range from 350 m with weaker cases like 04 July, up to heights of greater than 1500 m as was observed with the strong 11 June case. Most observations of LLJ top are consistent with the rawinsonde observations of around 1000 m. LLJ core heights generally vary between 400m and 700m. As mentioned previously, because the 16-m flux tower was not fully operational until 14 June, several of the earlier LLJ days detected by HRDL were

omitted. These days include 03–07 June, 09–12 June, and 14 June. The first day of the LLJ dataset for this analysis was 16 June.

C. SURFACE LAYER RESPONSE UNDER LLJ INFLUENCE

Table 2 provides a comprehensive list of all days in which a LLJ was observed, along with relevant boundary layer measurements and calculations for each event.

Table 2. Table of LLJ Events and Associated Boundary Layer Quantities

Date	U_g	U_{LLJ}	$U_{16m,jet}$	$U_{6m,jet}$	U_{LLJ} Time (UTC)	Z_{LLJ}	U_{LLJ}/Z_{LLJ}	U_{LLJ}/U_g	U_{LLJ}/U_{6m}	U_{16m}/U_{6m}	$Ri_{B,night}$	$Ri_{B,day}$	$U_{t,day}$	$(U_t/U_{6m})_{day}$	$U_{t,night}$	$(U_t/U_{6m})_{night}$	Minimum $(T_{2.5m}-T_{sfc})_{day}$	Maximum $(T_{2.5m}-T_{sfc})_{night}$	$[(T_{2.5m}-T_{sfc})_{night}]$ -$[(T_{2.5m}-T_{sfc})_{day}]$	Minimum $(T_{16m}-T_{sfc})_{day}$	Maximum $(T_{16m}-T_{sfc})_{night}$	$[(T_{16m}-T_{sfc})_{night}]$ -$[(T_{16m}-T_{sfc})_{day}]$
16-Jun	8.14	12.22	4.49	3.27	3:45	283	0.04	1.50	3.74	1.37	0.47	-0.02	1.16	0.21	0.23	0.26	-4.08	1.21	5.30	-4.82	1.58	6.40
18-Jun	5.15	11.60	4.73	3.25	3:56	177	0.07	2.25	3.57	1.46	0.25	-0.97	1.04	0.34	0.23	0.15	-5.38	1.32	6.70	-5.84	1.50	7.34
20-Jun	9.86	25.71	5.51	4.14	11:12	460	0.06	2.61	6.21	1.33	0.06	-0.36	1.14	0.21	0.57	0.15	-9.09	1.47	10.57	-9.99	1.68	11.66
21-Jun	14.51	23.50	7.45	5.75	6:02	389	0.06	1.62	4.08	1.29	0.03	-0.02	1.76	0.17	0.85	0.16	-5.80	1.65	7.46	-6.58	1.77	8.35
22-Jun	12.85	26.80	7.67	6.08	8:39	530	0.05	2.09	4.40	1.26	0.02	-0.05	1.38	0.17	0.87	0.17	-8.08	1.45	9.53	-9.34	1.58	10.93
24-Jun	14.15	24.64	8.89	7.42	6:48	318	0.08	1.74	3.32	1.20	0.02	-0.10	1.56	0.18	0.93	0.14	-9.38	1.77	11.16	-10.62	2.10	12.72
25-Jun	15.06	25.50	7.47	6.16	8:36	389	0.07	1.69	4.14	1.21	0.02	-0.08	1.74	0.17	0.93	0.15	-9.25	1.85	11.10	-10.57	2.31	12.89
26-Jun	9.65	19.09	4.43	2.74	6:19	707	0.03	1.98	6.97	1.62	0.40	-0.19	1.36	0.19	0.66	0.20	-10.81	1.76	12.57	-12.01	2.86	14.88
27-Jun	8.94	11.64	4.36	2.82	4:52	247	0.05	1.30	4.12	1.54	1.62	-0.05	1.92	0.25	0.19	0.18	-13.63	2.68	16.30	-14.94	3.29	18.23
28-Jun	2.82	19.48	4.05	2.80	11:12	283	0.07	6.90	6.95	1.44	0.18	-1.22	1.30	0.54	0.46	0.15	-18.45	1.73	20.17	-19.16	2.97	22.13
1-Jul	7.76	25.81	6.85	5.39	11:04	318	0.08	3.33	4.79	1.27	0.10	-0.36	1.34	0.22	0.75	0.15	-12.40	1.92	14.31	-13.72	2.31	16.03
4-Jul	8.24	11.37	3.41	2.44	9:22	247	0.05	1.38	4.67	1.40	0.21	-0.37	1.26	0.26	0.32	0.15	-16.44	1.92	18.36	-17.50	2.99	20.48
5-Jul	7.26	20.63	4.82	3.85	9:07	460	0.04	2.84	5.36	1.25	-0.01	-0.49	1.26	0.21	0.67	0.14	-14.00	0.98	14.99	-15.54	1.16	16.70
6-Jul	12.82	25.61	8.61	7.34	7:14	530	0.05	2.00	3.49	1.17	0.02	-0.11	1.52	0.16	1.01	0.15	-10.41	1.49	11.90	-11.87	1.68	13.56
7-Jul	7.16	20.23	9.38	7.84	2:29	742	0.03	2.83	2.58	1.20	0.00	-0.29	1.45	0.21	2.22	0.27	-12.34	0.76	13.10	-13.22	1.15	14.37
8-Jul	6.97	10.52	3.21	1.85	9:36	778	0.01	1.51	5.68	1.73	1.51	-0.19	1.23	0.18	0.27	0.20	-12.41	1.26	13.67	-13.75	2.17	15.92
10-Jul	5.06	16.16	4.49	3.60	7:05	778	0.02	3.19	4.48	1.24	0.44	-1.09	0.79	0.25	0.60	0.37	-16.06	0.68	16.74	-17.25	0.82	18.07
11-Jul	11.61	25.54	6.86	5.44	7:39	530	0.05	2.20	4.69	1.26	0.03	-0.19	1.22	0.17	0.60	0.13	-6.76	1.75	8.51	-7.91	1.91	9.81
12-Jul	13.33	24.73	6.98	5.60	7:24	530	0.05	1.86	4.42	1.25	0.02	-0.12	1.45	0.16	0.64	0.13	-9.18	1.62	10.80	-10.98	1.93	12.92
13-Jul	8.68	20.36	4.82	3.29	5:31	283	0.07	2.35	6.19	1.47	0.06	-0.76	1.07	0.22	0.57	0.14	-12.70	1.79	14.49	-13.82	2.21	16.03

This table lists dates for all LLJ events determined using Andreas (2000) criteria and supplemented with relevant boundary layer measurements and calculations obtained from fully operational sensors at FP-2 during the PECAN campaign. See text for measurement and calculation explanation.

Shown in the first column are all days where LLJ presence was observed according to the criteria outlined in Andreas (2000), where a LLJ was determined to have occurred if the wind speed maximum between sunset and sunrise on a given day was at least 2 ms^{-1} greater than speeds both above and below the height of wind speed maximum. The subsequent analysis yielded 20 LLJ events. The second column, denoted by "U_g," is a representation of the geostrophic wind. Generally, the geostrophic wind is representative of the pressure field over a given area and is most accurately depicted using measurements obtained from multiple locations over an experiment domain. As such, accurate geostrophic wind representations at a single point are difficult to measure. For the current analysis, the geostrophic wind is represented as the mean wind speed above 800m AGL between 1700 UTC (1200 Local Time) and sunset. This representation is similar to that described in Klein (2015) in which the scaling velocity U_s is obtained using the mean wind measurement between 800m AGL and the height at which data retrieval ends between 1730 and 1830 Local Time. For the current analysis, the time period between 1200 local time and sunset was chosen to account for the full development of the afternoon CBL, which has meaningful influence over the ambient geostrophic wind. Geostrophic wind speeds measured at FP-2 ranged from 2.82 ms^{-1} to 15.06 ms^{-1}, with a mean value of 9.50 ms^{-1}. The third column, denoted by "U_{LLJ}," is the wind speed maximum between sunset and sunrise on a given night and represents the LLJ nose. The maximum height considered for jet nose occurrence on LLJ nights was 1500 m AGL, as low-level wind maxima at or above this height were virtually non-existent. The highest LLJ wind speed that occurred over the period was 26.80 ms^{-1} on 22 June, while the lowest LLJ wind speed observed was 11.04 ms^{-1} on 08 July. The average LLJ wind speed maximum at FP-2 during the project was 20.16 ms^{-1}.

The fourth and fifth columns depict the 16-m and 6-m wind speeds, respectively, that occurred at the same time as a wind speed maximum on a given LLJ night. These quantities were obtained from mean wind speed measurements on the 16-m flux tower. The selection of the 6 m and 16 m levels on the flux tower were not arbitrary, but were chosen due to their collocation with sonic anemometers at the same levels. The turbulence measurements obtained from the sonic anemometers will be used later in the

analysis. In the Klein (2015) study discussed earlier, mean wind measurements and turbulence measurements were made at the top tower level of 80 m, and at 37 m, a level roughly half the height of the 80-m instrument. In keeping with the focus on the nocturnal surface layer in the current study, the top tower height at FP-2 was 15.98 m (rounded to 16 m in this thesis for simplicity purposes), with the 5.64 m (also rounded to 6 m for simplicity purposes) level being the nearest to one-half of the 16m level measurements, while also maintaining the capability to measure both the mean wind and turbulence quantities throughout the experiment. A sensor suite at 10 m was higher than the requisite one-half tower height and did not make turbulence measurements throughout the campaign, while the 2.8245m sensor suite did make both mean wind and turbulence measurements, but was significantly less than one-half of the tower height, hence why measurements from 6m were chosen for the current analysis.

The sixth and seventh columns, denoted by "U_{LLJ} Time" and "Z_{LLJ}" respectively, are the UTC time and AGL height of the wind speed maximum U_{LLJ} on a LLJ night. Wind speed maxima on LLJ nights occurred as early as 0229 UTC (2129 Local Time) and as late as 1112 UTC (0612 Local Time) with the majority of cases occurring between 0600 and 0900 UTC (0100 and 0400 Local Time). The height of LLJ wind speed maxima ranged from 247 m AGL to 1025 m AGL, with a mean jet nose height of 520 m AGL.

The eighth column is denoted by "U_{LLJ}/U_g" and is the ratio of the nightly LLJ wind maximum to the geostrophic wind measured between 1700 UTC (1200 Local Time) and sunset during the previous afternoon's CBL evolution, as found in the second column. This quantity is intended to serve as a measurement of the relative intensity of the LLJ wind maximum to a previous day scaling velocity, and is adapted from the quantity U_{LLJ}/U_s found in Klein (2015). Klein suggests that, instead of examining various boundary layer parameters against the actual LLJ wind maximum on a given night, it may be more practical to investigate these parameters against a relative LLJ intensity. The highest U_{LLJ}/U_g observed during the PECAN campaign was 6.90 on 28 June, while the lowest observed relative LLJ intensity was 1.30 on 27 June. It is important to note that the highest LLJ intensity of 6.90 does not correlate to the highest actual observed LLJ wind maximum 26.80 ms^{-1}, and subsequently, the lowest LLJ intensity of 1.30 does

not correlate to the lowest observed relative LLJ intensity of 11.04 ms^{-1}. Several wind shear calculations were also made for comparison purposes with different boundary layer parameters. U_{LLJ}/U_{6m} is the ratio between the maximum LLJ wind and the 6 m mean wind at the same time as the jet maximum. U_{16m}/U_{6m} is the ratio of the 16-m mean wind to the 6-m mean wind at the same time as the jet maximum.

The NPS team at FP-2 also made several stability and turbulence calculations for use in correlating the previously mentioned LLJ-influenced, height varying mean wind speeds and shear parameters. The team used Equation (14), as was defined in the Klein (2015) study, for computing bulk Richardson number. This equation can be found in the "Background" chapter. Values in the column denoted by "$Ri_{B,\text{night}}$" were the maximum bulk Richardson number values (most stable) on a given LLJ night between 0700 UTC (0200 Local Time) and 0900 UTC (0400 Local Time). This time range was chosen primarily because nocturnal thermal stability does not appreciably change throughout the night and this timeframe revealed the most stable Ri_B values as well as the lowest magnitudes of sensible heat flux. Values in the column marked "$Ri_{B,\text{day}}$" were the minimum bulk Richardson number (most unstable) occurring between 1800 UTC (1300 Local Time) and 2000 UTC (1500 Local Time) during the previous day leading up to a LLJ night. This time period was justified because daytime Ri_B values were found to be the most negative during this period and sensible heat flux was at a maximum, revealing stability at the time of the day of maximum surface heating.

In addition to stability as determined by Richardson number, turbulence parameters were also calculated in an attempt to draw correlation between the diurnal variation in surface layer turbulence and LLJ wind maxima relative to LLJ wind intensities, and various shear parameters mentioned previously. Similar to Klein (2015), turbulence quantities U_t were calculated according to Equation (13). It is important to note that the square of U_t is the TKE. *U*, *V*, and *W* variances were obtained from the sonic anemometer positioned at the 6-mlevel on the flux tower. This level was chosen to better characterize surface layer turbulence under LLJ influence, and due to the fact that mean wind measurements were collected at the same level. The column denoted $U_{t,\text{day}}$ contains the average turbulence strength between 1800 UTC (1300 Local Time) and 2000 UTC

(1500 Local Time) on the afternoon prior to the LLJ night in question. This time period was chosen to capture the average of the strongest daytime turbulence within the CBL of the previous afternoon. The column denoted by $(U_t/U_{6m})_{\text{day}}$ contains the average turbulence ratio calculated between 1800 UTC and 2000 UTC turbulence and the average 1800 UTC-2000 UTC U_{6m} wind speeds. This quantity serves as an average measure of turbulence intensity relative to the ambient mean 6 m wind speed during the afternoon hours prior to the onset of the stable nocturnal surface layer. The column denoted $U_{t,\text{night}}$ contains the average turbulence calculation between 0700 UTC (0200 Local Time) and 0900 UTC (0400 Local Time) of the LLJ night in question, while the column denoted by $(U_t/U_{6m})_{\text{night}}$ contains the average nighttime turbulence ratio between 0700 UTC-0900 UTC and average U_{6m} wind speeds between 0700 UTC-0900 UTC. The latter quantity serves as an average measure of nocturnal turbulence intensity relative to the ambient mean 6-m wind speed during the most stable portion of the nocturnal stable surface layer regime.

Thermal stability was also taken into account in examining the relationship between surface layer response and LLJ wind maxima, LLJ intensity, and various shear parameters. This analysis examines thermal stability between 16 m and the surface, and between 2.5 m and the surface. The latter calculations were made because the largest gradient in surface layer temperature often occurs in this lowest several meters adjacent to the Earth's surface. "Minimum $(T_{2.5m}\text{-}T_{sfc})_{\text{day}}$" corresponds to the most negative temperature difference between the 2.5m temperature and the temperature at the surface, which is also known as the skin temperature. These measurements were obtained from the 2.5 m scalar tripod between 1700 UTC (1200 Local Time) and sunset on the day prior to the LLJ night in question. The most negative daytime temperature difference between these two levels generally corresponds to the time of the day characterized by maximum surface heating, hence why this time period was chosen. The column denoted as "Maximum $(T_{2.5m}\text{-}T_{sfc})_{\text{night}}$," is the largest magnitude temperature difference between the 2.5-m temperature and skin temperature between sunset and sunrise of the LLJ night being examined. This quantity generally corresponds to the time of night when the surface temperature is at its coolest, and when the temperature inversion at 2.5 m is the

strongest. The column denoted "[$(T_{2.5m}\text{-}T_{sfc})_{night}$]-[$(T_{2.5m}\text{-}T_{sfc})_{day}$]" depicts the difference between the minimum change in temperature between 2.5m and the surface during the day prior to a LLJ event and the maximum change in temperature between 2.5m and the surface during the night characterized by a LLJ event. This quantity can be described as the maximum temperature differential below 2.5 m AGL between 1700 UTC (1200 Local Time) on the day prior to a LLJ event and sunrise on the morning following the same LLJ event. Similarly, "Minimum $(T_{16m}\text{-}T_{sfc})_{day}$" corresponds to the most negative temperature difference between the 16 m temperature and the temperature at the surface between 1700 UTC (1200 Local Time) and sunset on the day prior to the LLJ night in question, while the column denoted as "Maximum $(T_{16m}\text{-}T_{sfc})_{night}$" is the largest magnitude temperature difference between the 16-m temperature and skin temperature between sunset and sunrise of the LLJ night being examined. Finally, the column denoted "[$(T_{16m}\text{-}T_{sfc})_{night}$]-[$(T_{16m}\text{-}T_{sfc})_{day}$]" depicts the difference between the minimum change in temperature between 16 m and the surface during the day prior to a LLJ event and the maximum change in temperature between 16 m and the surface during the night characterized by a LLJ event.

The blending of data from multiple sensors allowed the NPS team to take advantage of the different sensors and gain valuable insight into altitude-varying wind speed behavior associated with the LLJ. Figure 24 is a time series plot of winds speeds from multiple levels within the boundary layer.

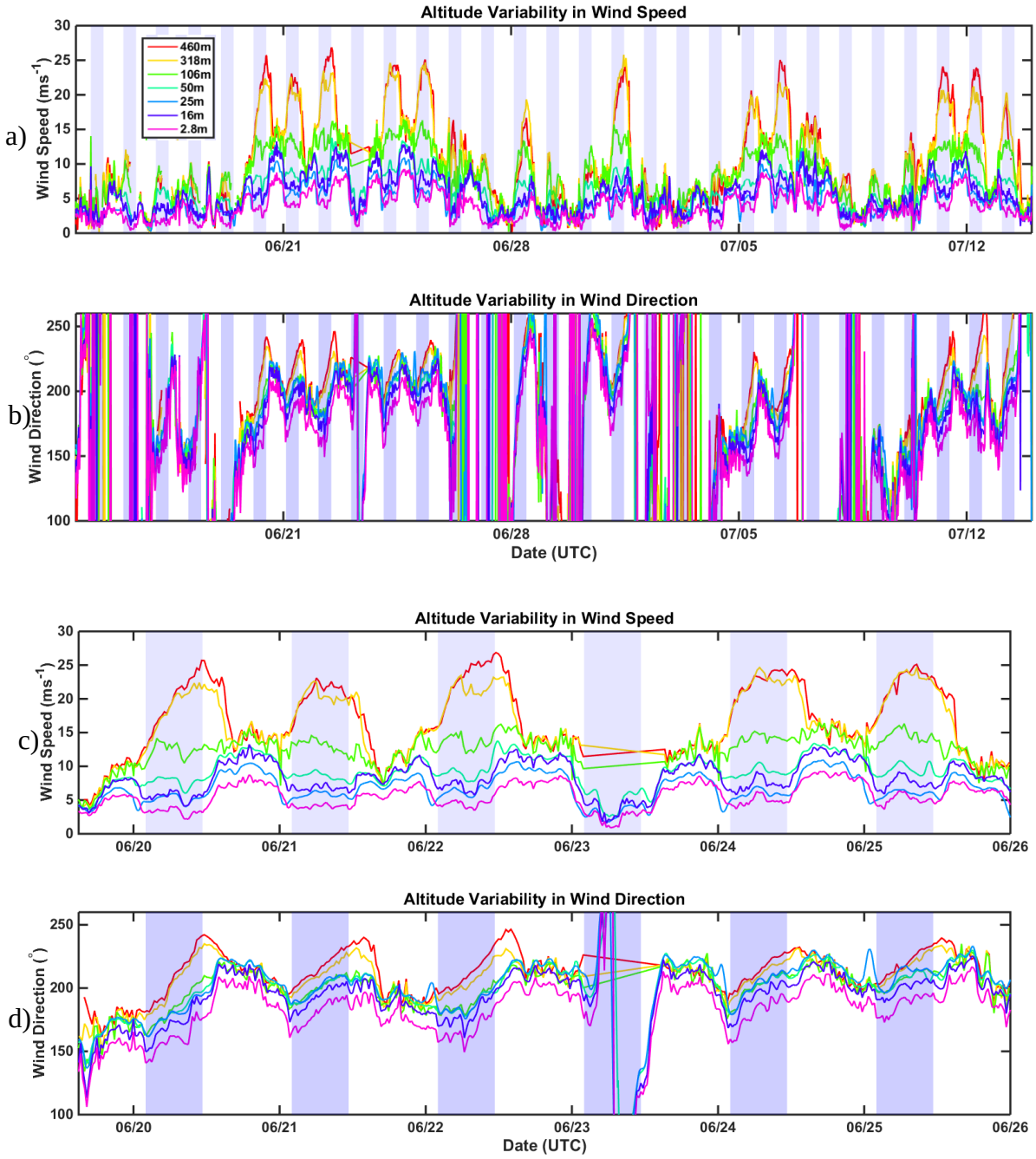

Time series for a) wind speed, b) wind direction for the full period, c) a zoomed-in view of wind speed and d) wind direction over the course of several successive LLJ days. Purple shading represents the time of the day between sunset (0159 UTC) and sunrise (1121 UTC) in order to show the diurnal nature of various mean wind profiles.

Figure 24. Altitude Variability in Wind Speed

1. Wind Speed Variability

Figure 24 portrays the time evolution of the mean wind at several representative levels below 500 m. In Figure 24a, strong LLJ days can be clearly distinguished among weaker LLJ days and non-LLJ days with the distinct peak in wind speed. A closer examination of the full period time series depicts higher than normal surface layer winds during the nocturnal period under the presence of a LLJ than LLJ-free days. Additionally, the wind direction variation in Figure 24b has been centered at 180° to illustrate the predominant wind direction under the influence of the nocturnal LLJ. Strong LLJ nights are largely characterized by southerly winds ranging anywhere between 150° and 250°. Shifting attention to Figure 24c reveals a marked variation of wind speed with altitude for wind profiles under LLJ influence on 20–26 June. Wind speeds were observed at 2.8 m, 16 m, 25 m, 50 m, 106 m, 318 m, and 460 m throughout the period. Winds just above the surface layer at 106 m do not vary much throughout each nocturnal period and represent a rough median value of winds above and below this level. Altitude-varying wind speeds throughout the daytime period do not exhibit very much spread, but diverge greatly around the time of sunset on LLJ nights. On the observed LLJ nights, the 318 m and 460 m winds increase drastically around the time of sunset while the surface layer winds at 50 m, 25 m, 16 m, and 2.8 m decrease simultaneously. This result is a very interesting observation, as it seems that the surface layer winds and upper boundary layer winds progress almost entirely out of phase throughout a LLJ night. The 460 m and 318 m winds peak during the second half of the nocturnal period and occasionally at or after sunrise, while the surface layer winds remain in a decreased, nearly constant value. Surface layer wind speeds and higher boundary layer wind speeds begin to converge once again following the recommencement of the daytime CBL after sunrise. Higher boundary layer winds drop significantly and surface layer winds climb slightly to converge to within a 10 ms^{-1} wind speed difference from 460m down to the surface. Closer inspection of Figure 24d also shows that LLJ-influenced wind direction usually begins from the south-southeast around sunset and rotates anticyclonically throughout the night, often reaching a west-southwesterly direction by sunset before rotating cyclonically upon the

onset of the CBL. This veering of the wind vector with time has been widely observed in previous studies and verifies expected results.

It is also important to note that the divergence of surface layer wind speeds from the higher boundary layer wind speeds on a LLJ night may occur up to an hour or more before sunset and re-converge up to an hour or more after sunrise. Figure 25 suggests why this may occur.

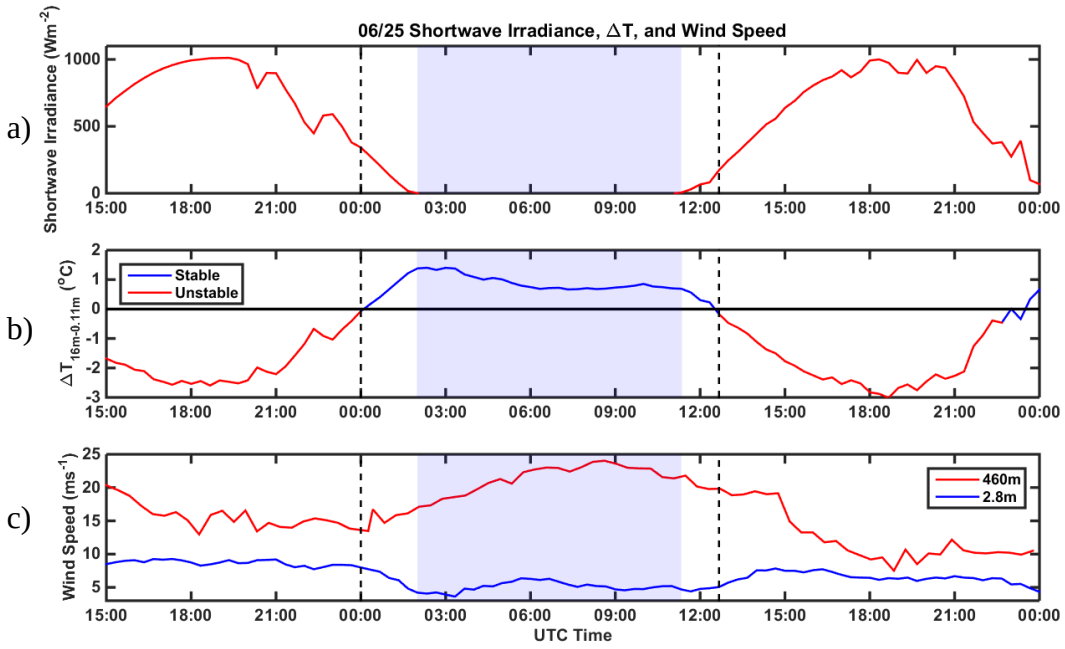

25 June time series of a) incoming shortwave solar radiation, b) temperature difference between 16 m and 0.11 m AGL, and c) the 460-m and 2.8-m wind speeds. Blue coloring in b) represents stable thermal stability while red coloring represents unstable thermal stability. The blue line in c) represents the 2.8 m wind speed while the red line represents 460-m wind speeds. The purple shading corresponds to the time period between sunset and sunrise and the black dashed lines indicate the changeover from negative (unstable) thermal stability to positive (stable) thermal stability.

Figure 25. Plots of Shortwave Irradiance, ΔT (16 m-0.11 m), and 460-m and 2.8-m Wind Speeds for 25 June

In Figure 25a, the incoming shortwave solar radiation diminishes at the time of sunset and begins increasing at sunrise, as expected. Many previous studies have explained LLJ occurrence between the bounds of sunset and sunrise. Figure 25 shows

that the upper boundary layer wind speed increases begin well before sunset and remain for several hours after sunrise. Likewise, surface layer winds begin to decrease several hours prior to sunset and begin to increase well after sunrise. Based on an inertial oscillation-induced LLJ theory, these results emphasize the Blackadar (1957) findings where a sudden cessation of surface momentum flux (or friction) occurs, allowing parcels to accelerate and oscillate more freely while rotating counterclockwise in the Northern Hemisphere due to Coriolis force. Figure 25 suggests that frictional release occurs well before sunset and persists well after sunrise as indicated by the onset of stable thermal stratification, resulting in significantly reduced friction, a condition necessary to increase the wind speed at levels above 100 m, and hence the presence of the LLJ. The time of transition from unstable thermal stability to stable thermal stability can be seen in Figure 25b as indicated by ΔT crossing the black dashed line. This transition time also appears to correspond closely with the time of wind speed separation between the winds in the surface layer and those above, as well as the time when wind speed from different levels converge after sunrise on the following morning (Figure 25c).

2. Thermal Stability

In addition to considering the thermal stability transition as a driver for the commencement of LLJ formation, it is also useful to examine the temporal variation of thermal stability over the experiment period as it relates to above-surface-layer wind speeds during LLJ events. Figure 26 illustrates the effect LLJ events have on surface layer thermal stability.

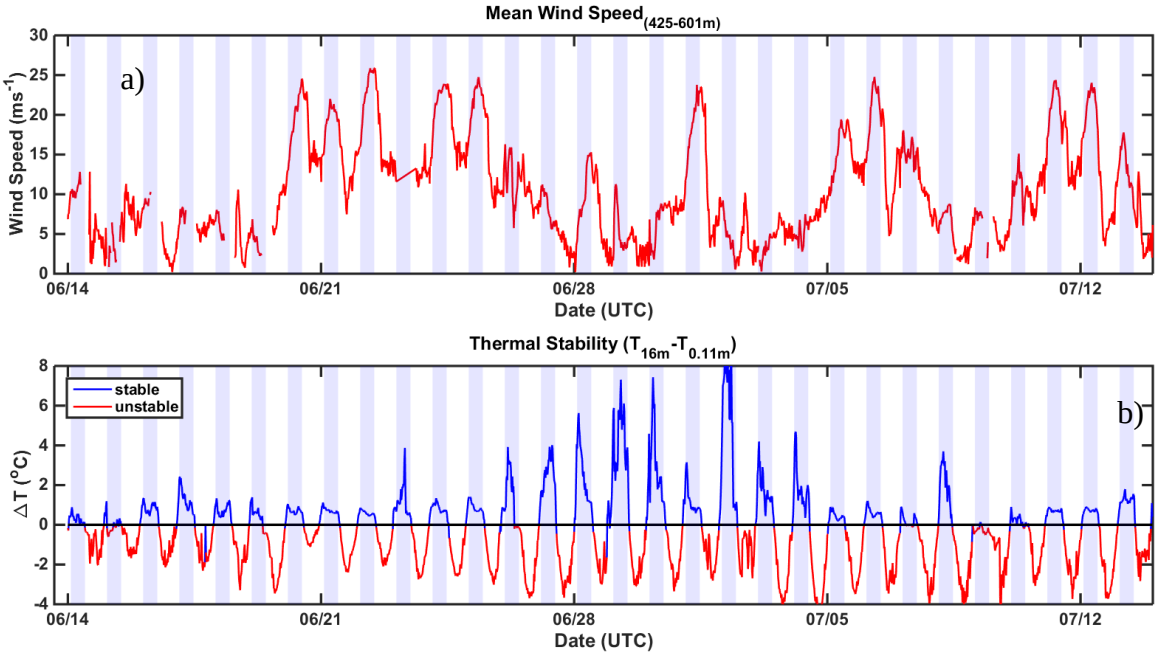

In this plot, a) depicts mean winds between 425 m and 601 m over the entire period, while b) depicts the surface layer temperature difference between 16 m and 0.11 m. The blue line denotes stable regime ($\Delta T>0$) while the red line denotes unstable regime ($\Delta T<0$). Purple shading represents the time period between sunset and sunrise.

Figure 26. Temporal Variations of Mean Wind Between 425 m and 601 m and Surface Layer Thermal Stability

The diurnal variation in thermal stability can be easily seen in Figure 26b. The range of variation of thermal stability (blue) is larger than that of thermal instability (red). Stable values range from less than 1 degree up to 8 or more degrees Celsius. In addition, Figure 26 seems to show high correlation between weak stable stratification and large magnitude of LLJ wind speed. The data from 20–22 June, 24–25 June, 01 July, 05–06 July, and 11–12 July are all characterized by upper boundary layer winds in excess of 20 ms^{-1} with relatively small vertical temperature differences in the surface layer. Each of these nights had nocturnal inversions of 2°C or less with the exception of 01 July, which had an inversion strength of about 3°C. Conversely, nights with the strongest inversions tended to lack LLJ wind maxima. Results from 30 June and 02 July are excellent examples of nights with strong surface layer inversions and a distinct absence of a pronounced jet-like wind maximum. Inversions on these two days were on the order of

7°C or more, with corresponding mean wind speeds between 425 m and 601 m of 10 ms^{-1} or less. Therefore, it would appear that the nominal nocturnal inversion strength with the presence of a LLJ is 2°C or less, such that a weak thermally stable surface layer is the dominant regime. These findings tend to agree with numerical simulations presented in Shapiro (2009) where, for a weak initial component of the geostrophic wind speed V_o, a terrain-slope angle of around 0.2 degrees (which is not consistent with the terrain slope at FP-2), and a weak capping inversion, the strongest values of the maximum ageostrophic wind speed V_{max} also tend to occur. Figure 8 in the "Background" chapter provides a review of this concept.

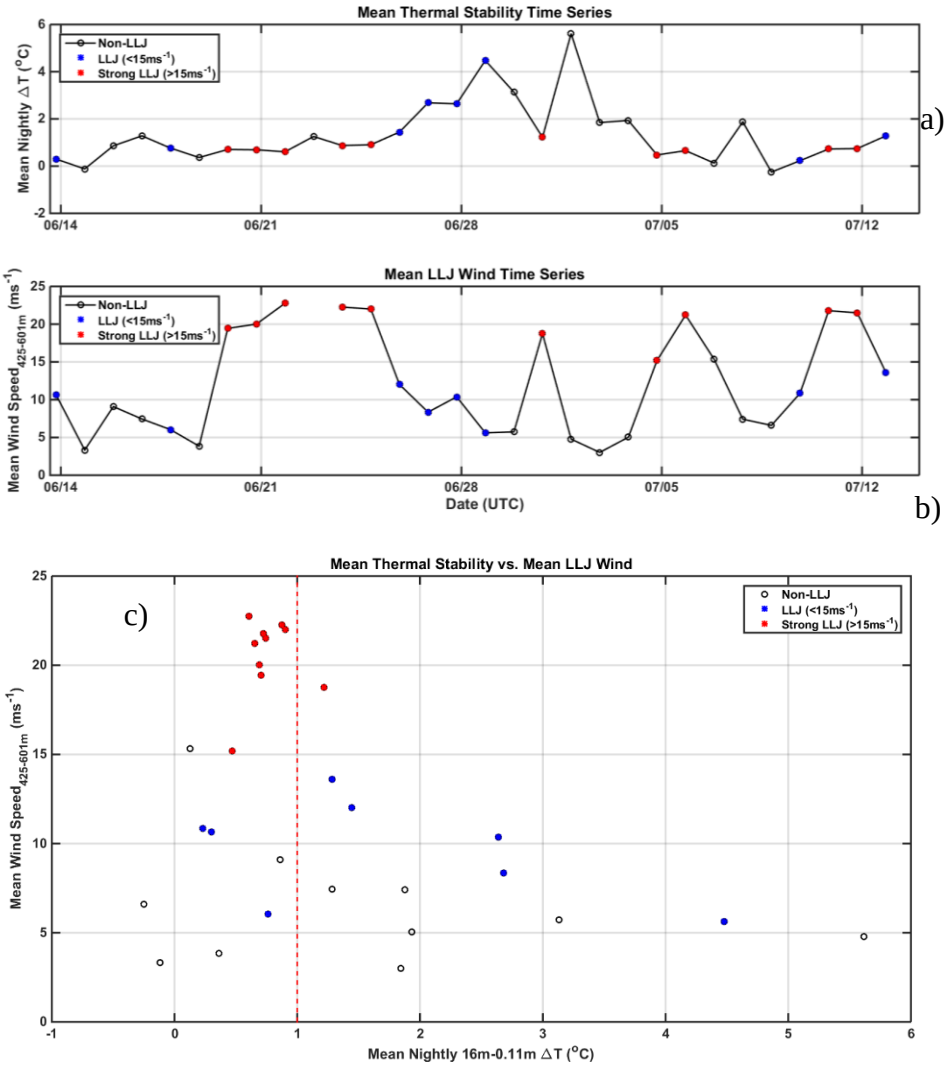

This figure depicts a) temporal variation of mean nightly ΔT, b) temporal variation of the mean nightly wind speed between 425m and 601m, and c) a scatter plot of these same parameters. Red dots signify strong LLJ events (> 15ms^{-1}), blue dots signify weaker LLJ events (<15ms^{-1}), and white dots signify non-LLJ events.

Figure 27. Temporal Variation and Scatter Plot of Mean Nightly ΔT vs. Wind Speed

Figure 27 shows a scatter plot and time series of mean nightly ΔT between 16 m and 0.11 m to illustrate where strong LLJ events, weaker LLJ events, and non-LLJ events resided with respect to surface layer thermal stability. In Figure 27c, the clustering of strong LLJ events can be seen to the left of the vertical 2°C ΔT line. Figure 28 examines the correlation on LLJ days between several quantities representing LLJ and surface layer

wind speed and surface layer thermal stability. Figures 28a and 28b examine the wind speeds at the LLJ nose, 16 m, and 6 m heights with respect to nighttime temperature differences between 16 m and the surface, as well as 2.5 m and the surface, respectively. Figures 28c and 28d display similar information except using the ratios of wind speed including LLJ wind speed to geostrophic wind U_{LLJ}/U_g (LLJ Intensity), LLJ wind speed to 6-m mean wind speed (U_{LLJ}/U_{6m}), and surface layer shear parameter U_{16m}/U_{6m}.

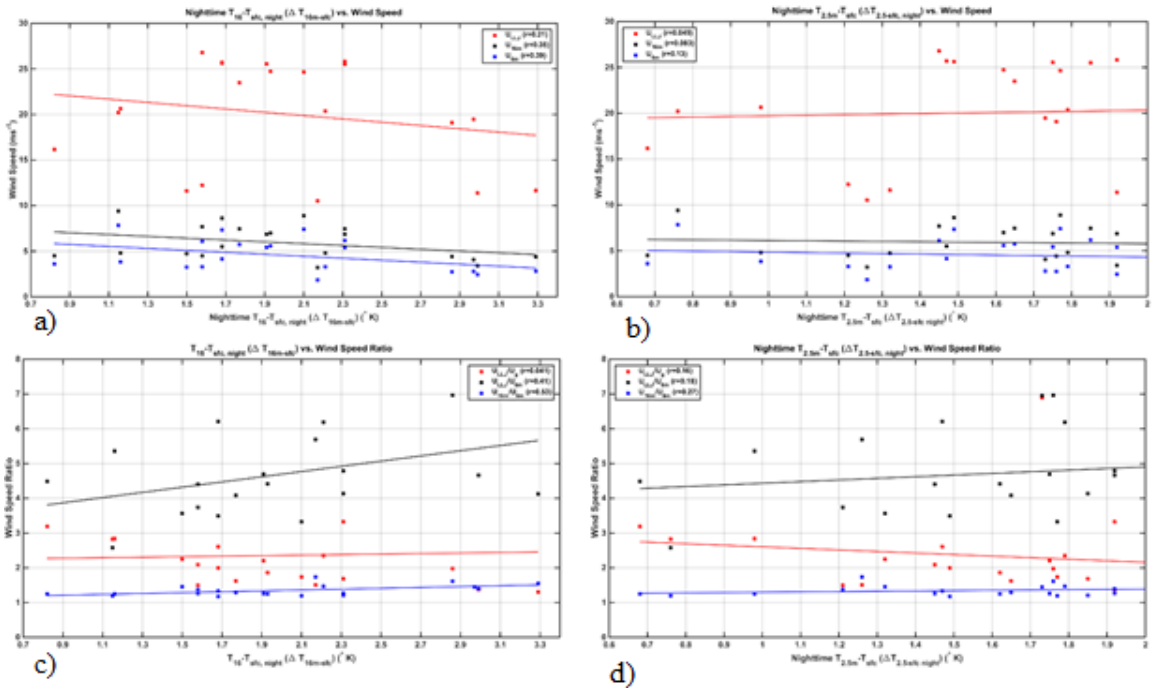

Shown in this figure are an illustration of the correlation between a) the nocturnal 16 m-surface ΔT and the LLJ wind speed, 16-m wind speed, and 6-m wind speed, b) same as in a) except using the temperature difference between 2.5 m and the surface, c) same as in a) except using the wind speed ratios representing LLJ intensity U_{LLJ}/U_g, shear parameter U_{LLJ}/U_{6m}, and surface layer shear parameter U_{16m}/U_{6m}, and d) same as in b) except using the wind speed ratios representing LLJ intensity U_{LLJ}/U_g, shear parameter U_{LLJ}/U_{6m}, and surface layer shear parameter U_{16m}/U_{6m}

Figure 28. Relationship Between Nocturnal Thermal Stability and LLJ Wind Speed Parameters on LLJ Nights

The correlation between nocturnal 16-m and surface temperature difference and LLJ, 16m, and 6m wind speeds (Figure 28a) does not show decisively strong correlation at first glance (0.21, 0.35, and 0.39 respectively), but a trend of decreasing nocturnal 16m-surface inversion with increasing LLJ speed seems to exist. Similar trends are

observed in the 16-m and 6-m mean wind speeds as well. In contrast, the temperature inversion strength between 2.5-m height and the surface do not seem to show any clear correlation (Figure 28b). The strongest correlation when considering the wind speed ratios U_{LLJ}/U_g, U_{LLJ}/U_{6m}, and U_{16m}/U_{6m} is for the 16m-surface ΔT vs. the low-level shear parameter U_{16m}/U_{6m} with a correlation coefficient of 0.53. The spread in data points for each of these plots was discouraging, as the temporal variation plot of nocturnal thermal stability, as well as the scatter plot, showed a meaningful clustering of weak inversion strength with strong LLJ wind speeds. The few low speed LLJ cases in Figures 28a and 28b are natural suspects that reduce the correlation. These data points occurred on 16 June (LLJ speed of 12.2 ms^{-1}), 18 June (LLJ speed of 11.6 ms^{-1}), 27 June (LLJ speed of 11.6 ms^{-1}), 04 July (LLJ speed of 11.4 ms^{-1}), 07 July, and 08 July (LLJ speed of 10.5 ms^{-1}). These LLJ days exhibited relatively lower wind maxima than other LLJ days. Further examinations of these cases reveal significant differences between these weak LLJs and the strong jets. For instance, several of the days (16 June, 18 June, 27 June and 07 July) exhibited earlier than average jet max times. Other days exhibited a lower than average LLJ height of speed maximum (16 June, 18 June, 27 June, and 04 July), or even higher than average LLJ height of speed maximum (08 July). Figure 29 is a collection of higher resolution, single-day views of each LLJ day in question using the HRDL data.

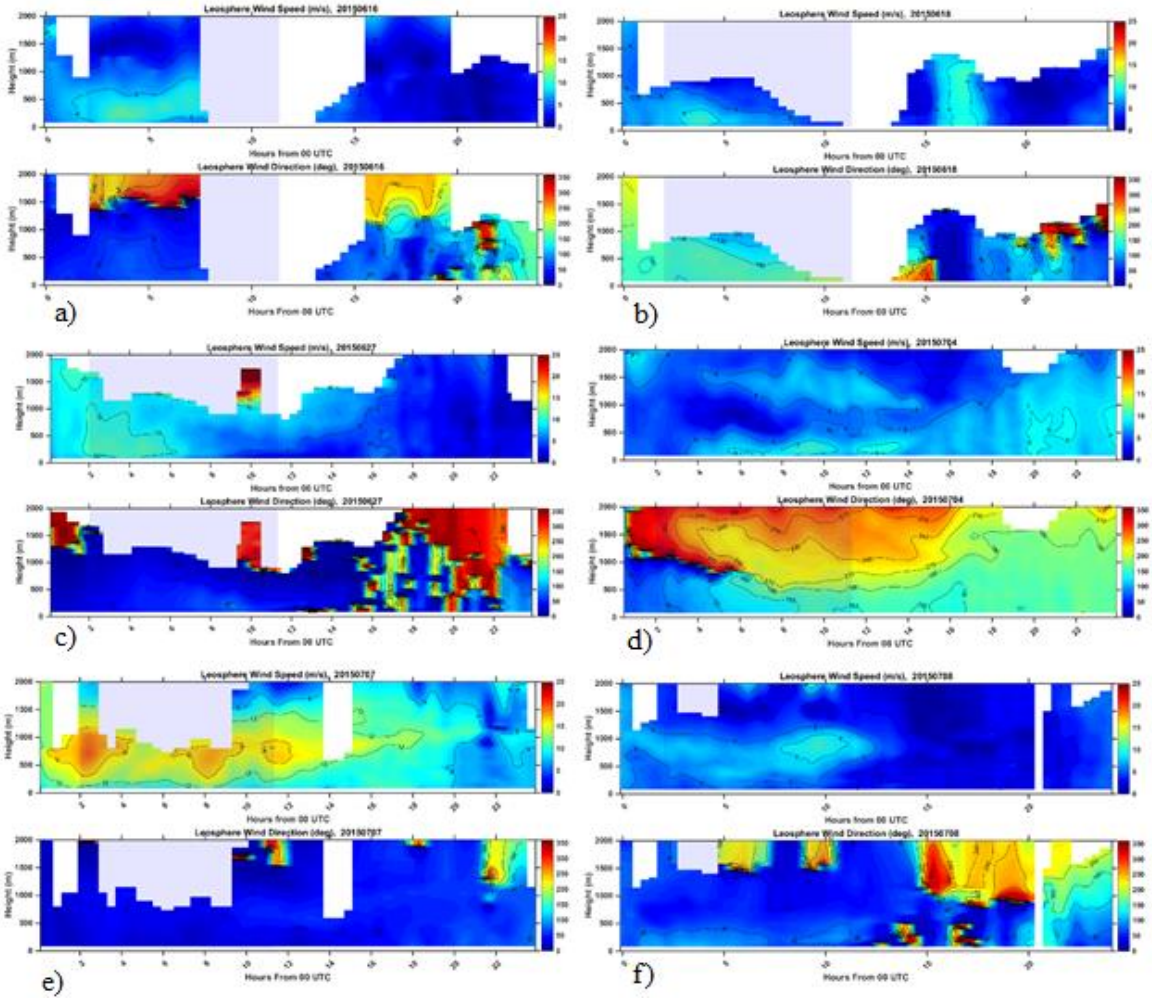

This figure depicts wind speed and direction contour plots as a function of height and time derived from HRDL data for some of the weak LLJ days a) 16 June, b) 18 June, c) 27 June, d) 04 July, e) 07 July, and f) 08 July.

Figure 29. Wind Speed and Direction For Weak LLJ Days

Figure 29 provides insight into why various correlations in Figure 28 may be lower than expected in the observed weak LLJ days. Four days that were determined to be LLJ days per the Andreas (2000) criteria exhibited wind directions that were not characteristic of a traditional Great Plains LLJ, where predominant wind direction is generally from a southerly sector. These days, 16 June (Figure 29a), 27 June (Figure 29c), 07 July (Figure 29e) and 08 July (Figure 29f) exhibited wind speed maxima that fit the Andreas (2000) definition, but had associated wind directions from a generally

northerly or easterly sector. These days will be omitted from further correlation analysis, as low-level wind maxima that do not exhibit wind directions generally from a southerly sector possess properties that are beyond the scope of this thesis. The case on 04 July (Figure 29d) was very interesting, as wind direction was not consistent with that of traditional Great Plains LLJs during the first period of the night, but began rotating anticyclonically several hours after sunset. It would appear that the beginning of this nocturnal period underwent an instability of some sort, and as such, this day will also be omitted. On 18 June (Figure 29b), surface winds originated from a southerly sector, but rotated counterclockwise (cyclonically) with height, as the surface winds are generally from 150° and shift to around 120° at around 500 m. This day will also be omitted from further correlation analysis, as low-level wind maxima that exhibit cyclonically turning wind directions also possess specific properties that are beyond the scope of this thesis. Figure 30 is the same as Figure 28 without the weak LLJ cases.

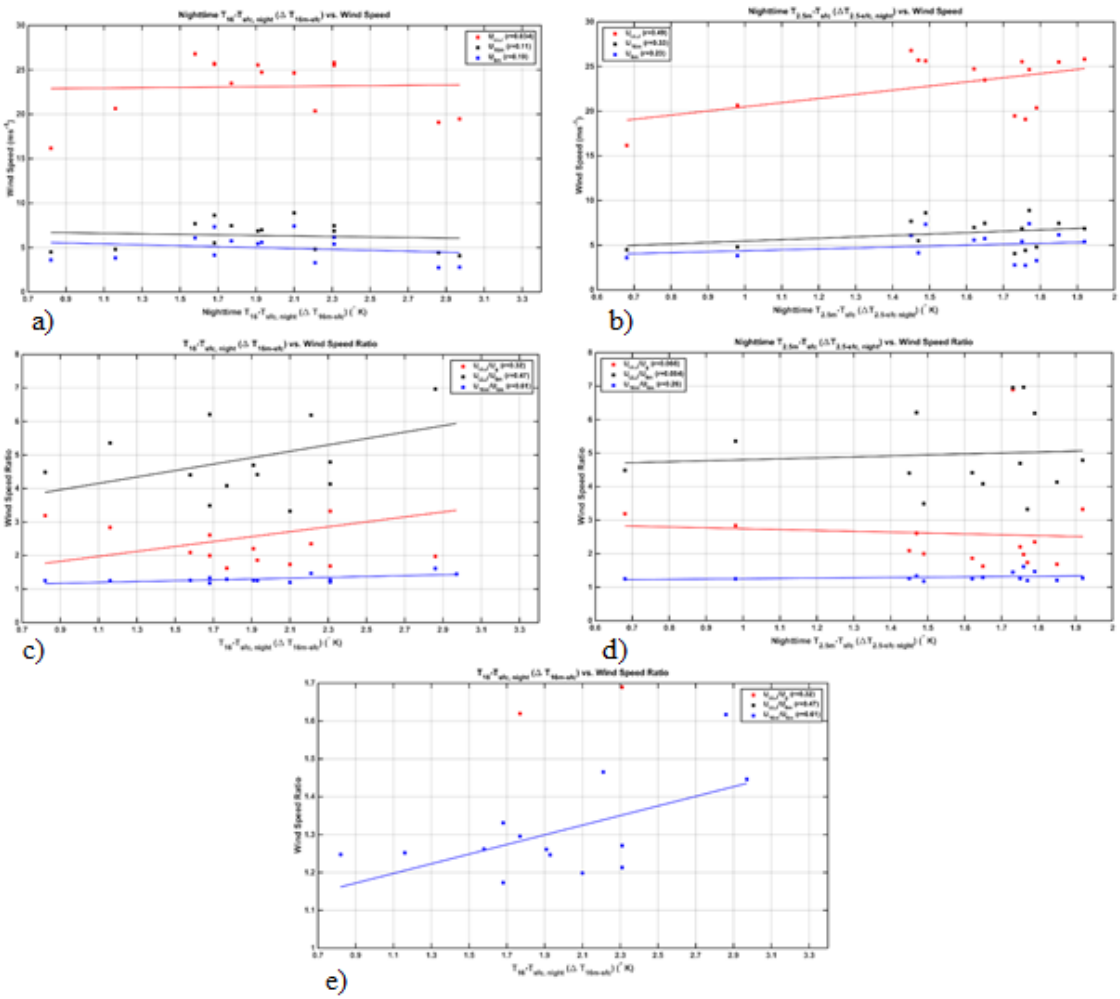

Panels a) to d) in this figure are the same as those in Figure 28 except with the weak LLJ cases removed. In e), a zoomed-in correlation plot is shown, depicting the strong correlation between the nocturnal 16-m and surface temperature difference and surface layer shear parameter U_{16m}/U_{6m}.

Figure 30. Correlation between ΔT and LLJ Wind Speed Properties Without the Weak LLJ Cases

Figure 30 reveals more accurate correlation between surface layer ΔT and LLJ-influenced wind speeds and ratios. With the weak LLJ cases, there was no appreciable trend for U_{LLJ} vs. the 16m-surface ΔT and the new correlation coefficient for the same comparison decreased even lower to 0.03. Figure 28b also revealed that, albeit a low correlation, 2.5 m-surface ΔT increased for decreasing LLJ wind speed. Without the weak LLJ cases, Figure 30b reveals that, with a correlation coefficient of 0.49, 2.5 m-surface ΔT actually increases for increasing LLJ wind speed. This enhanced correlation is likely

results from the two data points with ΔT ~1.0 and ΔT ~0.7 for 05 July and 10 July, respectively. Upon examination of the HRDL data for these days, there were no extraneous wind speed/direction properties that rendered them expendable. While these days will not be omitted, it is important to keep in mind that the rest of the data points themselves do not present a similar trend when using the entire dataset as shown currently on Figure 30b. While the time series plot in Figure 26 generally agrees with the findings in Shapiro (2009) that weaker capping inversions tend to favor larger ageostrophic wind maxima, namely the Great Plains LLJ, the findings in the Shapiro study may not accurately account for the very near surface environment. LLJ wind maxima in the Shapiro (2009) study tend to become supergeostrophic by the stated 70% or more for capping inversion heights of 1000 m or more, a height which was beyond the capabilities of the instrumentation at FP-2, and subsequently, beyond the scope of this study with a surface layer focus. Additionally, the shear parameters U_{LLJ}/U_{6m} and U_{16m}/U_{6m} revealed relatively high correlation with the 16 m-surface ΔT (Figures 30c, e) with coefficients of 0.47 and 0.61, respectively. Increasing shear between U_{LLJ} and U_{16m} and U_{16m} and U_{6m} tended to result from the increasing stable thermal stratification between 16 m height and the surface. This is also consistent with the previous physical explanation that increased mixing which results from the enhanced shear-driven turbulence between the LLJ nose and surface, transports warmer air aloft to the surface layer. The same relationship did not seem to hold for the 2.5 m-surface ΔT, as correlation coefficients with the bottom right plot are quite low.

3. Dynamic Stability

The bulk Richardson number is a measure of boundary layer stability and is intended to identify whether buoyancy (numerator) or wind shear (denominator) contribute more substantially to turbulence generation/consumption. When Ri_B is greater than 1, it can be assumed that the positive temperature difference between two levels (i.e., negative buoyancy) dominates wind shear in generating/consuming turbulence. When Ri_B is less than 1 but greater than 0, it can be deduced that the wind shear generated turbulence dominates turbulence consumed by buoyancy, resulting in overall turbulent flow. A bulk Richardson number less than 0 but greater than -1 signifies an unstable

regime dominated by vertical shear of the mean wind. A negative bulk Richardson number less than -1 also signifies an unstable regime, but one that is dominated by buoyancy plumes. For PECAN measurements at FP-2, bulk Richardson number were found to vary greatly. The following quantitative discussions of the Richardson number neglect the cases of free convection defined by cases where $Ri_B < -2$ and near-laminar flow where $Ri_B > 2$. These two types of extreme stability cases did not occur too often, but when they did, the extreme Richardson number changed the general statistics substantially. The magnitude of the Richardson number was not especially meaningful in these two extreme regimes. As a result, the extreme stability cases were removed in the analysis. Figure 31 is a plot of temporal variation of bulk Richardson number and mean wind speed between 425m and 601m for the entire duration of the project.

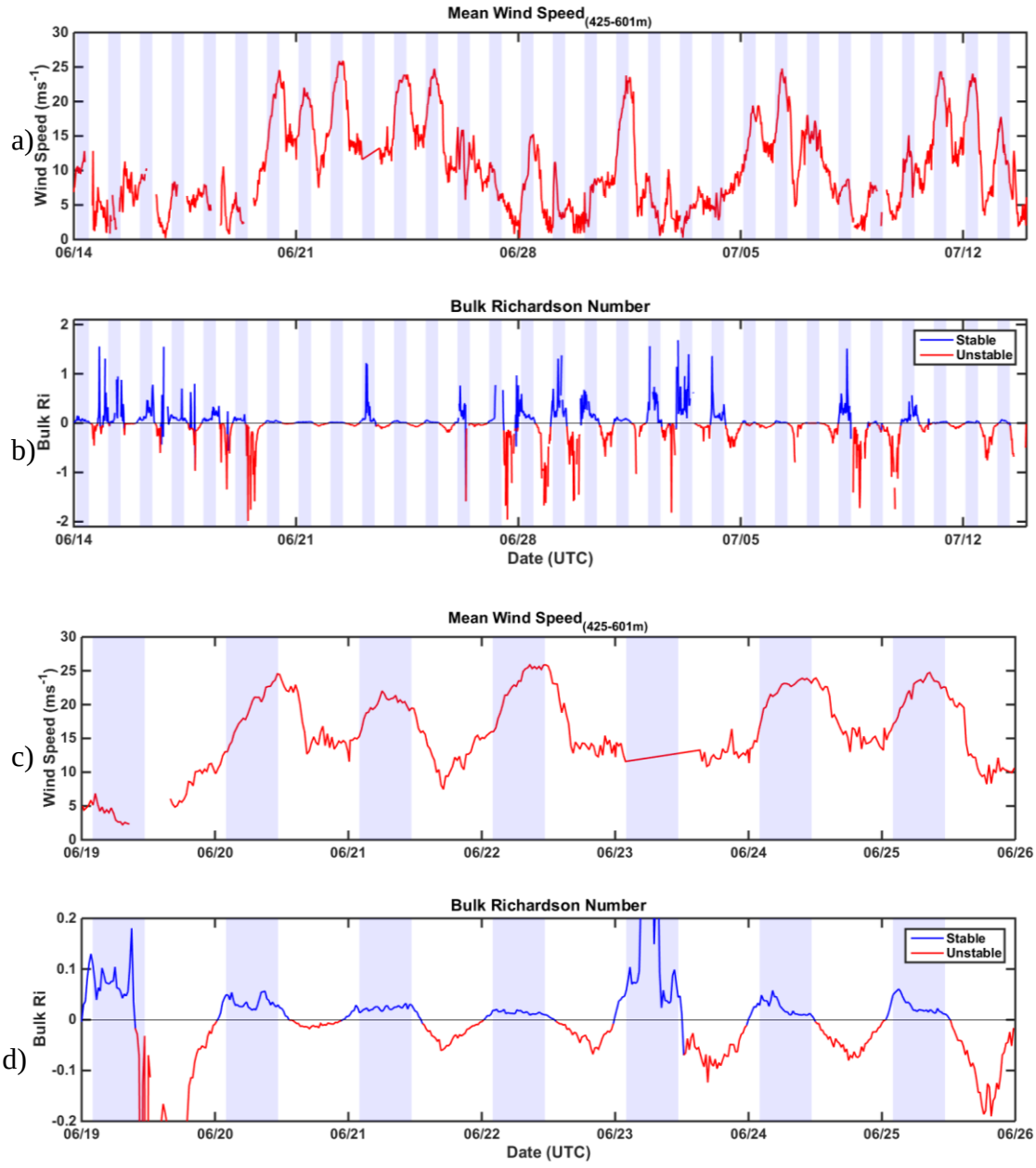

Shown in this figure are a) the full period temporal variation of 425 m-601 m mean wind speed b) bulk Richardson number, c) same as a) except for 19–26 June 2015, and d) same as a) except for 19–26 June 2015. Richardson number calculation used measurements from the lowest 10 m of the surface layer and was calculated using a combination of data from the 16-m flux tower and the 3-m scalar tripod. Blue portion of the time series signifies positive Richardson number, while the red portion signifies negative, unstable Richardson number. Purple shading signifies the time period between sunset and sunrise.

Figure 31. Temporal Variation of Mean Winds between 425 m and 601 m and Bulk Richardson Number

Diurnal variation in Richardson number is shown well in Figure 31. During the daytime CBL when large amounts of turbulence are generated by a combination of positive buoyancy and wind shear, the Ri_B is negative, signifying instability. After the afternoon-to-evening boundary layer transition, the surface layer vertical gradient of temperature becomes positive once an inversion forms, resulting in negative buoyancy. This yields positive *Ri* values that manifest themselves as positive spikes in Figure 31a. One interesting feature is the weaker positive stability under LLJ influence, represented by the only marginally positive *Ri* values in Figure 31d. These marginally positive *Ri* values are present during days with stronger mean wind speeds between 425 m and 601 m, including 20–22 June, 24–25 June, 01 July, 05–07 July, and 11–13 July. Nights where no LLJ occurs or where LLJ presence may be more difficult to determine contain *Ri* values that are larger in magnitude, signifying stronger stable nocturnal stratification. Figure 32 is a scatter plot of the mean bulk Richardson number between sunset and sunrise for the entire period plotted against the average nightly mean wind speed between 425 m and 601 m.

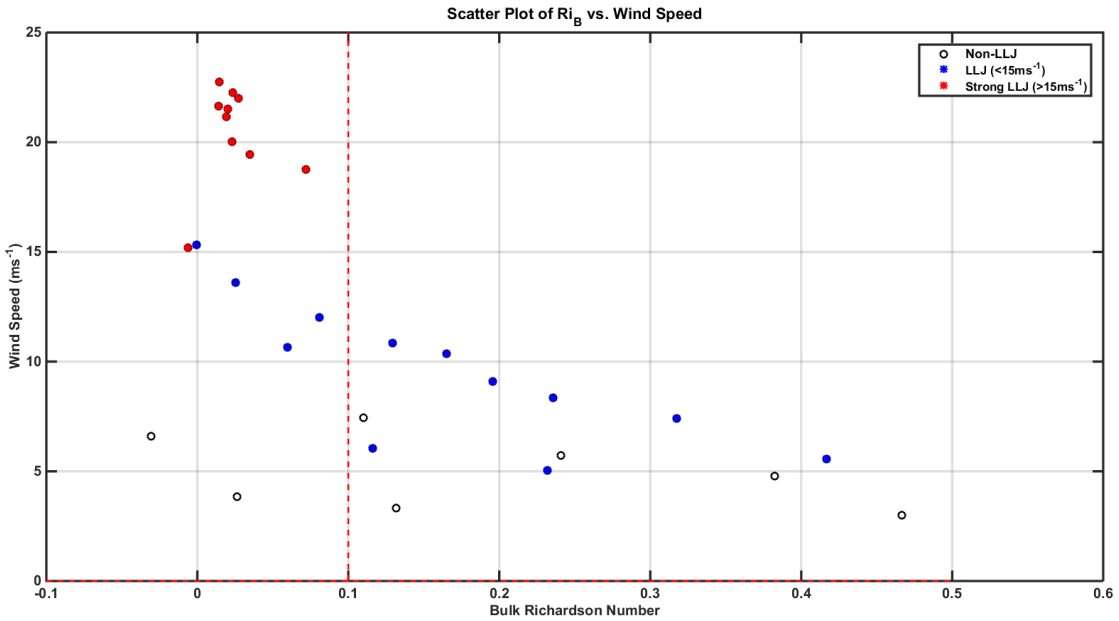

Open circles indicate non-LLJ events, blue dots indicate weak LLJ events with wind speed < 15 ms^{-1}, and red dots indicate strong LLJ events with wind speed >15 ms^{-1}). The vertical red dashed line is set at Ri_B=*0.1*. All strong LLJ events are to the left of this line (R_{iB} <0.1).

Figure 32. Scatter Plot of Mean Nightly Ri_B vs. Mean Nightly Wind Speed for Entire Period

Figure 32 emphasizes the previous suggestion that stronger LLJ wind speeds are associated with relatively weaker positive stability throughout the night. The red dots in Figure 32, which represent strong LLJ nights, are confined to the left of the Ri_B=0.1 line. This subsequently leads to the definitive conclusion that strong LLJ nights are associated with weak surface stability (i.e., close to neutral stability) throughout the night on LLJ days, and may not exceed Ri_B values of 0.1. The same conclusion cannot be drawn for weaker LLJ events, as the spread of data points among all positive, stable values of Ri_B is too wide. Weaker LLJ events with mean nightly wind speeds ranging between 5 ms^{-1} and 15 ms^{-1} yielded Richardson number values ranging from near neutral (Ri_B=0) to 0.4. A clear relationship for these weak events cannot be determined. Figure 33 contains correlation plots of nighttime Ri_B against several LLJ-influenced wind speeds, LLJ intensities, and wind shear parameters, as was depicted with thermal stability in Figure 30.

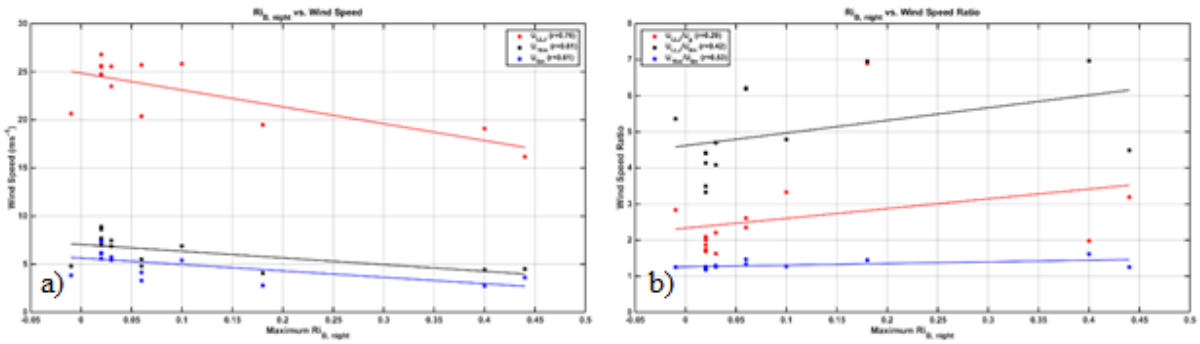

Shown in this figure are a) the correlation between nighttime Ri_B and LLJ wind speed, 16-m wind speed, and 6-m wind speed, and b) the correlation between nighttime Ri_B and LLJ intensity U_{LLJ}/U_g and wind shear parameters U_{LLJ}/U_{6m} and U_{16m}/U_{6m}.

Figure 33. Relationship between Nocturnal Dynamic Stability and LLJ Wind Speed Parameters on LLJ Nights

In Figure 33 and for all additional correlation points, the weak LLJ nights have not been included, which results in increased correlation coefficients for several parameters. In examining Figure 33a, the correlation coefficient for Ri_B vs. U_{LLJ} increased from 0.70 to 0.76 with a trend for smaller values of positive Ri_B with stronger LLJ wind speeds, which is consistent with the data in Figures 31 and 32. Correlation coefficients did rise for Ri_B vs. the 16-m and 6-m mean wind speeds (0.56 each, updated to 0.61), signifying that stronger LLJ wind speeds translated to subsequently stronger 16-m and 6-m wind speeds in the surface layer, and that these stronger low-level winds also contributed to lower values of nocturnal Ri_B, or weak stability in the surface layer. As mentioned previously, positive values of Ri_B that are less than 1 represent wind shear in the surface layer dominating buoyancy in determining the dynamic stability.

Correlation between LLJ intensity and the shear parameters U_{LLJ}/U_{6m} and U_{16m}/U_{6m} and nocturnal Ri_B is not as straightforward. The ratio of U_{16m}/U_{6m}, used as a proxy for surface layer wind shear, has the highest correlation to nocturnal Ri_B with a coefficient of 0.53 with the weak LLJ cases omitted. Ri_B values increase slightly for increasing U_{16m}/U_{6m}. This relationship highlights thermal stability effects on wind shear in the surface layer. Under stable conditions, thermal stability effects tend to increase wind shear, which is consistent with the Monin-Obukhov Similarity Theory. Stronger thermal stability tends to suppress vertical turbulent mixing, resulting in enhanced

horizontal wind shear, which is reinforced in Figure 33b. While the correlation between LLJ intensity U_{LLJ}/U_g and Ri_B is quite low, a general trend of increasing nocturnal Ri_B for increasing LLJ intensity can be seen. For LLJ intensity to increase, this would require either U_{LLJ} to increase significantly or the background synoptic flow U_g to decrease. Previously, this analysis has shown that increasing U_{LLJ} tends to result in decreasing Ri_B values, signifying a weakly stable regime. The depiction of rising Ri_B values for rising U_{LLJ}/U_g seems counterintuitive for what might be expected. This has warranted a closer look at the relationship between the *ad hoc* proxy for geostrophic wind and absolute LLJ wind maxima. Figure 34 shows this relationship.

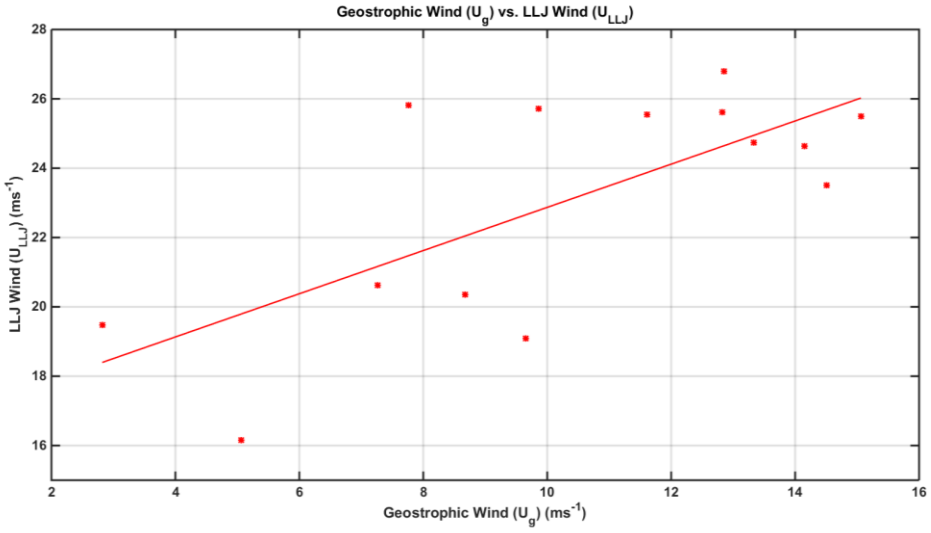

All data points are for LLJ nights only, with weak LLJ cases removed. See text for the definition of geostrophic wind.

Figure 34. Relationship between Geostrophic and LLJ Winds

The correlation coefficient of the geostrophic wind speed plotted against LLJ wind speed is 0.70, meaning that, for this dataset, the proxy for geostrophic wind speed, as was defined in Klein (2015), is strongly correlated to the LLJ wind speed. This raises the possibility that the sampling of geostrophic wind values as calculated for this analysis may actually be vertically embedded in the LLJ itself. Recall that these *ad hoc* geostrophic wind values were calculated as the mean wind speed above 800 m AGL between 1700 UTC (1200 Local Time) and sunset. Since the Leosphere HRDL was only

able to retrieve horizontal wind values to a ceiling of about 1500 m, the current calculation of geostrophic wind may be lacking in the ability to retrieve true geostrophic-like values higher in the atmosphere. The current analysis of geostrophic wind may be over-representing the true value of geostrophic wind, and as such, values of geostrophic wind presented may actually be part of the vertical extent of the LLJ. For the remainder of this analysis, LLJ winds scaled by the geostrophic wind as a proxy for LLJ intensity will also be omitted. The shear parameters U_{LLJ}/U_{6m} and U_{16m}/U_{6m} will continue to be analyzed against other boundary layer parameters.

4. Moisture

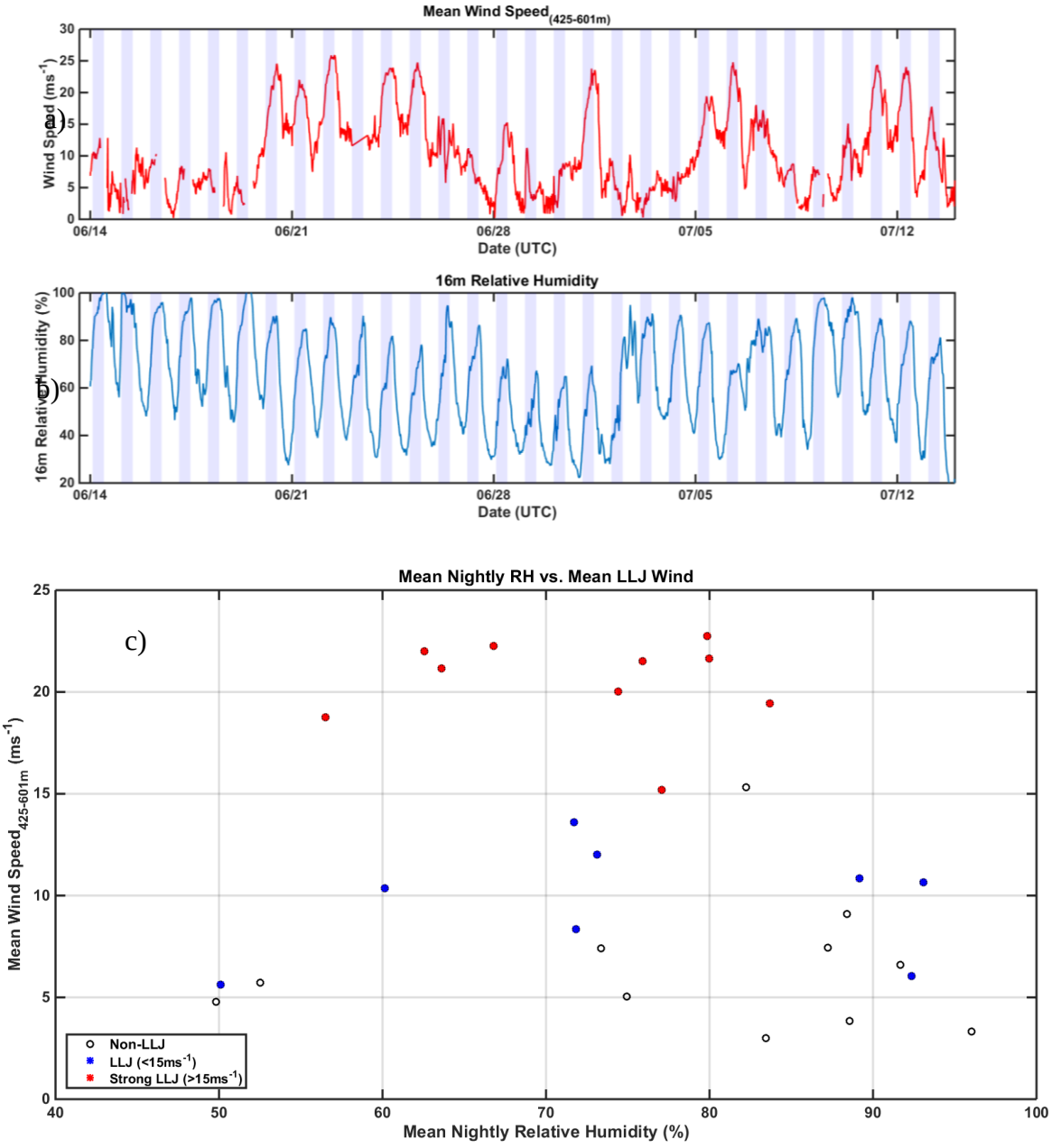

This figure depicts a) a temporal variation of both the 425m-601m mean wind speed and 16m relative humidity where purple shading signifies the time period between sunset and sunrise and b) a scatter plot of 16m relative humidity plotted against 425m-601m mean wind where red points represent strong LLJ events (>15ms^{-1}), blue points represent weaker LLJ events (<15ms^{-1}), and white dots represent non-LLJ events.

Figure 35. Relationship between Relative Humidity and LLJ Wind

The relationship between LLJ and surface layer moisture was also examined in this analysis. Figure 35 is a depiction of this relationship. Here, the temporal variation of 16-m relative humidity and 425 m-601 m wind speed reveals that nights under the influence of a LLJ appear to have lower maximum relative humidity values during the nocturnal period. Following the expected diurnal trend, relative humidity increases during the nocturnal period and drops upon the onset of the daytime CBL. For stronger LLJ nights such as 20–22 June, 24–25 June, 28 June, 01 July, 07 July, and 11–12 July, the maximum nocturnal relative humidity stays below 90% and even remains as low as 65% on 01 July. These findings are further reinforced with the scatter plot in Figure 35 where each red dot signifying strong LLJ events remain below 90% saturation while several weaker LLJ nights and non-LLJ nights attain greater than 90% saturation. The lower relative humidity values associated with stronger LLJs can be attributed to warmer air aloft being transferred to the surface via LLJ-generated mixing at night. These warmer temperatures at the surface inhibit saturation that occurs when the surface cools towards the dew point temperature near the surface, which is a typical occurrence under non-LLJ conditions.

D. SURFACE FLUX AND TURBULENCE RESPONSE UNDER LLJ INFLUENCE

1. Surface Fluxes

The NPS team made high-rate turbulence measurements at four levels on the 16-m flux tower throughout the PECAN campaign. Specifically, momentum flux, sensible heat flux, and latent heat flux were investigated for the entire experiment period, and particularly on LLJ nights. Figures 36 and 37 are plots of temporal variation of LLJ winds and all three fluxes.

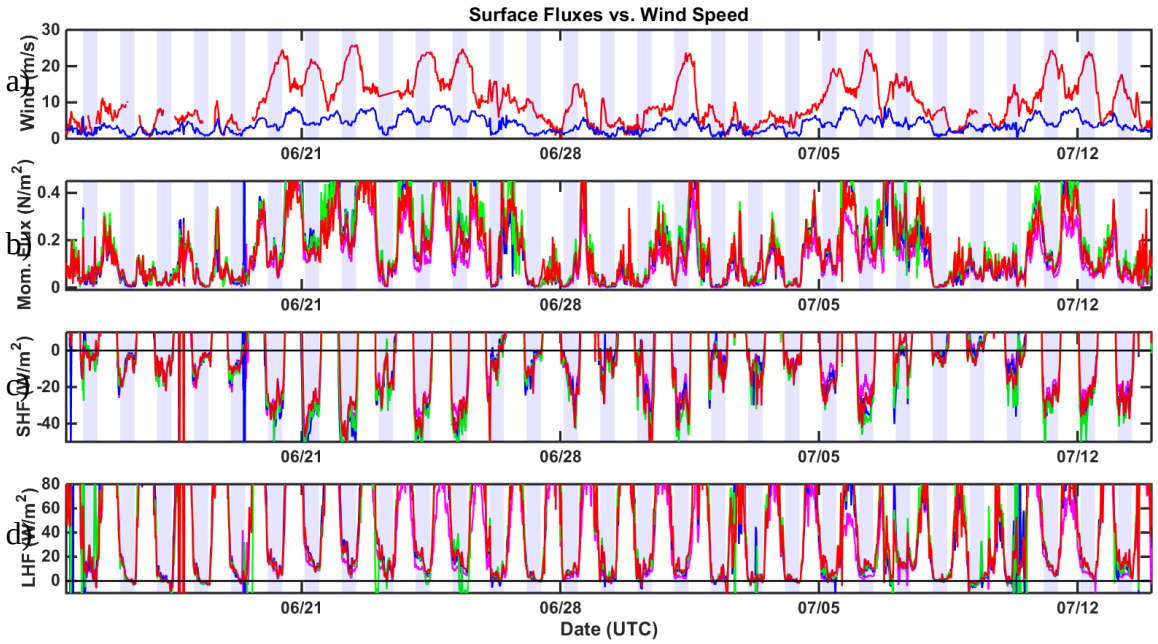

This figure represents a) the mean winds between 425 m-601 m (red) and at 2.5-m AGL (blue), b) momentum flux at 2.5 m (magenta), 5.6 m (blue), 11.3 m (green), and 16 m (red), c) sensible heat flux at the same levels (colors) as momentum flux and d) latent heat flux at the same levels (colors) as momentum flux. Purple shading signifies the time period between sunset and sunrise.

Figure 36. Temporal Variation of Mean Wind Speeds and Surface Fluxes

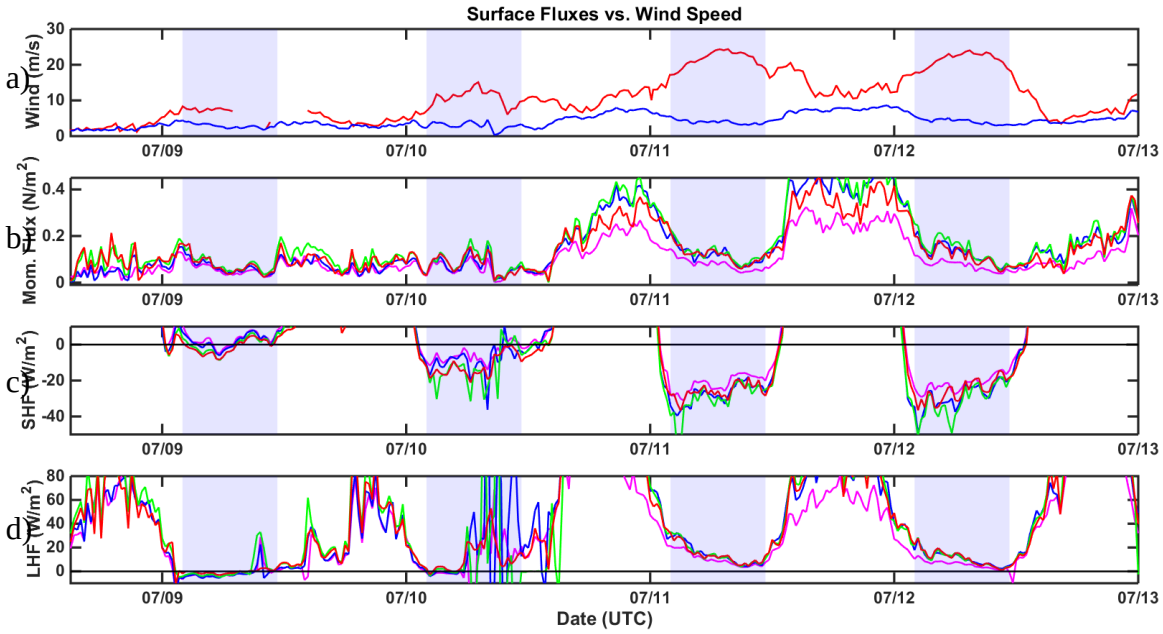

See Figure 36 caption for height levels and associated colors. This temporal variation is zoomed to a shorter time period for 09–13 July.

Figure 37. Temporal Variation of Mean Wind Speeds and Surface Fluxes, 09–13 July Time Period

Figure 36 depicts the variation in momentum flux, sensible heat flux, and latent heat flux throughout the period. Diurnal variations in each flux are shown. As expected, momentum flux increases drastically during the daytime CBL regime and decreases around sunset to a constant value throughout the NBL regime. Sensible and latent heat flux follow suit, increasing to a peak value in the middle of the daytime, and decreasing to a constant value through the nocturnal period. Several interesting features are manifested for LLJ events, which can be seen in the contrast between the non-LLJ night 09 July, and the subsequent several LLJ nights on 12–13 July, as can be seen well in Figures37a-d. While all values of momentum flux remain at a nearly constant, decreased value throughout the nocturnal period, nights under LLJ influence show a slightly higher minimum value between sunset and sunrise. LLJ wind speed maxima generate enhanced mechanical turbulence below the jet nose, resulting in a subsequently enhanced value of momentum flux throughout the night. The temporal variation of sensible heat flux in Figure 36c and Figure 37c depicts a larger magnitude of downward-pointing sensible heat

flux on stronger LLJ days. This also is due to an enhancement of the mechanical turbulence beneath the LLJ nose. Wind shear generated by the LLJ increases turbulent mixing within the surface layer and thereby transports sensible heat to the surface from aloft. Finally, the magnitude of latent heat flux under LLJ influence was also observed to be enhanced. During LLJ events, the surface layer was characterized by increased latent heat flux, transporting moisture from the surface to the atmosphere via turbulent vertical mixing. Figure 37 is a scatter plot of the mean momentum flux, mean sensible heat flux, and mean latent heat flux at the four levels of the 16-m flux tower over the experiment period.

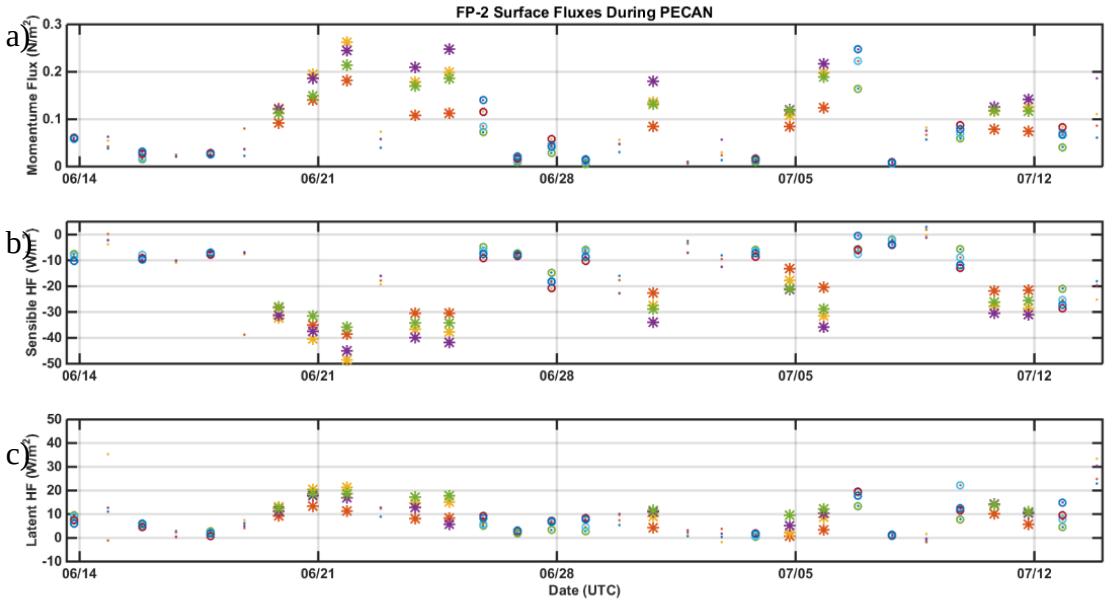

This figure depicts a) the mean momentum flux during the nocturnal period for each day of the campaign at the four levels of the 16m flux tower, b) the mean sensible heat flux at the same four levels of the 16-m flux tower, and c) the mean latent heat flux also for the same levels of the 16-m flux tower. Strong LLJ nights (>15ms^{-1}) are marked with a "*," weaker LLJ nights (<15ms^{-1}) are marked with an "o," and non-LLJ nights are marked with a .."“

Figure 38. Mean Surface Fluxes From Measurements on the 16-m Flux Tower

Mean surface flux values in Figure 38 confirm the enhancement of turbulent transport of momentum, sensible heat, and latent heat described previously. Strong LLJ

nights have a larger magnitude of momentum flux than all non-LLJ days and all weaker LLJ days with one exception on 07 July. This underscores that shear-generated mechanical turbulence enhances surface friction under LLJ influence. Similarly, the magnitude of sensible heat flux is also enhanced under strong-LLJ presence such that sensible heat is transported to the surface from aloft via shear-generated turbulence at night. The relationship between sensible heat flux and weaker LLJ nights and non-LLJ nights is not as straightforward, as there are some weaker LLJ nights (e.g. 28 June) that have an equal mean sensible heat flux magnitude as non-LLJ nights (e.g. 30 June). On non-LLJ nights, turbulence is reduced, resulting in subdued vertical mixing and a reduction in the downward transport of sensible heat. In fact, 09 July, which was a non-LLJ night, yielded a positive value of mean sensible heat flux, resulting in an upward transfer of sensible heat to the atmosphere. Finally, a slight enhancement of the mean latent heat flux magnitudes also occurred on strong LLJ night, albeit not nearly as discernible as for the sensible hear flux and momentum flux. In general, strong LLJ nights had a larger magnitude than non-LLJ days, but were in some cases (e.g. 22 June) equal in magnitude to weaker LLJ days (e.g. 07 July). Some non-LLJ days ultimately resulted in a negative mean latent heat flux, meaning latent heat was transported downward to the surface in small quantities, owing to the absence of turbulence-generated mixing. Figure 39 is a scatter plot of mean surface flux quantities plotted against mean 425 m-601 m wind speed and further emphasizes the previous conclusion that surface flux quantities are enhanced under strong LLJ influence as compared to their weaker LLJ and non-LLJ counterparts.

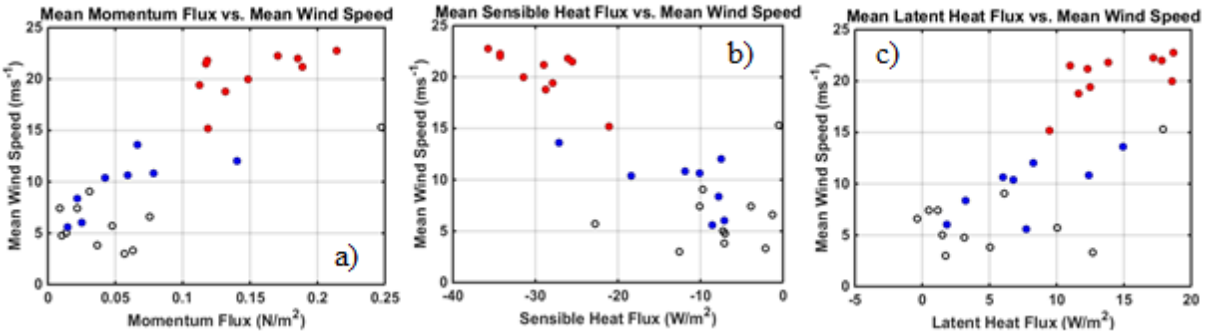

Pictured are scatter plots of a) momentum flux, b) sensible heat flux, and c) latent heat flux plotted against the mean 425 m-601 m wind speed. Red dots represent strong LLJ events (>15ms^{-1}), blue dots represent weaker LLJ events (<15ms^{-1}), and white dots represent non-LLJ events.

Figure 39. Scatter Plot of Surface Fluxes Plotted Against Mean Wind Speed

2. Turbulence

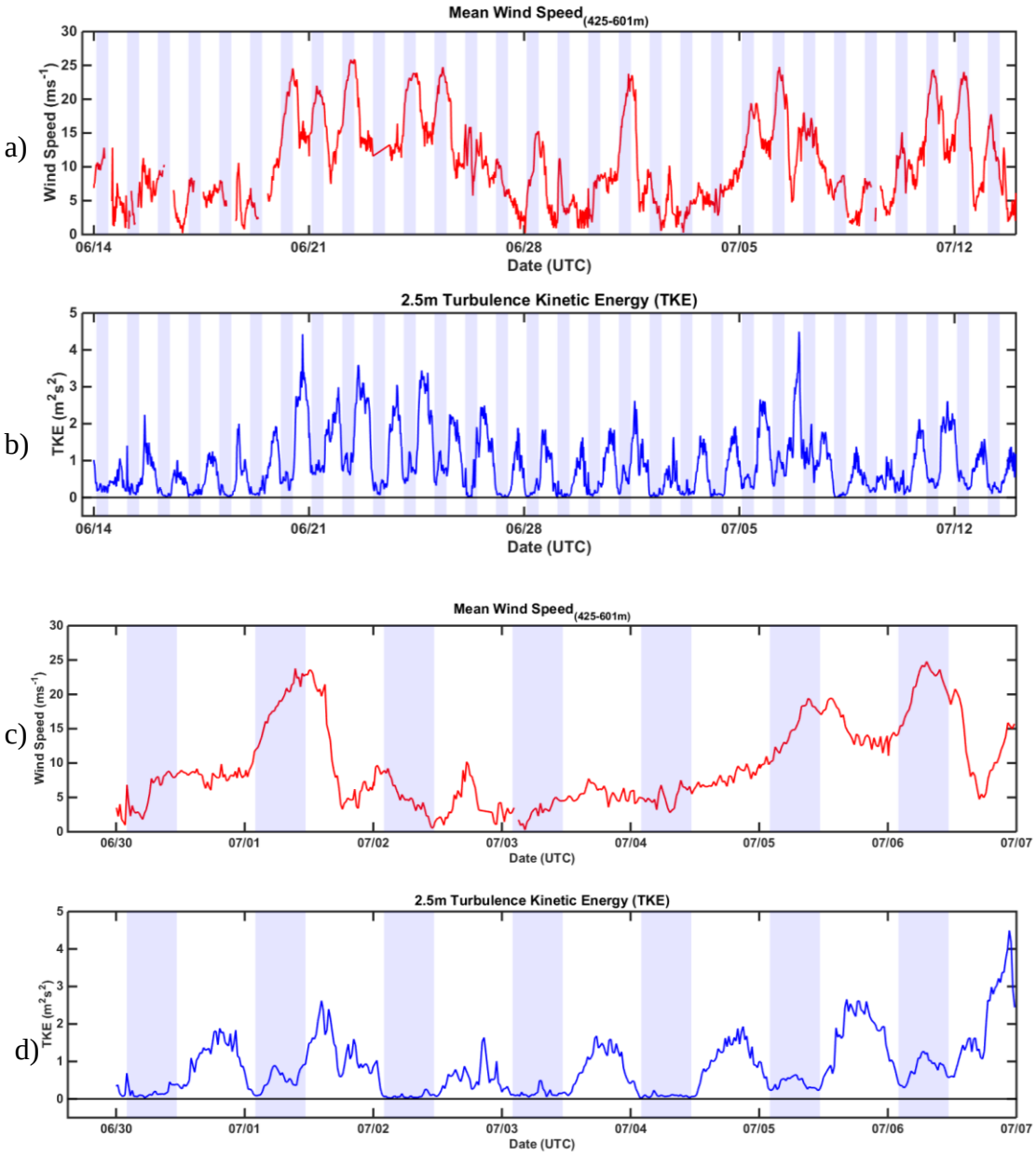

Shown here is the full-period temporal variation of a) the 425 m-601 m mean wind (red) and b) 2.5 m level TKE (blue). Also shown is a temporal variation for the period of 30 June-07 July for c) the 425 m-601 m mean wind (red) and d) 2.5 m TKE (blue). Purple shading indicates the time period between sunset and sunrise.

Figure 40. Temporal Variation of TKE at 2.5 m Level and Mean Wind Speed

Understanding of LLJ-influenced surface fluxes of momentum, sensible heat, and latent heat may be better achieved in examining TKE observations at FP-2 during PECAN. Figure 40 depicts the temporal variation of TKE at 2.5m over the course of the project. Diurnal variation in TKE can be seen in this figure, where values of TKE increase drastically during the daytime CBL and decrease to a near-constant value during the overnight hours each night. This observation is consistent with expectations, as large amounts of turbulence are generated during the day when positive buoyancy (i.e., convection) and large values of wind shear promote strong vertical mixing. Conversely, when negative buoyancy sets in and wind shear subsides, turbulence within the boundary layer subsides to a nearly constant value overnight relative to the daytime regime, supported only by wind shear. Closer examination of the plots of temporal variation in Figure 40c-d reveal that nocturnal values of TKE are affected in the presence of a wind speed maxima in the upper boundary layer. While many of the TKE values in the zoomed in time series remain near zero for weak LLJ days and non-LLJ days (02-03 July), stronger LLJ days tend to enhance the magnitude of TKE during the nocturnal period. Measurements on 01 July and 06 July are perfect examples of this response. Large TKE values from a daytime regime dominated by positive buoyancy and wind shear subsides around sunset, but begins to increase again just after sunset as the LLJ begins to form and shear-driven turbulence begins. The commencement of LLJ formation coincides almost exactly with the time of TKE minimum, making a strong case for an inertial oscillation-dominated LLJ where surface frictional effects are initially at a minimum. For the 01 July and 06 July cases, values of TKE undergo a second phase of decrease approximately half-way through the nocturnal period, but begin increasing again during the early morning hours near the time of sunset, and subsequently at the same time as LLJ decay. Figure 41 is a scatter plot of mean nightly TKE plotted against the 425 m-601 m mean wind speed and will emphasize the correlation between larger nocturnal TKE and strong LLJ events.

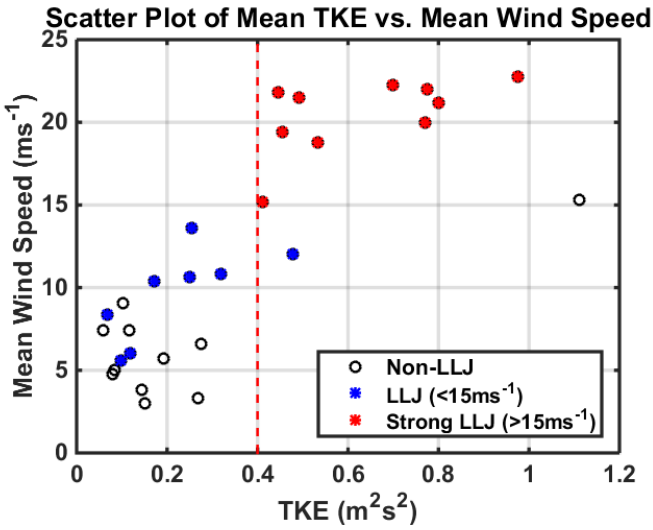

Red points represent strong LLJ events (>15ms^{-1}), blue points represent weak LLJ events (<15ms^{-1}), and white dots represent non-LLJ events. The red dotted line at TKE=0.4 is a lower threshold for TKE values associated with strong LLJ events.

Figure 41. Scatter Plot of Mean 2.5m TKE and Mean Wind Speed

Mean TKE correlation with mean 425 m-601 m wind speed is strong, as can be seen in Figure 41. TKE=0.4 represents a lower bound for higher TKE values associated with strong LLJ events, as every strong LLJ event surpassed this value for TKE. Consequently, all non-LLJ events and almost every weaker LLJ event fell below this threshold, with the exception of one weaker LLJ event and a non-LLJ night. This highlights the fact that surface layer turbulence is heavily influenced by strong LLJ presence and tends to be reasonably enhanced by LLJ-generated wind shear. This also provides additional credence to the discussion on enhanced surface fluxes, where higher than normal amounts of turbulence under strong LLJ presence supports increased vertical mixing, allowing quantities of momentum, sensible heat, and latent heat to be transported more efficiently.

Correlation analysis was also conducted on the turbulence parameter U_t, whose definition can be found in Equation (13), which was previously defined in Klein (2015) and whose value, when squared, is equivalent to TKE. This correlation is depicted in Figure 42 and has omitted both the anomalous Andreas (2000)-defined wind speed maxima days discussed previously and correlation with U_{LLJ}/U_g.

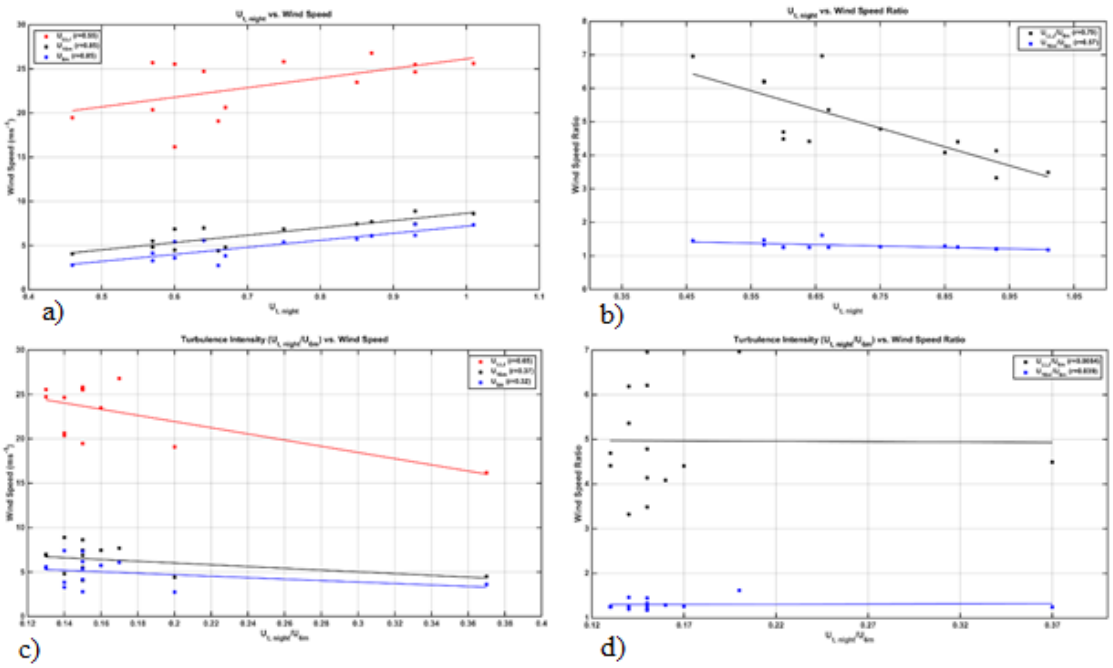

This figure depicts correlations between a) nighttime turbulence U_t, and LLJ wind speed, 16-m wind speed, and 6-m wind speed, b) nighttime turbulence U_t and wind shear parameters U_{LLJ}/U_{6m} and U_{16m}/U_{6m}, c) turbulence intensity U_t/U_{6m} and LLJ wind speed, 16-m wind speed, and 6-m wind speed, and d) nighttime turbulence intensity U_t/U_{6m} and wind shear parameters U_{LLJ}/U_{6m} and U_{16m}/U_{6m}. These plots have excluded weak LLJ cases from 16 June, 18 June, 27 June, 04 July, 07 July, and 08 July. All points are for LLJ days only.

Figure 42. Relationship between Nocturnal Turbulence and Wind Speed Parameters

Nocturnal turbulence parameter U_t correlates well with the mean U_{LLJ}, U_{16m}, and U_{6m} with correlation coefficients of 0.55, 0.85, and 0.85, respectively. This agrees with expectations that, with increasing LLJ wind speeds, surface layer wind speeds also increase, causing enhanced turbulence at the surface. The turbulence intensity parameter U_t/U_{6m} also correlates well with the LLJ wind speed U_{LLJ} with a correlation coefficient of 0.65. As LLJ wind speeds increase, the turbulence intensity tends to decrease. While the turbulence U_t by itself increases as LLJ wind speed (and correspondingly U_{16m} and U_{6m}) increases, the turbulence intensity decreases, as is expected. The U_{6m} in the denominator of turbulence intensity U_t/U_{6m} may be considered similar to the shear term in the denominator of Ri_B. As LLJ wind speeds increase, the wind speeds at heights below the jet nose also increase, including within the surface layer with U_{6m}. While turbulence does

increase for increasing LLJ wind speeds (as is shown in Figure 41a), the magnitude of turbulence increase is smaller than the magnitude of the wind shear proxy U_{6m} increase in the denominator, thereby reducing the value of turbulence intensity for stronger U_{LLJ}.

In Figure 41b, strong correlations exist for turbulence parameter U_t when plotted against both U_{LLJ}/U_{6m} and U_{16m}/U_{6m}, with coefficients of 0.79 and 0.57, respectively. For a decreasing ratio of U_{LLJ}/U_{6m}, turbulence actually increases. Because shear-driven turbulence is a localized phenomenon, this result is consistent with expectations. In order for the value of U_{LLJ}/U_{6m} to decrease, the LLJ wind speed must decrease or the mean 6-m wind speed must increase. It has already been shown that turbulence U_t increases for increasing U_{LLJ}, so it may be deduced in this scenario that the magnitude of U_{6m} is growing such that it is the dominant factor in determining the decreasing value of U_{LLJ}/U_{6m}. When the 6-m mean wind speed increases, this increases turbulence within the surface layer as more mixing is generated and subsequently transports momentum, sensible heat, and latent heat throughout the boundary layer. This result can also be seen in the U_{16m}/U_{6m} wind speed ratio, albeit on a smaller scale.

E. PRE-LLJ PROCESSES AND IDENTIFYING POSSIBLE LLJ INDICATORS

Thus, far, this thesis has given an in-depth description on the effects of the LLJ on various boundary layer quantities. A thorough investigation into LLJ-generated turbulence has also provided insight into the enhanced surface layer fluxes of momentum, sensible heat, and latent heat that also accompany LLJ presence. The analysis in this section will look into the state of the environment on the day prior to LLJ formation in an attempt to characterize possible indicators of LLJ formation and LLJ strength. The results could be helpful to forecasting strong LLJ formation on a given night.

1. Dynamic Stability

In a manner similar to the investigation of LLJ impact on bulk Richardson number at night, this analysis has also examined daytime Ri_B on the day prior to a LLJ event. Figure 43 shows the daytime Ri_B plotted against previously depicted wind speeds and wind speed ratios.

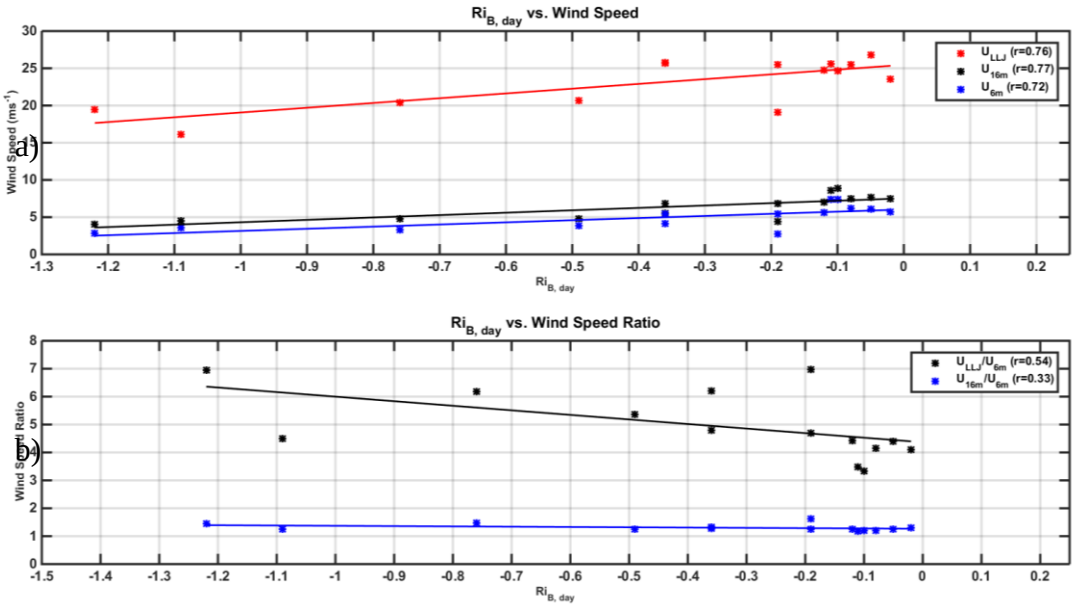

This figure includes a) LLJ wind speed (red), 16-m mean wind speed (black), and 6-m mean wind speed (blue) as a function of daytime Ri_B, and b) the ratio of the LLJ wind speed and 16-m mean wind speed at the time of the jet (U_{LLJ}/U_{16m}) (black) and ratio of the 16-m wind speed and 6-m mean wind speed at the time of the jet (U_{16m}/U_{6m}) (blue) against daytime Ri_B, respectively.

Figure 43. Relationship between Preceding Daytime Ri_B and Wind Speed/Wind Speed Ratio

Correlation between the previous day bulk Richardson number and U_{LLJ}, U_{16m} and U_{6m} is strong, with coefficients of 0.76, 0.77, and 0.72, respectively. For each increasing wind speed value (LLJ, 16 m, and 6 m), the magnitude of previous day Ri_B decreases, meaning it becomes closer to neutral. In other words, as the previous day becomes less unstable, the LLJ event on the following night appeared to be stronger. This less negative daytime Ri_B is, by definition, primarily dominated by mechanical wind shear and less dominated by positive buoyancy (i.e., convective instability), as it is falls in the shear-dominated range of 0 to -1. There were two LLJ days with the observed Ri_B<-1, but these events were two of the weakest among all LLJ days. The presence of shear-dominated daytime stability is reinforced by Figure 41b, where the correlation yielded a coefficient of 0.54 for daytime Ri_B plotted against the following night's wind speed ratio between the LLJ nose and 6-m mean wind speed. The thermal stability aspect (i.e., numerator) of daytime bulk Richardson number will be discussed momentarily. However, it is

important to underscore the importance and validity of previous day Ri_B in the strength of absolute LLJ wind speed. In Klein (2015), it is suggested that LLJ wind speed must be normalized by an initial, mixed layer wind speed in order to accurately compare atmospheric stability to LLJ strength, and that absolute wind speed by itself may yield inaccurate correlation. This normalization is represented by U_{LLJ}/U_s in the Klein (2015) study and U_{LLJ}/U_g in the current study, which was determined to be unusable due to the sensor's inability to sample wind speeds truly representative of the geostrophic synoptic flow. Klein states that "the fact that stronger LLJs correspond with more neutral conditions merely reflects that atmospheric stability, in general, decreases as wind speed increases" (Klein 2015). While this is agreeable during the stable, nocturnal regime where LLJ presence imparts a certain amount of wind shear upon the boundary layer stability (as is shown in Figure 33a-b), causing an otherwise stable regime to become closer to neutral, this explanation may not be as straightforward during the previous afternoon CBL regime when the LLJ has not developed yet.

2. Thermal Stability

In order to confirm that the more neutral previous afternoon Ri_B values were in fact dominated by wind shear as opposed to positive buoyancy, this analysis also examined the thermal stability during the day prior to a LLJ event. Figure 44 contains correlation plots of the 16 m-surface temperature difference on the day prior to a LLJ event plotted against the LLJ, 16-m, and 6-m wind speeds, as well as the shear ratios U_{LLJ}/U_{6m} and U_{16m}/U_{6m}. Additionally, Figure 44 depicts the difference between the maximum absolute value of previous day 16 m-surface temperature difference and the maximum nocturnal 16 m-surface temperature difference on the night of the LLJ.

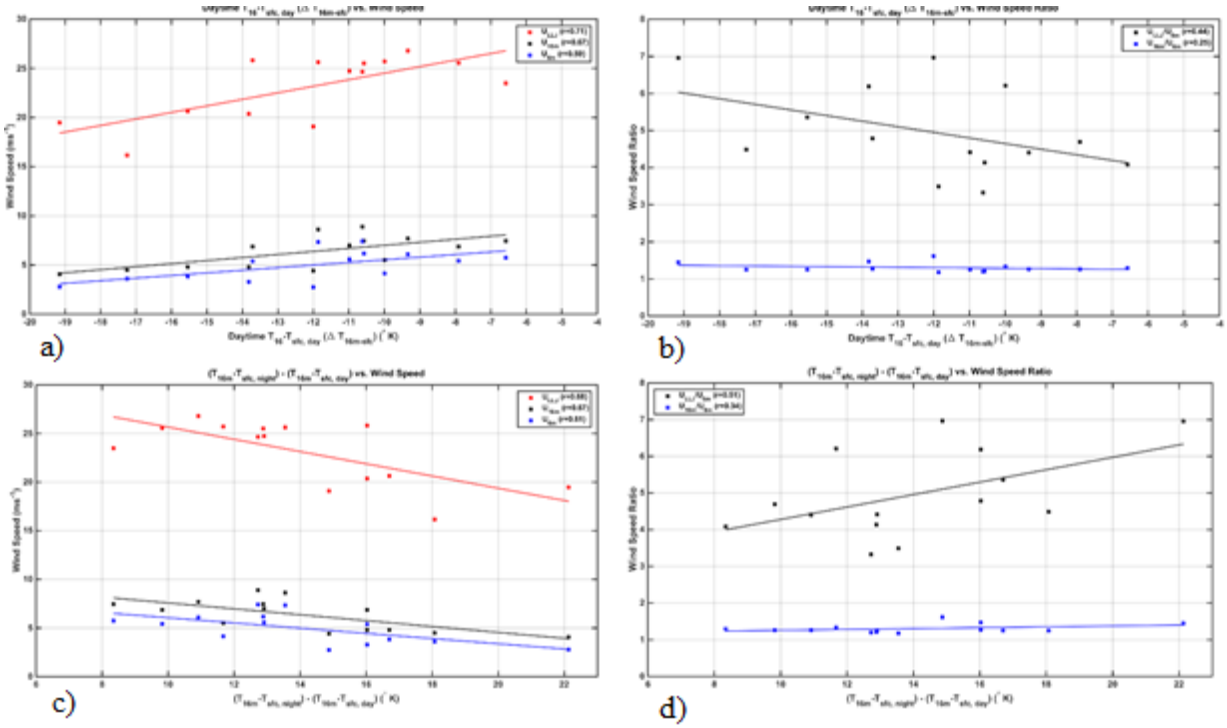

Shown are correlations between a) daytime 16 m-surface ΔT and LLJ wind speed (red), 16-m mean wind speed (black), and 6-m mean wind speed (blue), b) daytime 16 m-surface ΔT and shear parameters U_{LLJ}/U_{6m} (black) and U_{16m}/U_{6m} (blue), c) difference between nocturnal 16 m-surface ΔT and previous day 16 m-surface ΔT and LLJ wind speed (red), 16-m mean wind speed (black), and 6-m mean wind speed (blue), and d) difference between nocturnal 16 m-surface ΔT and previous day 16 m-surface ΔT and shear parameters U_{LLJ}/U_{6m} (black) and U_{16m}/U_{6m} (blue).

Figure 44. Daytime 16 m-Surface ΔT and Day to Night 16 m-Surface ΔT Difference Relationship with Wind Speeds/Wind Speed Ratios

The plots in Figure 44 support the findings discussed pertaining to daytime dynamic stability. With correlation coefficients of 0.71, 0.67, and 0.59 for U_{LLJ}, U_{16m} and U_{6m}, respectively, there is a clear relationship between the daytime thermal stability and the LLJ speed and associated surface layer wind speeds. Figure 43 suggests that near-neutral daytime Richardson numbers dominated by shear are conducive to a stronger LLJ the following night. The decreasing absolute value of 16 m-surface ΔT correlates well to a stronger absolute LLJ wind speed, as well as stronger 16-m mean wind speed and 6-m wind speeds at the time of the jet. The smaller magnitude of negative temperature difference between 16 m and the surface would also result in a smaller numerator in the Richardson number calculation and allow a larger difference in the denominator's wind

speeds, thereby bringing the Ri_B closer to neutral. While the height difference between the measurements of thermal stability (16m-surface) is admittedly different from the height difference used to make the Ri_B calculation (9.6m-1.3 m), the same physics apply to both, as they are both valid for the surface layer. Additionally, there is a high correlation between the difference in nocturnal ΔT and previous day ΔT with LLJ wind speeds, 16-m mean wind speeds, and 6-m mean wind speeds (Figure 42c) with coefficients of 0.68, 0.67, and 0.61, respectively. As the LLJ night to previous day ΔT difference decreases, LLJ wind speed, 16-m wind speed, and 6-m wind speed increase. This essentially means that days that are characterized by the smallest change between the daytime 16m-surface ΔT and 16m-surface ΔT on the night of the LLJ tend to promote not only LLJ presence, but stronger LLJ wind speeds and accompanying surface layer wind speeds. These high correlations between LLJ wind and daytime Richardson number and thermal stability suggest some forcing mechanisms that contribute to both weak daytime buoyancy forcing and nocturnal LLJ development. This is, however, inconsistent with previous LLJ studies relating strong daytime buoyancy forcing to LLJ development. Nearly every previous LLJ study suggests that the LLJ forms under "clear, cloud free conditions conducive to radiative cooling at night" (Singh 2002, Shapiro and Federovich 2009, Kutsher 2012, Klein 2015). The marginal thermal stability during both the daytime preceding a LLJ event and during the LLJ event itself raises questions about the validity of a clear and cloud free initial condition. From a radiation standpoint, clear, cloud free conditions during the summer months over the Great Plains generally results in maximum surface heating during the day (very thermally unstable) and maximum radiative cooling at night (strong thermal stability). Figures 45 and 46 are temporal variations in the 425–601 m mean wind speeds, cloud base height measurements from the laser ceilometer, and thermal stability.

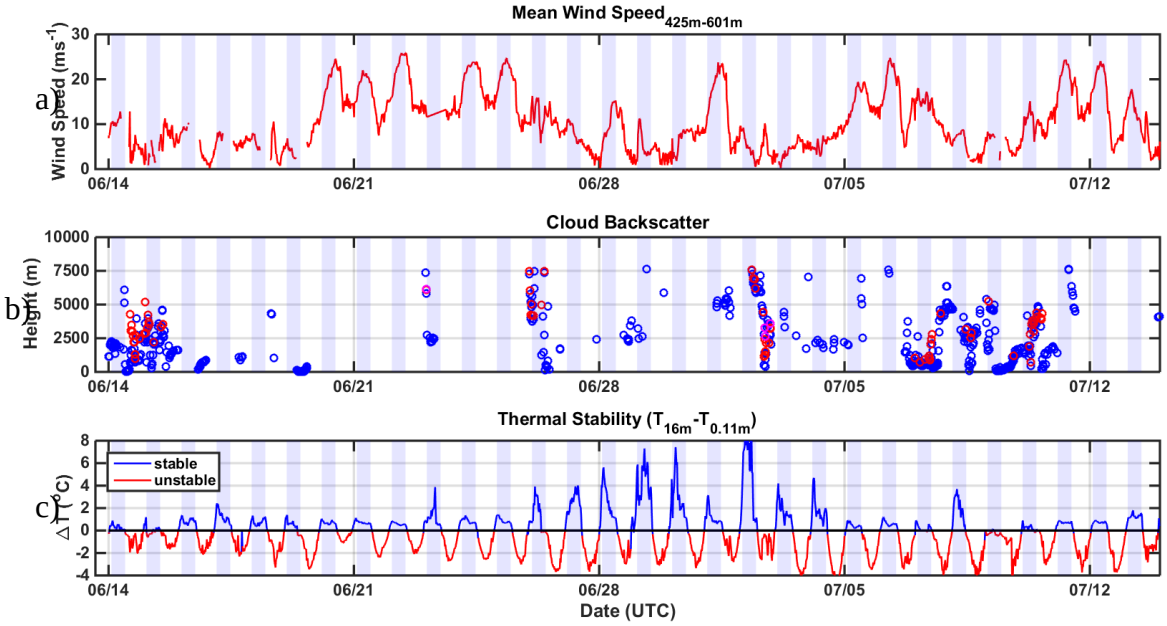

This figure depicts the full period a) the mean wind speed between 425 m and 601 m, b) cloud base height for low clouds (blue), mid-range clouds (magenta), and high clouds (red), and c) 16–0.11 m thermal stability (blue represents stable while red represents unstable conditions).

Figure 45. Full Period Temporal Variation of 425–601 m Mean Wind Speed, Cloud Base Height, and 16–0.11 m Thermal Stability

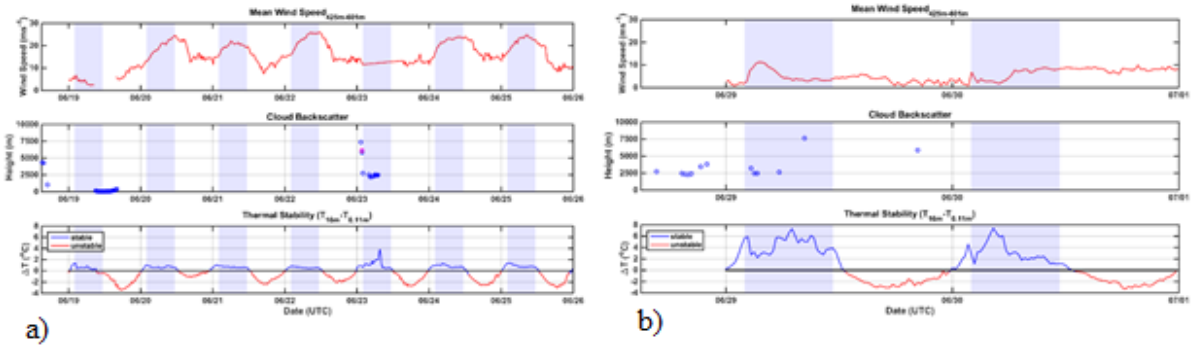

This figure depicts the same temporal variation in 425–601 m mean wind speed, cloud backscatter, and thermal stability as in Figure 45, except for a) LLJ days 20–22 June and 24–25 June and b) non-LLJ days 29–30 June.

Figure 46. Partial Period Temporal Variation of 425–601m Mean Wind Speed, Cloud Base Height, and 16–0.11 m Thermal Stability

Figure 45 seems to support the position of previous studies that, generally, LLJ formation is conducive to clear, cloud free conditions. Cloud cover found in Figure 45b is consistent with stronger LLJ events, for the most part. It also correlates well with the smaller magnitudes of daytime and nocturnal thermal stability (Figures 45c and 46a), which is contrary to expectations. There was one instance found for 30 June where the daytime period was characterized by relatively cloud free conditions with a subsequent non-LLJ night to follow, as well as a large magnitude of thermal stability during the nocturnal period. This would appear to be the only exception to the validity of pre-LLJ clear and cloud free conditions. An explanation for these scenarios, where cloud-free days relate to subsequent LLJ events as well as a non-LLJ event, would require additional follow on analysis and a larger sample size of LLJ and non-LLJ events.

Figure 44 shows that the correlation is not very strong between the shear parameters U_{LLJ}/U_{6m} and U_{16m}/U_{6m} and both the previous day 16 m-surface ΔT and the night to day 16 m-surface ΔT difference. The correlation between the previous day 2.5m-surface ΔT and night to daytime 2.5m-surface ΔT difference shows similar findings to that of the 16 m-surface thermal stability and can be seen in Figure 44. Correlation between daytime 2.5 m-surface ΔT and wind speeds at the LLJ nose, at 16 m, and 6 m remain equally high with coefficients of 0.72, 0.69, and 0.62, respectively. Additionally, there is strong evidence that lower night to day 2.5m-surface ΔT difference also promote stronger LLJ wind speeds, with correlation coefficients of 0.69, 0.68, and 0.62 for U_{LLJ}, U_{16m}, and U_{6m}, respectively. The slackening of thermal instability (near-neutral) in both the previous day 16 m-surface and 2.5 m-surface cases suggests that the minimal positive buoyancy in the Richardson number calculation allows the mechanical wind shear to play a significant role in determining the magnitude of Richardson number in these cases.

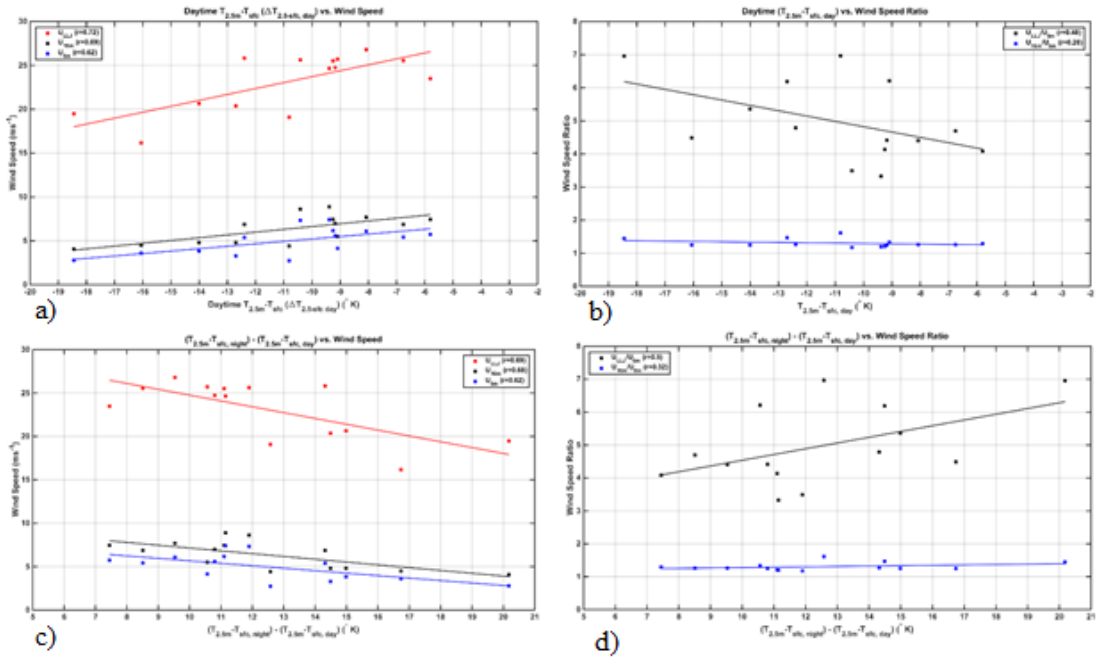

Shown are correlations between a) daytime 2.5m-surface ΔT and LLJ wind speed (red), 16m mean wind speed (black), and 6m mean wind speed (blue), b) daytime 2.5m-surface ΔT and shear parameters U_{LLJ}/U_{6m} (black) and U_{16m}/U_{6m} (blue), c) difference between nocturnal 2.5m-surface ΔT and previous day 2.5m-surface ΔT and LLJ wind speed (red), 16m mean wind speed (black), and 6m mean wind speed (blue), and d) difference between nocturnal 2.5m-surface ΔT and previous day 2.5m-surface ΔT and shear parameters U_{LLJ}/U_{6m} (black) and U_{16m}/U_{6m} (blue).

Figure 47. Daytime 2.5m-Surface ΔT and Day to Night 2.5m-Surface ΔT Differential Relationship with Wind Speeds/Wind Speed Ratios

3. Turbulence

In addition to previous day thermal stability and dynamic stability, this study has also considered previous day turbulence U_t and turbulence intensity U_t/U_{6m} as it relates to LLJ wind speed, surface layer wind speeds, and shear parameters. Figure 48 is a depiction of the correlation between these turbulence quantities and wind speeds U_{LLJ}, U_{16m}, and U_{6m}, and shear parameters U_{LLJ}/U_{6m} and U_{16m}/U_{6m}.

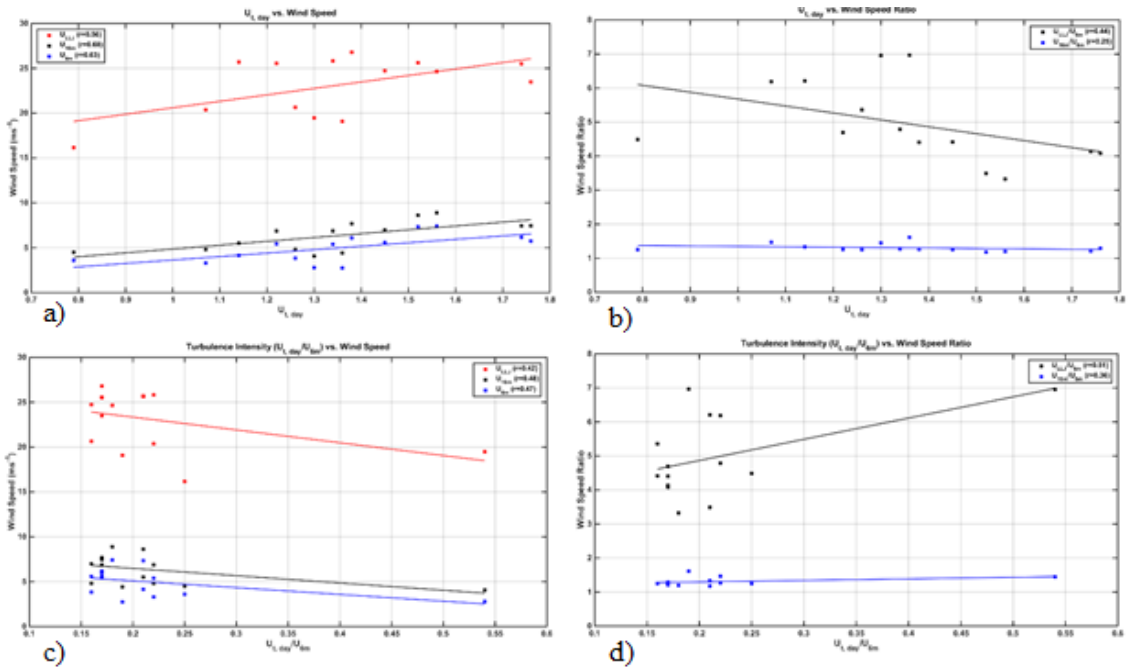

Shown are correlations between a) daytime turbulence U_t and LLJ wind speed (red), 16-m mean wind speed (black), and 6-m mean wind speed (blue), b) daytime turbulence U_t and shear parameters U_{LLJ}/U_{6m} (black) and U_{16m}/U_{6m} (blue), c) daytime turbulence intensity U_t/U_{6m} and LLJ wind speed (red), 16-m mean wind speed (black), and 6-m mean wind speed (blue), and d) daytime turbulence intensity U_t/U_{6m} and shear parameters U_{LLJ}/U_{6m} (black) and U_{16m}/U_{6m} (blue).

Figure 48. Daytime Turbulence U_t and Turbulence Intensity U_t/U_{6m} Relationship with Wind Speeds/Wind Speed Ratios

Daytime turbulence U_t showed strong correlation with the LLJ wind speed, 16-m mean wind speed, and 6-m mean wind speed with correlation coefficients of 0.56, 0.68, and 0.64, respectively, as is shown in Figure 48a. For increasing turbulence, whose quantity when squared is equivalent to TKE, LLJ wind speed, 16-m mean wind speed, and 6-m mean wind speed all increase. This correlation, once again, supports a daytime CBL with significant contributions by wind shear instead of being dominated by positive buoyancy when favoring following night LLJ development. Before plotting the correlation plots of turbulence U_t against wind speeds at the LLJ nose, 16 m height, and 6 m height, the correlation data between boundary layer stability and these same wind speed quantities suggested significant contribution from mechanical wind shear in turbulence generation prior to LLJ events. Figure 48 justifies this expectation and is consistent with the shear-dominated stability correlation depicted previously in Figure 43.

The correlation for turbulence intensity plotted against the wind speeds and wind speed ratios in Figure 48c and 48d was relatively low, as the majority of data points exhibited a wide scatter and lump grouping on extreme low end of the U_t/U_{6m} scale, with the exception of one outlier on 28 June. Since TKE and the wind speed at 6 m height are both related to the LLJ induced wind shear, the turbulence intensity, when defined as the ratio of the two, apparently does not provide significant information.

As the weakest LLJ in the "strong" category, the case on 28 June deserves further evaluation. The night of 28 June fit the definition of the LLJ as defined in Andreas (2000) and possessed both anticyclonically rotating winds and wind direction from a southerly sector. However, the previous afternoon of 27 June was characterized by a northerly wind and possible frontal boundary passage, rendering the correlation of the previous day parameters an exceptional case. Table 2 shows that June 28 contained some extreme observational statistics for non-anomalous LLJ events, including the lowest observed 16-m and 6-m mean wind speed at the time of jet max (4.05 ms^{-1} and 2.80 ms^{-1}, respectively), one of the few cases with the latest time for LLJ peak (11:12 UTC), a tie for the lowest height of LLJ maximum (283 m AGL), the most unstable daytime Ri_B value (-1.22), the highest daytime turbulence intensity U_t/U_{6m} (0.54), the lowest nighttime turbulence U_t (0.46), the most thermally unstable daytime 16m-surface and 2.5m-surface ΔT (-18.45°C and -19.16°C, respectively), and the largest night to day differential of ΔT for both 16m-surface and 2.5m-surface (20.17°C and 22.13°C). The very unstable daytime Ri_B and large daytime ΔT suggest a very convectively unstable regime during the day period, and thus may regarded with skepticism when correlating with the subsequent LLJ event. HRDL data for 27–28 June is given in Figure 49.

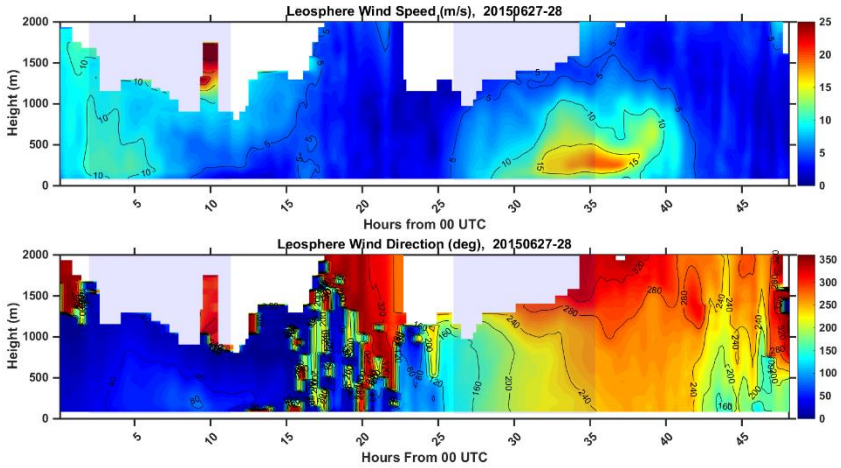

Shown are wind speed and direction for the LLJ event on 27 and 28 June 2015.

Figure 49. Leosphere HRDL Data for the 27–28 June Case

While some of these previously discussed boundary layer parameters do show strong correlation with the development and strength of subsequent LLJ events, it is important to note that the boundary layer undergoes transition on a small temporal scale. By their nature, turbulence and stability evolve on the scale of an hour or less at times and must be regarded with a certain degree of uncertainty. However, the boundary layer should be viewed as a general reflection of larger scale synoptic processes which impart different properties and effects on the lowest kilometer of the atmosphere, including the surface layer. The correlation between some of these previous day surface layer processes and the LLJ may be regarded, in part, as a correlation with a variety of these synoptically imparted properties and quantities.

V. CONCLUSIONS

The nocturnal LLJ is a boundary layer phenomenon that occurs under dry, cloud free conditions characterized by strong radiative cooling at night. They occur in many areas of the world, including several regions where U.S. DOD assets and manpower operate. The nocturnal LLJ is most frequently observed and studied, however, across the Great Plains of the United States during the summer months when predominant synoptic flow originates from southerly sectors. The importance of understanding the LLJ must not be minimized, as it carries wide-ranging implications on a variety of operational aspects. LLJs provide dynamical and thermodynamic forcing for elevated thunderstorms and long-duration rain events when intersecting frontal boundaries at near-right angles. They are efficient conveyors of atmospheric particulates, aerosols, migrating insects, mold spores, and fungi. LLJs pose aviation hazards to aircraft during take-off and landing. Finally, accurate forecasting and numerical modeling of LLJ events is of great interest to both the wind-energy industry and fire weather agencies due to their potential for both profit and catastrophe, respectively. While much research has been undertaken in improving modelling both from a theoretical standpoint and an observational standpoint, there is much to learn about these phenomena.

Inertial oscillation, proposed by Blackadar in 1957, was one of the first theories offered in identify the controlling mechanisms for LLJ development. Upon the cessation of friction at the collapse of the daytime CBL, air parcels are released from frictional constraint and able to accelerate freely with anticyclonic rotation forced by Coriolis. Numerous additional improvements have been made since the Blackadar (1957) study, including the Holton (1967) application of a gently sloping terrain, which is characteristic in the Great Plains region, as well as the Shapiro et al. (2009, 2010) combination of baroclinicity and Holton's sloping terrain. Understanding of LLJ properties and formation from a boundary layer perspective has been greatly advanced by Banta (2002, 2003) and Klein (2015).

The team from the Naval Postgraduate School participated in the two-month long PECAN campaign, which was a multi-university, multi-agency research project that was

geared towards collecting data on four summertime phenomena over the Great Plains: nocturnal mesoscale convective systems (MCS), nocturnal bore waves, nocturnal convective initiation (CI), and nocturnal LLJs. The NPS team was situated at FP-2 in Greensburg, KS and made extensive, continuous boundary layer measurements from this fixed site throughout the campaign. Included in the NPS continuous sensor suite was a Doppler sodar, a ceilometer, a 16-m tower with multiple levels of turbulence measurement and measurements of temperature, relative humidity, water vapor density, and mean wind speed and direction, a 6-m tripod with redundant measurements of turbulence and the mean quantities just mentioned, a 3-m scalar tripod with multiple levels of near-surface temperature and humidity measurements, as well as measurements of soil temperature, moisture content and incoming and outgoing solar/infrared radiation. In addition to these fixed, continuous sensors, the NPS team also employed a mobile rawinsonde sounding system and a mobile tethered balloon system equipped with Anasphere tethersondes and iMet radiosondes capable of profiling temperature, moisture, and wind speed and direction during events of interest. Finally, a FP-2 collocated team from UMBC operated a Leosphere 200S high-resolution Doppler lidar system that made continuous scans at a variety of azimuth angles, retrieving horizontal wind speed and direction, as well as vertical velocities. For the purposes of this analysis, the NPS team combined measurements and observations across all sensors to better characterize surface layer processes under LLJ influence.

The current study first investigated a variety of measurements and processes that occur within the surface layer as a response to LLJ presence over FP-2 during PECAN. General LLJ properties as observed from the perspective of a coarse interpolation of rawinsonde soundings include many LLJ tops at approximately 1000 m AGL with LLJ maxima occurring between 300 m and 700 m AGL, and a very shallow layer of weak surface wind speeds at the Earth's surface. Because of the coarse rawinsonde interpolation, LLJ events were better identified using continuous profiling measurements from the Leosphere HRDL. Vertical positioning of LLJ cores was generally agreeable with the rawinsonde plots, but LLJ top heights were found to be slightly more variable. A total of 33 LLJ events as defined by Andreas (2000), were identified over the full project

period using the HRDL data, but because of setup delays in additional sensors used in the analysis, this number was reduced to 20 (Table 2). In the analysis of LLJ formation and effects on the surface layer, this number was further reduced to 14 LLJ events, as some of the weak LLJs clearly show different characteristics than the strong LLJs with wind from the southerly sectors. These weak LLJs that were excluded from the analyses have various characteristics including predominant wind direction from the north or east, and/or cyclonically rotating winds with time and height (Figure 29).

The altitude variation of wind speed and direction was examined in detail, and it was observed that surface layer wind speeds, while experiencing a net decrease nearly every night, were slightly stronger during the nocturnal period during LLJ events (Figure 24). Additionally, the temporal variation of altitude varying wind speed also yielded boundary layer wind speeds and surface layer wind speeds at the beginning of the nocturnal period that were nearly out of phase during LLJ events. During the day preceding a LLJ event, these wind speeds at higher boundary layer levels and surface layer levels would vary in synchronization throughout the daytime period, but then would separate significantly around the time of sunset, only to converge again just after sunrise.

Closer inspection into the timing of LLJ development and subsequent decrease of surface layer winds around sunset revealed that it may be more appropriate to observe the transition of these quantities in terms of thermal stability. While the cessation of turbulent friction is directly correlated to the reduction of incoming shortwave irradiance to a minimum value, the transition of thermal stability from an unstable, negative value to positive, stable stratification occurs as much as an hour or more before sunset, and remains as much as an hour after sunrise. The divergence of higher boundary layer winds associated with the LLJ from surface layer winds around sunset and the subsequent convergence of these same altitude-varying wind speeds and directions at sunrise seems better correlated with the onset and collapse of stable thermal stratification (Figure 25).

Thermal stability over the experiment period was reviewed in great detail, and it was observed that nights under the influence of LLJ presence exhibited weakly stable stability during the nocturnal period than non-LLJ nights. Nights with LLJ events with maxima of 20 ms^{-1} or more were accompanied with 16–0.11 m temperature differences of

2°C or less, with the exception of 01 July, 2015 (Figures 26 and 27). Conversely, nights with the strongest inversions tended to lack LLJ wind maxima. While low correlation coefficients for LLJ wind speeds and associated surface layer wind speeds (Figure 30) have precluded the proposal of a nominal nocturnal 16–0.11 m surface layer temperature inversion of 2°C as a byproduct of strong LLJ formation, the temporal variation of surface layer nocturnal thermal stability does assist in separating LLJ events from non-LLJ events. Additionally, while these results roughly agree with the numerical simulations of Shapiro et al. (2009), whose results are best shown in Figure 8, these findings with regard to thermal stability are valid for inversion heights only in the surface layer where processes occur in much more intricate detail and on smaller time scales, as opposed to several hundreds of meters above ground, as was proposed for the LLJ maximum V_{max} delineated in the Shapiro et al. study.

In addition to thermal stability, dynamic stability from the perspective of bulk Richardson number, as defined in Equation (14) and following Klein (2015), was examined in relation to nocturnal LLJ evolution. It was shown in Figures 31–33 that LLJ events tend to favor smaller values of nocturnal Ri_B in the surface layer. Positive Ri_B values between 0 and 1 define stable stability in a shear-dominated (Ri_B denominator) regime, while positive values of Ri_B in excess of 1 define a weak- or non- turbulent boundary layer in a negative buoyancy-dominated (Ri_B numerator) regime. With a correlation of 0.7, strong absolute LLJ wind speed maxima tended to promote positive Ri_B values less than 1 with shear generated turbulence overcoming buoyancy consumption. The same conclusion could not be drawn for weaker absolute LLJ wind maxima, as the spread was slightly larger. The wind shear parameter U_{16m}/U_{6m} yielded a correlation coefficient of 0.53 with nocturnal Ri_B values, which tended to increase slightly for increasing shear parameter. This relationship highlights thermal stability effects on wind shear in the surface layer, where under stable conditions, thermal stability effects tend to increase wind shear, which is consistent with the Monin-Obukhov similarity theory. Stronger thermal stability tends to suppress vertical turbulent mixing, resulting in vertically enhanced wind shear.

The relationship between turbulence and surface fluxes of various quantities was also studied in relation to LLJ presence. The temporal variations in Figure 36 depicts the observed diurnal variation of surface fluxes of momentum, sensible heat, and latent heat. While all nocturnal values of momentum flux remain nearly constant at night, nights under LLJ influence show slightly larger magnitudes of fluxes between sunset and sunrise than non-LLJ nights. LLJ-influenced wind speeds generate enhanced mechanical turbulence below the jet nose, resulting in a subsequently enhanced value of momentum flux throughout the night. Additionally, the time series of sensible heat flux depicts a larger magnitude of downward sensible heat flux on stronger LLJ days, which also owes to the enhancement of surface layer winds beneath the LLJ nose. Wind shear generated by the LLJ increases turbulent mixing within the surface layer and thereby transporting sensible heat to the surface from aloft. Finally, latent heat flux magnitudes were also observed to be enhanced under LLJ presence. During LLJ events, the surface layer was characterized by increased latent heat flux, transporting moisture from the surface to the atmosphere via turbulent vertical mixing. These findings are shown clearly in Figure 37.

Understanding of the behavio of surface fluxes of momentum, sensible heat, and latent heat was reinforced by inspecting the effect of LLJ presence on turbulence. As previously described, these surface fluxes undergo a diurnal evolution with strong turbulent transport during the day and a much reduced magnitude at night. During LLJ events, TKE behaves in a similar fashion where large TKE values with significant buoyancy forcing in the CBL subsides to a near-constant value around sunset, only to begin increasing again upon LLJ development. This increase stems from enhanced mechanical shear-driven turbulence. Once incoming solar radiation is reintroduced at sunrise, TKE increases once again with the onset of the CBL. The commencement of LLJ formation coincides almost exactly with the time of TKE minimum, making a strong case for an inertial oscillation-dominated LLJ where surface frictional effects are at a minimum. TKE correlation with strong LLJ wind maxima is high, with increasing values of TKE for increasing LLJ wind maxima. This reiterates the fact that surface layer turbulence is strongly influenced in LLJ events and tends to be reasonably enhanced by LLJ-generated wind shear as well as the relaxed thermal stability. The enhanced

turbulence at the hands of the LLJ wind maxima also provides additional support to the observed enhanced surface fluxes, where higher than normal amounts of turbulence under strong LLJ presence supports increased vertical mixing, allowing quantities of momentum, sensible heat, and latent heat to be transported very efficiently.

Following a thorough examination of the nocturnal boundary layer response during LLJ events, thoughtful consideration was given to possible LLJ pre-cursors on the day prior to development that might indicate LLJ presence and strength ahead of time. Bulk Richardson number values for the day prior to each LLJ event were analyzed against wind speed properties from the events themselves. It was found that there was a strong correlation between daytime Ri_B values and wind speeds of the LLJ, 16m mean wind at the time of the jet, and 6m mean wind at the time of the jet (Figure 43). Small magnitudes of the daytime dynamic stability (Bulk Richardson number) are correlated with high LLJ wind speeds and surface layer wind speeds. As conditions approached near-neutral during an afternoon leading up to a LLJ event, the LLJ event on the following night tended to be stronger. These slightly negative daytime Ri_B cases have significant contribution by mechanical wind shear, as seen in the range of Richardson number of -1 to 0. It lends to the emphasis and validity of comparing LLJ wind speed to daytime Ri_B values by also exploring daytime thermal stability. With strong correlation between both 16 m-surface and 2.5 m-surface daytime ΔT and wind speeds at the LLJ nose, 16 m, and 6 m heights, respectively, it appears that there is also a clear relationship between daytime thermal stability and the LLJ. LLJ wind speed and associated surface layer wind speeds tended to increase for small magnitude daytime ΔT, or the daytime regime becoming less unstable. This, in turn, would also result in a smaller numerator in the Richardson number calculation and allow for a larger differential in the denominator's wind speeds, thereby bringing the Ri_B closer to neutral, which is consistent with observations. There is also strong correlation between the night to day temperature difference. This is represented by both the 16 m-surface and 2.5 m-surface ΔT_{night}- ΔT_{day}. LLJ events with days characterized by the smallest difference between the nocturnal thermal stability and daytime thermal stability also exhibited stronger wind speeds. These daytime thermal stability findings reinforce the discussion on smaller Richardson number

values serving as a precursor to LLJ development for the following night. However, they also fail to explain why, under clear and cloud-free conditions, the magnitude of thermal stability for both daytime and night isn't larger, as would be consistent with strong thermal heating during the day and strong radiative cooling at night (Figures 45 and 46).

Finally, in order to examine whether mechanical shear is a dominant forcing term during the day leading up to a LLJ event, the turbulence parameter U_t was investigated. Daytime turbulence showed strong correlation with the LLJ wind speed, 16-m mean wind speed, and 6-m mean wind speed, where when increased daytime turbulence was observed, values of LLJ wind speed, 16-m mean wind speed, and 6-m mean wind speed all increase (Figure 48a).

Several areas for improvement and enlightenment have been reserved for future studies and collaboration. Additional scrutiny into the occurrence of different LLJ-influenced processes on a very small temporal scale would undoubtedly provide insight into the mechanics behind formation and strengthening of the LLJ. Such scrutiny will require a more in depth analysis of individual cases, their timing and strength, and a comparison against a control sampling of non-LLJ nights. Additionally, there is a particular interest in the LLJ events (as defined by the 2000 Andreas study) that occurred on the anomalous days where predominant wind direction was either northerly or easterly, and where the vertically-varying wind vector rotated cyclonically instead of anticyclonically. These special LLJ events yielded boundary layer parameter values that were inconsistent with the "traditional" Great Plains LLJ, but fell under the Andreas (2000) definition of a LLJ, nonetheless. It would be interesting to delve deeper into these individual cases such that their associated boundary layer effects and possible pre-cursors might be exploited.

THIS PAGE INTENTIONALLY LEFT BLANK

LIST OF REFERENCES

Andreas, E. et al., 2000. Low-level atmospheric jets and inversions over the western Weddell Sea. *Boundary Layer Meteor.,* **97(3)**, 459–486. Doi: 10.1023/A:1002793831076.

Baas, P. et al., 2009. A climatology of nocturnal low-level jets at Cabauw. *J. Appl. Meteor. Climatol.,* **48,** 1627–1642, doi: 10.1175/2009JAMC1965.1.

Banta, R. M. et al., 2002. Nocturnal low-level jet characteristics over Kansas during CASES-99. *Boundary Layer Meteor.,* **105**, 221–252.

Banta, R. M. et al., 2003. Relationship between low-level jet properties and turbulence kinetic energy in the nocturnal stable boundary layer. *J. of the Atmos. Sci.,* **60**, 2549–2555.

Blackadar, A. K., 1957. Boundary layer wind maxima and their significance for the growth of nocturnal inversions. *Bull. Am. Meteor. Soc.,* **38**, 283–290.

Bleeker, W. and M. J. Andre, 1951. On the diurnal variation of precipitation, particularly over central U.S.A., and its relation to large-scale orographic circulation systems. *Q.J.R. Meteor. Soc.*, **77(332)**, 260–271, doi: 10.1002/qj.49707733211.

Chen, G. T., and Chia-Chung Y., 1988. Study of low-level jet and extremely heavy rainfall over northern Taiwan in the Mei-Yu Season. *Mon. Wea. Rev.*, **116**, 884–891, doi: 10.1175/1520-0493(1988)116<0884:SOLLJA>2.0.CO;2.

Delgado, R. et al., 2016. FP2 UMBC Doppler Line of Sight Wind Data, Version 1.1. UCAR/NCAR—Earth Observing Laboratory. Accessed 22 Oct 2016. http://doi.org/10.5065/D6Q81B4H.

Garreaud, R. D., and R. C. Munoz, 2005. The low-level jet off the west coast of subtropical South America: Structure and variability. *Mon. Wea. Rev.,* **133**, 2246–2261, doi: 10.1175/MWR2972.1.

Holton, J.R., 1967. The diurnal boundary layer wind oscillation above sloping terrain. *Tellus*, **19**, 199–205, doi:10.1111/j.2153-3490.1967.tb01473.x.

Hu, X-M. et al., 2013b. Impact of low-level jets on the nocturnal urban heat island intensity in Oklahoma City. *J. Applied Meteor. Climatol.,* **52(8)**, 1779–1802, doi: 10.1175/jamc-d-12-0256.1.

Klein, P. M. et al., 2015. Linkages between boundary-layer structure and the development of nocturnal low-level jets in central Oklahoma. *Boundary Layer Meteor.*, **158**, 383–408, doi: 10.1007/s10546-015-0097-6.

Kutsher, J. et al., 2012. On the formation of an elevated nocturnal inversion layer in the presence of a low-level jet: a case study. *Boundary Layer Meteor.*, **144**, 441–449, doi: 10.1007/s10546-012-9720-y.

National Severe Storms Laboratory, 2015. PECAN: Plains Elevated Convection at Night Factsheet. National Severe Storms Laboratory. Accessed 22 Oct 2015. http://www.nssl.noaa.gov/news/factsheets/PECAN_2015_NSSL_FINAL.pdf

Shapiro, A. and E. Federovich, 2009. Nocturnal low-level jet over a shallow slope. *Acta Geophysica*, **57**, 4, 950–980, doi: 10.2478/s11600-009-0026-5.

Shapiro, A., and E. Federovich, 2010. Analytical description of a nocturnal low-level jet. *Q. J. R. Meteor. Soc.*, **136(650)**, 1255–1262, doi: 10.1002/qj.628.

Shapiro, A. et al., 2016. A unified theory for the Great Plains nocturnal low-level jet. *J. of the Atmos. Sci.*, **73**, 3037–3057, doi: 10.1175/JAS-D-15-0307.1.

Singh, M.P. et al., 1993. An analytical study of diurnal wind-structure variations in the boundary layer and the low-level nocturnal jet. *Boundary Layer Meteor.*, **63**, 397–423.

Song, J. et al., 2005. Climatology of the low-level jet at the southern Great Plains atmospheric boundary layer experiments site. *J. Appl. Meteor.*, **44(10)**, 1593–1606, doi: 10.1175/JAM2294.1.

Stull, R.B., 1988: *An Introduction to Boundary Layer Meteorology*. Kluwer Academic Publishers, 670 pp.

Vickers, D., and L. Mahrt, 2003. The cospectral gap and turbulent flux calculations. *J. Amos. Oceanic Technol.*, **20**, 660–672.

Wei, W. et al., 2013. Characteristics and mechanisms of low-level jets in the Yangtze River delta of China. *Boundary Layer Meteor.*, **149(3)**, 403–424, doi: 10.1007/2006jame1283.1.

Wexler, H., 1961. A boundary layer interpretation of the low-level jet. *Tellus*, **13(3)**, 368–378.

Zhong, S. et al., 1996. A case study of the Great Plains low-level jet using wind profiler network data and a high-resolution mesoscale model. *Mon. Wea. Rev.*, **124(5)**, 785–806, doi: 10.1175/1520-0493(1996)124(aa)0785:ACSOTG(aa)2.0.CO;2.

INITIAL DISTRIBUTION LIST

1. Defense Technical Information Center
   Ft. Belvoir, Virginia

2. Dudley Knox Library
   Naval Postgraduate School
   Monterey, California